
**UNIVERSITÀ DEGLI STUDI DELL'AQUILA**
**DIPARTIMENTO DI SCIENZE FISICHE E CHIMICHE**


Dottorato di Ricerca in Scienze Fisiche e Chimiche
Curriculum comune
XXXVI ciclo

Titolo della tesi

# Raman LIDAR-Based Aerosol Profiling for Atmospheric Studies in Ultra High Energy Cosmic Ray Observatories

SSD FIS/01


Dottorando
Emanuele Avocone

Coordinatore del corso
Prof. Massimiliano Aschi

Tutor
Prof. Vincenzo Rizi



a.a. 2022/2023

*In appreciation of my family's unwavering support.*

# Contents

# Raman LIDAR-Based Aerosol Profiling for Atmospheric Studies in Ultra High Energy Cosmic Ray Observatories

**Emanuele Avocone**

## Abstract

The presence of aerosols in the atmosphere impacts various aspects, underscoring the importance of continuous monitoring of these minute particles. Within ultra-high-energy cosmic ray observatories, neglecting the attenuation of light due to atmospheric molecules and aerosols introduces a significant systematic error in determining the properties of the primary particle. At the Pierre Auger Observatory, a comprehensive atmospheric monitoring program has been developed to correct observations of extensive atmospheric showers conducted with the Fluorescence Detector (FD).

This work describes the Raman lidar of the Pierre Auger Observatory, operational since September 2013, which allows monitoring of aerosols above the central laser facility. The vertical profiles of aerosol optical depth have been obtained for the period 2013-2022, highlighting a seasonal variability and obtaining, for those nights with a low aerosol load, an average value of 0.04 at a reference altitude of 4.5 km above ground level. The vertical distribution of aerosols can be modeled using two or three parameters, with lidar data better described by the three-parameter model. Information obtained from Raman lidar measurements is also used within the collaboration as a cross-check with other methods used to determine aerosol attenuation.

Next, the development of a Raman lidar system, both hardware and software components, for monitoring atmospheric aerosols is described. Given the regions where cosmic ray observatories are located, solutions have been tested to simplify maintenance, eliminating the need for specialized personnel on-site. This objective is achieved by using a bundle of optical fibers within the receiver. The initial observations conducted in L'Aquila are reported, which have proven to be very encouraging.

# List of Figures

# List of Tables

# Introduction

*The Cosmic rays*
*over the pampa or not,*
*aerosols rule.*

---

V. Rizi

The interest in aerosols arises from multiple factors: they can have adverse effects on human health, they exert a significant impact on atmospheric chemistry, and they significantly influence the atmospheric radiative balance. Related to this last aspect is the importance of aerosols monitoring within ultra-high-energy cosmic ray observatories. At the Pierre Auger Observatory, the largest infrastructure in the world for the study of cosmic rays of which I am a member of the collaboration, a significant effort has been made to establish an aerosol monitoring program.

One of the primary tools for aerosol monitoring is the atmospheric lidar. In this work, I focused on the development of a multiwavelength Raman lidar system, engaging in the characterization and simulation of optical components through laboratory instruments and Zemax optical design software. A new solution involving the use of a fiber bundle in the receiver has been extensively tested. Substantial effort was also devoted to developing the control software for the instrument, which specifically handles dome opening and closing, powering all lidar subsystems, monitoring meteorological conditions, and data acquisition and storage. Additionally, I contributed to the creation of analysis software to extract aerosol optical properties from lidar signals. Looking ahead, plans include upgrading the lidar for integration into ACTRIS (Aerosols, Clouds, and Trace gases Research InfraStructure Network). This system will also serve as a testbed for future instruments to be installed at cosmic ray observatories.
As part of the Pierre Auger collaboration, I supervised the characterization of the new laser designated for the Central Laser Facility (CLF) and actively participated in measurement shifts for both the Fluorescence Detector and Surface Detector. Following this, I conducted data analysis of signals acquired by the observatory's Raman lidar, which has been acquiring data since September 2013.

Throughout my doctoral studies, I was also engaged in a measurement shift at the Large Size Telescope, LST1, situated at the Cherenkov Telescope Array Observatory (CTAO) on Roque de los Muchachos, La Palma. This observatory, dedicated to gamma-ray astronomy at very-high energies, employs an array of telescopes to capture Cherenkov radiation emitted by particle cascades resulting from the interaction of high-energy gamma rays with the atmosphere.
Additionally, during the mission, I contributed to the maintenance of the Raman

lidar ARCADE, which received substantial contribution from the Department of Physical and Chemical Sciences of the University of L'Aquila and was positioned near the observatory.

This work is structured into seven chapters:

1. In Chapter 1, we delve into atmospheric aerosols, solid or liquid particles suspended in the atmosphere. The chapter explores the rationale behind monitoring them, their classification, and introduces the size distribution function. Additionally, it covers the interactions of these particles with electromagnetic radiation.

2. Chapter 2 will delineate the characteristics of ultra-high-energy cosmic rays, including a concise historical overview of their discovery and an examination of the phenomenon of extensive air showers.

3. Chapter 3 will provide an overview of the Pierre Auger Observatory, a hybrid facility designed for detecting and researching ultra-high-energy cosmic rays. It will emphasize the observatory's extensive atmospheric monitoring program, with particular attention to aerosols, crucial for gathering data on cosmic rays.

4. In Chapter 4, the principles of Raman lidar for aerosol monitoring will be outlined. A thorough explanation will be given on how to invert the lidar equations to derive the optical properties of aerosols. The chapter will also cover crucial considerations, including digital filters and error propagation.

5. In Chapter 5, we delve into the hardware of the Raman lidar at the Pierre Auger Observatory, detailing the analysis of vertical aerosol optical depth derived from lidar signals collected between 2014 and 2022. The resulting data can be effectively described using a straightforward three-parameter model.

6. In Chapter 6 a comprehensive overview of the hardware and software of the AQ Raman lidar, located at the University of L'Aquila, is provided. The chapter delves into the lidar system's performance for atmospheric observations, detailing the results of tests conducted on optical components.

7. Finally, Chapter 7 will serve as a brief concluding chapter, summarizing all the findings presented in the thesis and exploring potential future projects that may stem from this research.

# Chapter 1

# Atmospheric aerosols

## 1.1 Introduction

The Earth's atmosphere is predominantly composed of gases, with the main components being molecular nitrogen, molecular oxygen, argon, and carbon dioxide. Nitrogen, oxygen, and argon alone account for more than 99% of the volume of the atmosphere. The concentration of these gases is predominantly uniform and independent of altitude within the first 100 kilometers (homosphere). In addition to these gases, water vapor and the so-called trace gases are present, which, despite their low concentration, play a fundamental role in the chemical evolution of the atmosphere. Table 1.1 shows the volume concentration values of the main molecules present in the atmosphere.

**Table 1.1:** Fractional concentrations of the major molecules of the Earth's atmosphere. From [1]. It should be noted that the carbon dioxide concentration has now exceeded 400 ppm

| Gas | Fractional concentration by volume |
|---|---|
| Nitrogen ($N_2$) | 78.08 % |
| Oxygen ($O_2$) | 20.95 % |
| Argon (Ar) | 0.93 % |
| Water vapor ($H_2O$) | 0-5 % |
| Carbon dioxide ($CO_2$) | 380 ppm |
| Neon (Ne) | 18 ppm |
| Helium (He) | 5 ppm |
| Methane ($CH_4$) | 1.75 ppm |
| Krypton (Kr) | 1 ppm |
| Hydrogen ($H_2$) | 0.5 ppm |
| Nitrous oxide ($N_2O$) | 0.3 ppm |
| Ozone ($O_3$) | 0-0.1 ppm |

In addition to gases, the atmosphere contains solid or liquid particles suspended in the air, called aerosols. To be precise, the term aerosol includes both the particles and the gas in which they are suspended (in our case, air) [2], but in atmospheric sciences the term aerosols is often used to refer to aerosol particles [3]. Due to the various sources, aerosols exhibit physical and chemical properties that vary over a

wide range and play a crucial role in many atmospheric processes. These particles range in size from about $10^{-3}$ µm to tens of micrometers and can have different shapes and different compositions [4]. An increase in global aerosols concentration might alter the radiation balance of the earth but, because of the large variability in space and time, their interaction with solar radiation is not completely known and, at present, atmospheric aerosols are considered one of the major uncertainties in climate forcing (Figure 1.1). But aerosols also affect cloud and precipitation physics and heterogeneous chemistry, and therefore, detailed measurements of their optical and microphysical properties are needed to understand their role in several areas. Furthermore, due to the large temporal variability, aerosols monitoring is crucial in those experiments where the atmospheric transparency has an important impact on the measurements, such as within ultra high energy cosmic ray observatories.

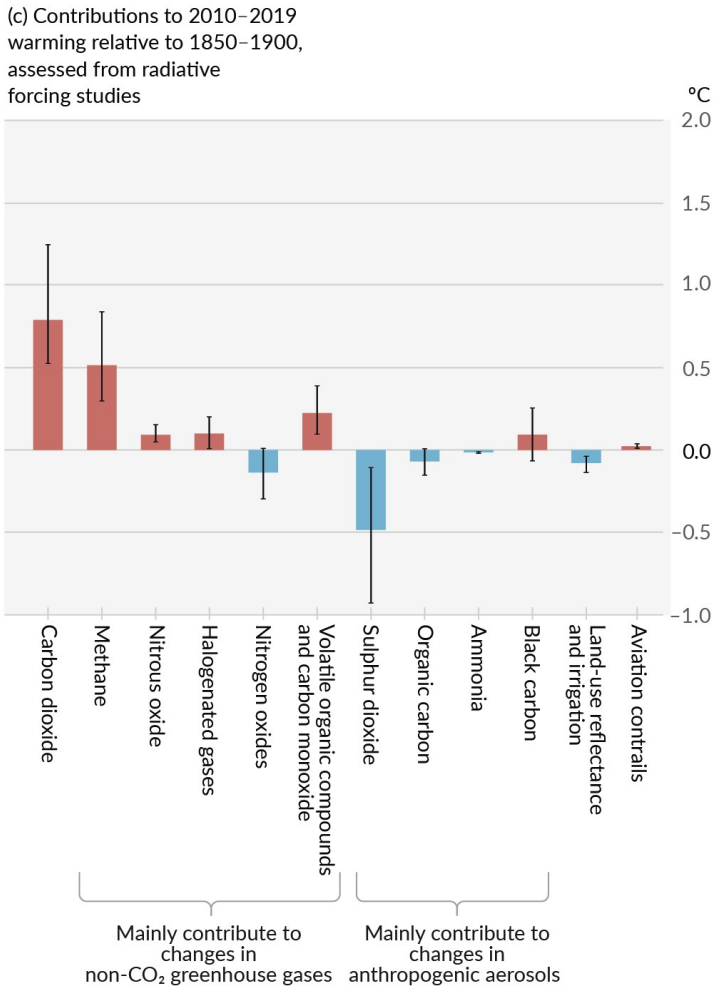


**Figure 1.1:** Temperature changes in 2010-2019 from individual components of human influence: emissions of greenhouse gases and aerosols; land-use changes; aviation contrails (Figure SPM.2 Panel(c) from [5]). The net effect of aerosols is a decrease in surface temperature, but there are large uncertainties in the data.

## 1.2 Aerosol classification

The chemical composition of aerosols is determined by their source, while their shape and size distribution are determined by the production process. The chemical composition determines the complex refractive index of the particle, with the real part determining its scattering properties and the imaginary part determining its absorption properties. All of these characteristics influence how particles interact with electromagnetic radiation.

Aerosols' sources can be primary and secondary. Primary sources are mostly natural and include oceans, arid lands, wildfires, and living organisms, but they can also be anthropogenic, such as road dust or soot. Some particles can also enter the atmosphere from space (cosmic aerosol). The secondary source is the conversion of atmospheric trace gases, of natural or anthropogenic origin, into liquid and solid particles (gas-to particle conversion) [4].

A first aerosol classification can be done on the basis of their size. Three categories can be identified:

- Aitken nuclei ($0.001\,\mu m < r < 0.1\,\mu m$);
- large particles ($0.1\,\mu m < r < 1.0\,\mu m$);
- giant particles ($r > 1.0\,\mu m$).

Particles with radius below $1.0\,\mu m$ are mainly produced through gas-to-particle conversion while aerosols greater than $1.0\,\mu m$ are produced by mechanical processes. Furthermore, Aitken nuclei constitute the nucleation mode while large particles are in the accumulation mode. Both Aitken nuclei and large particles constitute the fine mode, and the giant particles constitute the coarse mode.

Typically, atmospheric aerosols are categorized based on their origin and chemical composition. The main aerosol types present in the atmosphere are:

- sea salt;
- mineral dust;
- sulfate;
- nitrates;
- carbonaceous particles.

These latter include organic carbon and black carbon. Black carbon originates primarily from human activities and, among all aerosols, exhibits a non-negligible absorption of electromagnetic radiation.

The characteristics of aerosols, such as mass concentration, aerosol type, and composition, can vary greatly on regional and global scales. For this reason, aerosols can be classified based on the environment in which they are found into six categories: continental, urban, rural, maritime, desert, and arctic.
Continental aerosols are mainly of natural origin, are generally smaller in size, and have lower mass and number concentration than urban aerosols. In urban regions, aerosols are a mixture of particles directly emitted into the atmosphere from industries and transportation, and particles resulting from gas-to-particle conversion.

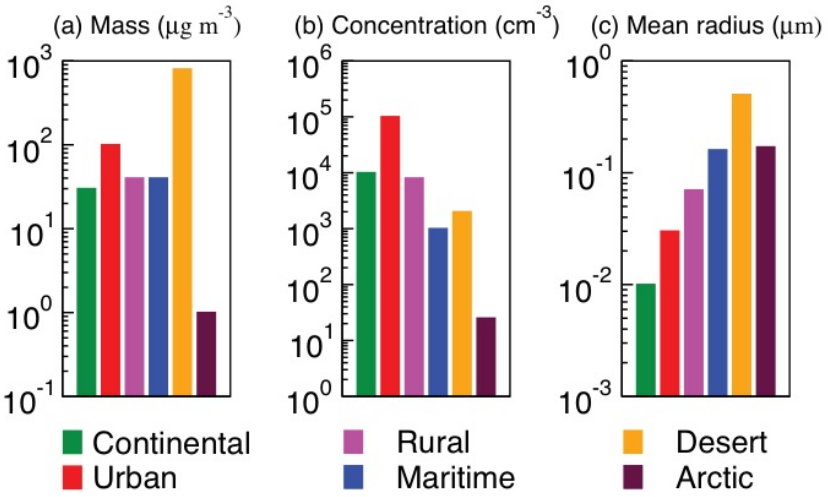


**Figure 1.2:** Mass, number concentration, and mean radius of aerosols in different environments (from [4]).

In contrast, in rural areas, aerosols are predominantly of natural origin and include sulfates, nitrates, and dust particles. Maritime aerosols are composed of sea salt and non-sea salt sulfates particles, while desert aerosols consist of dust particles and are larger and heavier. Finally, arctic aerosols result from the long-range transport of particles from other regions and include mineral dust, sea salt, sulfate, and biogenic material [4].
A summary of aerosol mass, concentration and radius in different environments can be found in Figure 1.2.

## 1.3 Particle size distribution

One of the most important parameters characterizing aerosols behavior is the particle size. The laws governing aerosols properties may also vary with this parameter, and therefore it is important to understand the distribution of particles. For a complete description of particle size distribution see [6] or one of the already cited books [3, 4].

Let $r$ be the radius of the particles and $n(r)$ be the particle size distribution. Then $n(r)dr$ is the particle number per unit volume with $r \in [r, r + dr]$. The total particle number per unit volume $N_0$ is given by

$$N_0 = \int_0^\infty n(r)dr, \tag{1.1}$$

and an average property can be estimated as an integral over the size distribution. Raw moments of order $i$ are defined as

$$r^{m_i} = \frac{1}{N_0} \int_0^\infty r^i n(r)dr. \tag{1.2}$$

The normal distribution is inadequate for describing aerosol particle size distribution, as most aerosols display a long tail at larger sizes. While it may suit monodisperse aerosols like certain pollen and spores, a broad normal distribution, where

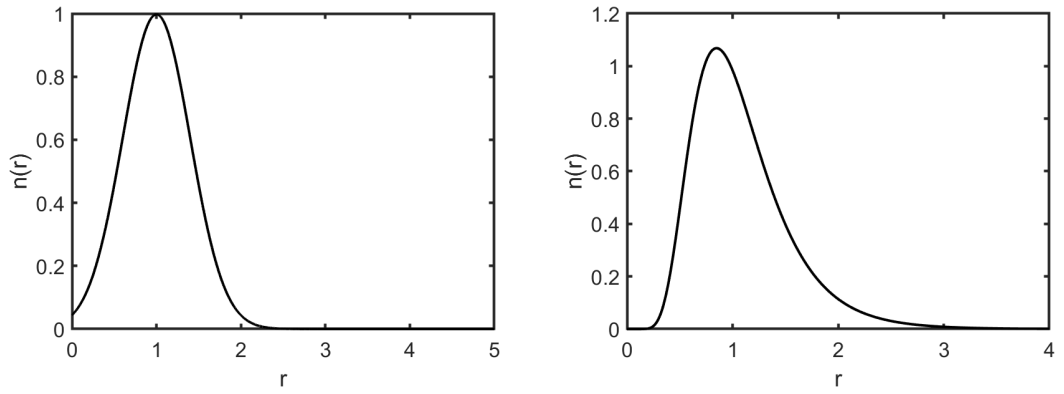


**(a)** Gaussian **(b)** Lognormal

**Figure 1.3:** Typical shapes of gaussian and lognormal distributions. The parameters used are $N_0 = 1$, $r_0 = 1$, $\sigma = 0.4$ and $s = 1.5$.

aerosol sizes vary widely, necessitates a portion of particles to have negative size. In situations where the distributed quantity can only have positive values and covers a broad range, the lognormal distribution is more appropriate.
The expressions for these two distributions are as follows:

$$n(r) = \frac{N_0}{\sqrt{2\pi}} \frac{1}{\sigma_0} e^{-\frac{(r-r_0)^2}{2\sigma_0^2}}, \tag{1.3}$$

$$n(r) = \frac{N_0}{\sqrt{2\pi}} \frac{1}{\ln s} \frac{1}{r} e^{-\frac{\ln^2 (r/r_0)}{2 \ln^2 s}}, \tag{1.4}$$

and can be observed in Figure 1.3. The parameters which characterize the two distributions are $N_0$, $r_0$ and $\sigma_0$ for the Gaussian one, and $N_0$, $\ln s$ ($s$ is the geometric standard deviation) and $r_0$ for the lognormal.
The presence of various aerosol types in the atmosphere is typically characterized by a multimodal lognormal distribution, which is the combination of two or more monomodal distributions. For instance, it may involve the combination of a lognormal distribution with its own parameters for the Aitken particle mode, another lognormal distribution for the accumulation mode, and yet another for the coarse mode.
Other distribution functions used to describe aerosols include the Junge power law [7]

$$n(r) = Cr^{-\nu-1}, \tag{1.5}$$

the modified gamma distribution [8]

$$n(r) = ar^{\alpha} \exp(-br^{\gamma}), \tag{1.6}$$

and the gamma distribution

$$n(r) = ar^{\alpha} \exp(-br). \tag{1.7}$$

The mean and integral properties which are ususally calculated from the particle size distribution are the effective radius

$$r_{\text{eff}} = \frac{\int n(r) r^3 dr}{\int n(r) r^2 dr}, \tag{1.8}$$

the total surface area concentration

$$a_{\mathrm{t}} = 4\pi \int n(r) r^2 dr \tag{1.9}$$

and the total volume concentration

$$v_{\mathrm{t}} = \frac{4\pi}{3} \int n(r) r^3 dr. \tag{1.10}$$

The effective radius is the ratio of the third and second moments, and it is important because the energy removed from a light beam is proportional to the particle's area. It can be seen as the average radius of the particles, with the section surface as weight.

## 1.4 Aerosol optical properties

In addition to determining the impact on radiative transfer in the atmosphere, the optical properties of aerosols make these particles detectable using remote sensing methods.

When a monochromatic beam with intensity $I$ passes through an atmospheric layer of thickness $ds$, the intensity is reduced due to absorption and scattering outside the beam by both molecules and aerosols. The variation in intensity is given by

$$dI = -k_{\mathrm{e}} I ds, \tag{1.11}$$

where $k_{\mathrm{e}}$ is the local extinction coefficient, and it is the sum of the absorption coefficient $k_{\mathrm{a}}$ and the scattering coefficient $k_{\mathrm{s}}$:

$$k_{\mathrm{e}} = k_{\mathrm{a}} + k_{\mathrm{s}}.$$

To describe the behavior of a molecule or a particle interacting with electromagnetic radiation, the extinction, absorption, and scattering cross-sections ($\sigma_{\mathrm{e}}$, $\sigma_{\mathrm{a}}$ and $\sigma_{\mathrm{s}}$) are typically used. The total cross section can be computed integrating the differential cross section over the whole solid angle:

$$\sigma = \int_{4\pi} \frac{d\sigma}{d\Omega} d\Omega.$$

By multiplying the cross-section by the numerical concentration of molecules or particles, the corresponding extinction, absorption and scattering coefficients are obtained.
For a finite-thickness atmospheric layer, it is possible to define the optical thickness (or optical depth) as

$$\tau_{\mathrm{e}} = \int_{s_1}^{s_2} \sigma_{\mathrm{e}}(s) ds.$$

If absorption is negligible, extinction is solely attributed to scattering processes.

Depending on particle size, several theories are available to describe the scattering process 1.4. If the scatterer dimensions are much smaller than the incident light wavelength (molecules), the scattering process can be described by Rayleigh theory, while, if the dimensions are comparable or greater than the light wavelength

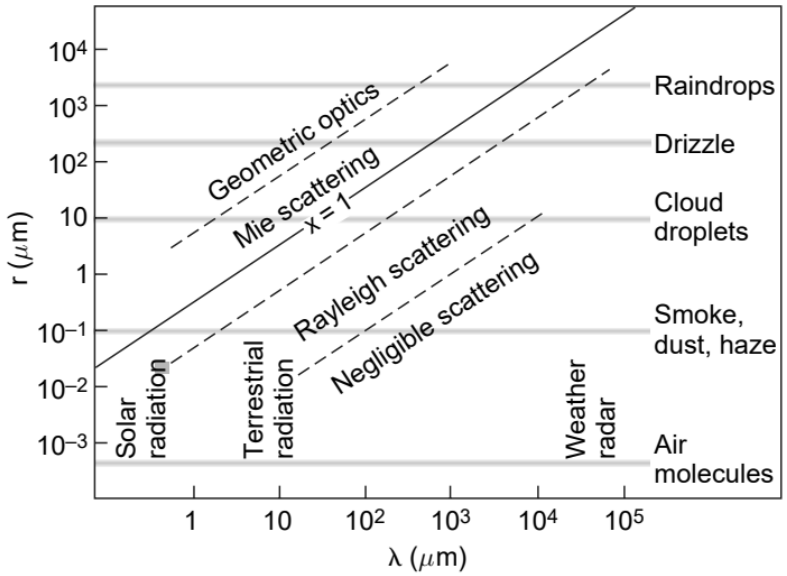


**Figure 1.4:** Size parameter and scattering processes. From [1]

(aerosols), the Mie theory is used. To discriminate the scatterer behaviour, the particle size parameter is used. It is defined as

$$x = \frac{2\pi r}{\lambda}, \tag{1.12}$$

where $r$ is the particle radius and $\lambda$ the incident wavelength.
A comprehensive explanation of scattering can be found in numerous texts, including [9, 10], while a recap can be found in lidar and aerosol books such as [11, 12].

### 1.4.1 Rayleigh Scattering

The theory of molecular scattering was first developed by J. W. Strutt, then Lord Rayleigh, in 1871 [13, 11]. Rayleigh scattering occurs when the particle dimensions are much smaller than the light wavelength. The electric field component of the propagating wave will induce a dipole moment in the molecules, which will radiate into the whole solid angle. The theory predicts for natural incident radiation, completely polarized scattered radiation at a scattering angle of 90°. However, observations have shown a small depolarization for this angle, attributable to the anisotropy of the molecules. For this reason, the so-called King factor $(6 + 3\delta_p)/(6 - 7\delta_p)$ was added, resulting in the following final formula for the total Rayleigh scattering cross section:

$$\sigma_{\mathrm{R}}(\lambda) = \frac{24\pi^3}{\lambda^4 N_s^2} \frac{\left(m_s^2 - 1\right)^2}{\left(m_s^2 + 2\right)^2} \left\{ \frac{6 + 3\delta_p}{6 - 7\delta_p} \right\}, \tag{1.13}$$

where $\lambda$ is the wavelength, $m_s$ is the refractive index for standard air, $N_s$ is the molecular density for standard air, and $\delta_p$ is the depolarization factor.

### 1.4.2 Mie Scattering

In 1908, Gustav Mie solved the scattering problem by dielectric spheres from Maxwell's equations [14].
The fields in the medium can be written as the superposition of the incident fields and the scattered fields

$$\vec{E_2} = \vec{E}_\mathrm{i} + \vec{E}_\mathrm{s}, \quad \vec{H_2} = \vec{H}_\mathrm{i} + \vec{H}_\mathrm{s},$$

with

$$\vec{E}_\mathrm{i} = \vec{E_0} exp\left(i\vec{k}\cdot\vec{x} - i\omega t\right), \quad \vec{H}_\mathrm{i} = \vec{H_0} exp\left(i\vec{k}\cdot\vec{x} - i\omega t\right).$$

The fields must satisfy Maxwell equations and boundary conditions (between the medium and the particle). Mie wrote the scattered electric field as

$$\begin{pmatrix} E_{\parallel\mathrm{s}} \\ E_{\perp\mathrm{s}} \end{pmatrix} = \frac{e^{ik(r-z)}}{-ikr} \begin{pmatrix} S_2 & S_3 \\ S_4 & S_1 \end{pmatrix} \begin{pmatrix} E_{\parallel\mathrm{i}} \\ E_{\perp\mathrm{i}} \end{pmatrix}, \tag{1.14}$$

where parallel and perpendicular are referred to the scattering plane, and determined the elements of the scattering matrix, which for the far field solution of the scattering by a sphere is diagonal.
Knowing the functions $S_1(\theta)$ and $S_2(\theta)$, with $\theta$ the scattering angle, it is possible to derive the extinction, scattering and absorption cross sections and the corresponding efficiencies which are related by

$$\sigma_\mathrm{abs} = \sigma_\mathrm{ext} + \sigma_\mathrm{sca}, \quad Q_\mathrm{abs} = Q_\mathrm{ext} + Q_\mathrm{sca}, \tag{1.15}$$

$$Q_X = \frac{\sigma_X}{\pi r^2}, \tag{1.16}$$

where $r$ is the particle radius and $X$ stands for absorption or extinction or scattering. The expressions found by Mie are

$$Q_\mathrm{sca} = \frac{2}{x^2} \sum_{n=1}^{\infty} (2n+1) \left(|a_n|^2 + |b_n|^2\right), \tag{1.17}$$

$$Q_\mathrm{ext} = \frac{2}{x^2} \sum_{n=1}^{\infty} (2n+1)\, Re\left(a_n + b_n\right), \tag{1.18}$$

where $x$ is the size parameter and $a_n$ and $b_n$ are the Mie coefficients.

Unfortunately, many aerosols exhibit complex morphologies, rendering the Mie theory inapplicable in these cases. Optical properties of such non-spherical particles must be measured in laboratory or computed through an advanced electromagnetic scattering theory.

### 1.4.3 Scattering properties

The phase function is defined as

$$p(\theta, m, \lambda) = \frac{(d\sigma_\mathrm{sca}/d\Omega)}{\sigma_\mathrm{sca}} \tag{1.19}$$

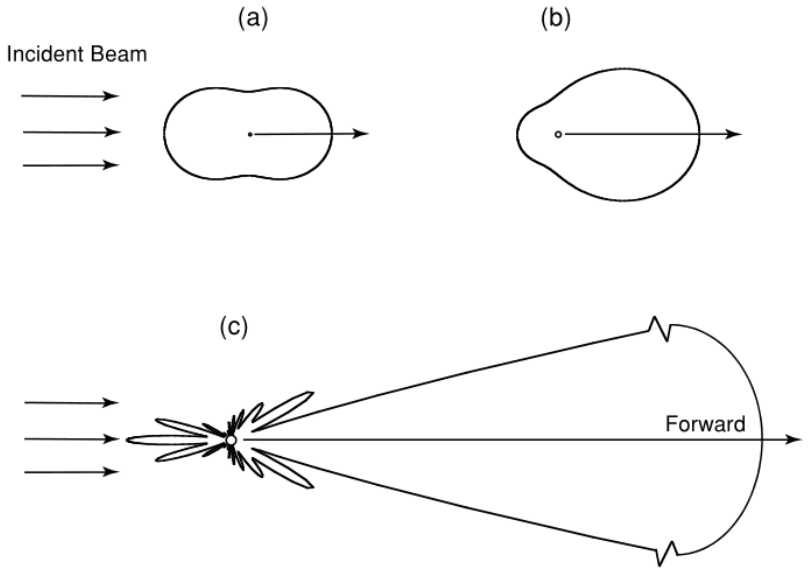


**Figure 1.5:** Angular distribution of scattered light (500 nm) by particles of dimension (a) 0.0001 $\mu$m, (b) 0.5 $\mu$m, (c) 1 $\mu$m. From [9].

where $\theta$ is the scattering angle, $m$ is the refractive index and $\lambda$ is the wavelength. For the Rayleigh isotropic scattering the phase function is given by

$$p_{\mathrm{R}}(\theta) = \frac{3}{16\pi}\left(1+\cos^2\theta\right).$$

As the particle size increases, the angular distribution of scattered light becomes more complex and forward peaked (Figure 1.5).
The average of the cosine of the scattering angle is called asymmetry factor

$$g = \langle cos\theta \rangle = \int_{4\pi} p\cos\theta d\Omega. \tag{1.20}$$

If the scattering is isotropic or symmetric respect to $\theta = 90°$ then $g = 0$. It assumes positive values if the particle scatters more light in the forward direction, or negative values, more light is scattered in the backward direction.
Another useful quantity is the single scattering albedo

$$\tilde{\omega} = \frac{\beta_{\mathrm{sca}}}{\beta_{\mathrm{ext}}} \tag{1.21}$$

where

$$\beta_{\mathrm{ext/sca}} = \int_{r_1}^{r_2} \sigma_{\mathrm{ext/sca}}(r)n(r)dr.$$

It represents the percentage of light beam which will undergo scattering in a single scattering event.
Very useful in lidar applications is the backscatter coefficient:

$$\beta = N\frac{d\sigma_{\mathrm{s}}(\theta=\pi)}{d\Omega},$$

where $N$ is the concentration of the scattering particles and $d\sigma_{\mathrm{s}}(\theta=\pi)/d\Omega$ is the differential scattering cross section for a scattering angle of 180°.

## 1.5 Aerosol observations

Aerosols can be observed in situ or through remote sensing techniques [11]. For in situ measurements, the instrument is in direct contact with aerosols. Aerosols can be collected and subsequently analyzed in the laboratory (chemical analysis can be performed, some optical properties can be determined, or they can be analyzed using an electron microscope), or they can be analyzed directly on-site, for example, by examining how the light emitted by a laser source is scattered by the particles. The main disadvantage of in situ observations is that they disturb the environment in which the particles are located and can provide only a limited amount of data both in time and space.
For this reason, for aerosol monitoring, given the importance of these particles within the atmosphere, remote sensing techniques are widely used. These techniques are based on the interaction of electromagnetic radiation with the particles of interest and can be passive or active. In passive remote sensing, the light emitted by a natural source is observed, which can be the sun, the moon, or even the stars, after it has interacted with the particles. The main instrument in this category is the sun photometer. On the other hand, in active remote sensing, the source is artificial, such as the pulsed laser used in atmospheric lidars (Chapter 4).

# Chapter 2

# Ultra high energy cosmic rays

## 2.1 Introduction

Cosmic rays are high-energy particles, primarily protons or heavier nuclei, that travel through space and reach our planet. Since their discovery over a century ago in 1912, the study of these particles has contributed significantly to the development of subnuclear physics, and today, cosmic rays continue to attract the interest of numerous physicists worldwide.
Cosmic rays with energies exceeding 1 EeV ($10^{18}$ eV) are referred to as ultra-high-energy cosmic rays (UHECRs), which are the focus of this work. When these particles interact with the atmosphere, they produce secondary particles that, in turn, can interact with atmospheric molecules again, giving rise to a cascade of particles known as an extensive air shower (EAS).

This chapter introduces the history of cosmic rays, their characteristics, and describes extensive air showers. Finally, methods for detecting cosmic rays are introduced.

## 2.2 Discovery

The discovery of cosmic rays dates back to the early years of the twentieth century when the Austrian physicist Victor Hess conducted a series of high-altitude ionization measurements, observing an increase in ionization levels during ascent.
The history of the discovery, however, involves many European and American scientists and is quite fascinating [15].

In 1896, Becquerel made the discovery of spontaneous radioactivity, and at the beginning of the twentieth century, many physicists were interested in studying it. The instrument used to detect it was the electrometer, which, in the presence of a radioactive material capable of ionizing the air within the instrument, promptly discharges. The time taken for the electrometer to discharge was used as a measure of the level of radioactivity.
It was observed that the discharge of the electrometer also occurred in the absence of radioactive sources, suggesting the presence of additional radiation capable of ionizing the air. The simplest hypothesis was that this radiation originated from radioactive material in the terrestrial crust.

The first to propose an extraterrestrial origin for this radiation was Father Theodor Wulf. To test his idea, he conducted a series of measurements of radioac-

tivity as a function of altitude. In 1909, he measured the ionization rate at the top of the Eiffel Tower (300 m above ground level), expecting, under the assumption of terrestrial origin for this radiation, a lower value compared to that measured on the ground. A decrease was indeed measured, but it wasn't sufficient to confirm the prevailing hypothesis at that time.

In the following years, the Italian physicist Domenico Pacini compared the ionisation rate in function of the environment. He observed no changes in his measurement on the ground and on the sea. The Italian physicist continued his observations, and in 1911, he conducted measurements of radioactivity underwater, finding a significant decrease in the discharge rate of the electroscope. These measurements were consistent with water absorption of a radiation coming from outside.

Despite these recent measurements, physicists generally hesitated to dismiss the hypothesis of terrestrial origin for this radiation. The puzzle pieces fell into place, however, when in 1912, Victor Hess, during a series of balloon ascents up to 5000 meters, observed that after an initial decrease, the radiation increased with altitude, suggesting an extraterrestrial origin. Hess's results were then confirmed with a series of ascent up to 9200 m by Kolhörster. The term 'cosmic ray' was coined in 1926 by Robert Millikan, initially skeptical about Hess's conclusions.

In 1934, Bruno Rossi, by placing three particle detectors on a horizontal plane, observed a large number of coincidences (the three detectors were triggered simultaneously), discovering the particle cascades [16]. In the following years, the studies on particle showers were carried out by Pierre Auger, who discovered the existence in nature of particles with energy above $10^{15}$ eV [17].

## 2.3 UHECR sources

Determining the source of cosmic rays poses a formidable challenge. Charged particles interact with the galactic magnetic field, resulting in the loss of arrival direction information, thereby complicating the identification of cosmic ray origins. The effects of the galactic magnetic field, however, become negligible for particles at higher energies, allowing for the identification of UHECRs galactic sources.

The primary hypothesis regarding the origin of UHECRs suggests that these particles are accelerated within certain astrophysical objects through electromagnetic processes (bottom-up models). The presence of particles with energies on the order of $10^{20}$ eV poses challenges to models of particle acceleration, because the extremely high energies of these particles exclude the majority of the accelerating mechanisms, and because these particles cannot be confined within our Galaxy's disk by its magnetic fields [18]. In fact, particles can only be accelerated by these processes up to a maximum energy given by [19]

$$E < \frac{1}{2}\frac{B}{\mu G}\frac{L}{pc}Z\,\mathrm{PeV}, \tag{2.1}$$

where $B$ is the strength of the magnetic fields within the astrophysical object, $L$ its size, and $Z$ is the charge of the accelerated particle. This limit is due to the fact that once the Larmor radius of the accelerated particle exceeds half the size of the astrophysical object, the particle is free to escape from the acceleration region. Hillas proposed a two dimensional plot of $B$ and $L$ for for various astrophysical objects, known as Hillas plot, that can be used to identify (or exclude) possible

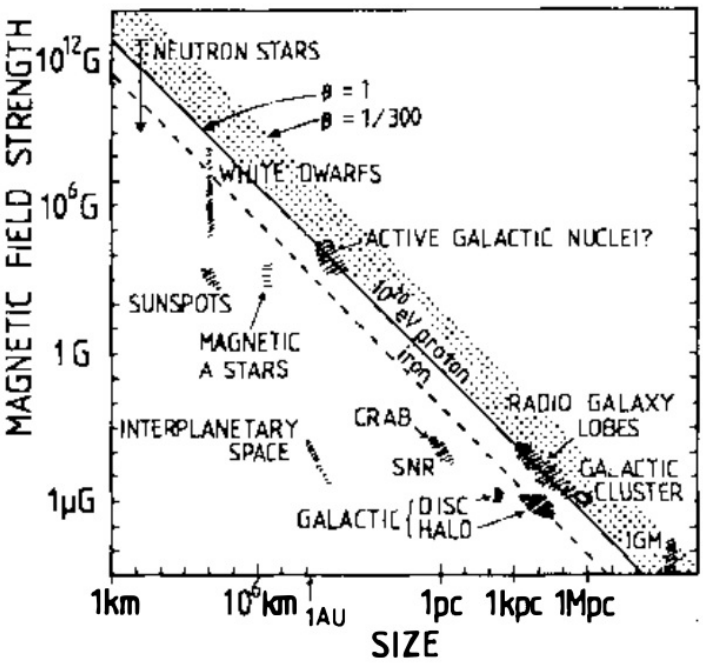


**Figure 2.1:** Size and magnetic field strength of possible sites of particle acceleration. Objects below the diagonal line cannot accelerate protons to $10^{20}$ eV. From [18].

cosmic ray sources (Figure 2.1). From the Hillas plot, it can be noted that only few sources can accelerate particles up to $10^{20}$ eV.

A second kind of mechanism for particle acceleration suggests that UHECRs originate from the decay of superheavy particles formed in the primordial universe (top-down models).

## 2.4 Properties

### 2.4.1 Energy spectrum

The number of cosmic rays reaching the Earth decreases rapidly at high energies. The differential flux of particles as a function of energy is called the energy spectrum $J(E)$, and the quantity $\gamma = -\frac{dlnJ}{dlnE}$ is referred to as the spectral index. For UHECRs, the energy spectrum can be described by a power law

$$J(E) \propto E^{-\gamma},$$

with $\gamma \approx 3$ (Figure 2.2). The spectrum has some interesting features highlighted by the spectral index variations such as the knee at $E_{knee} \approx 3 \times 10^{15}$ eV, the ankle at $E_{ankle} \approx 5 \times 10^{18}$ eV, and the cutoff at $E_{cut-off} \approx 40 \times 10^{18}$ eV. Around the knee (a second knee is present at $E \approx 4 \times 10^{17}$ eV where the spectrum steepens again) the spectral index changes from $\gamma = 2.7$ to $\gamma = 3.3$ while it returns to $\gamma = 2.7$ after the ankle. This latter feature has been interpreted as a transition from galactic sources to extragalactic sources of cosmic rays or as the pair production dip [21].

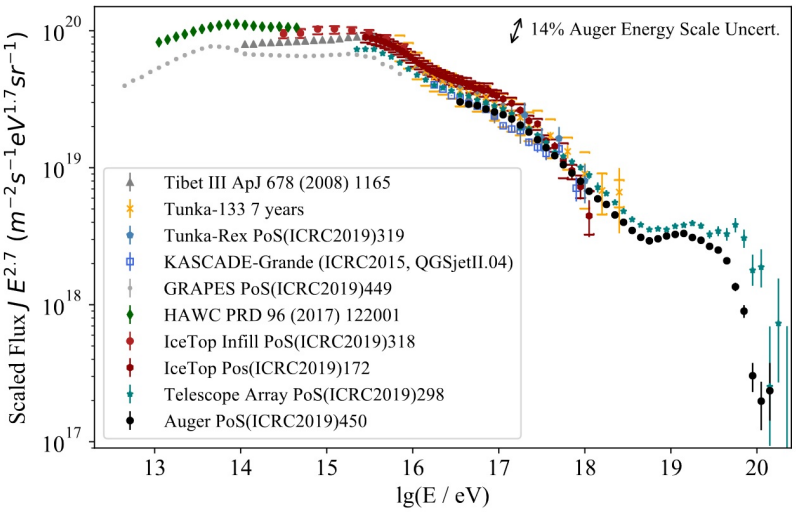


**Figure 2.2:** Energy spectrum of high-energy cosmic rays. From [20].

### 2.4.2 Mass composition

The composition of cosmic rays for energy up to $10^{14}$ eV can be assessed using space-based instruments. It is interesting to compare the composition of cosmic rays with that of astrophysical objects to obtain information about their sources [23]. As shown in Figure 2.3, the mass composition typically mirrors the abundance found in the solar system, with light nuclei being the predominant component. Interestingly, there seems to be an excess of lithium, beryllium, and boron in cosmic rays compared to their abundances in the solar system. This difference can be explained by the fact that these elements are absent in stellar nucleosynthesis but are instead produced by the fragmentation of heavier nuclei in cosmic rays interactions with gas, dust, and the CMBR.
At higher energy, the composition of cosmic rays cannot be directly measured due to their extremely low flux, and must be inferred from the characteristics of the atmospheric showers.

## 2.5 Showers

A high-energy proton or other nucleus reaching the Earth, will interact hadronically with a nucleus in a molecule of the atmosphere. The produced secondary particles, fragments of the original nucleus and other hadrons such as pions, can in turn interact with atmospheric molecules to give rise to a particle cascade, known as extensive air shower (EAS). The number of particles in the cascade increases until it reaches a maximum and then decreases when the energy of the particles is no longer sufficient to produce new ones.
The coordinate used to measure lengths along a shower is the atmospheric depth $X$ [19, 23], defined as

$$X = \int_{+\infty}^{h} \rho(h)dx, \qquad dx = -\frac{dh}{\cos\theta}, \tag{2.2}$$

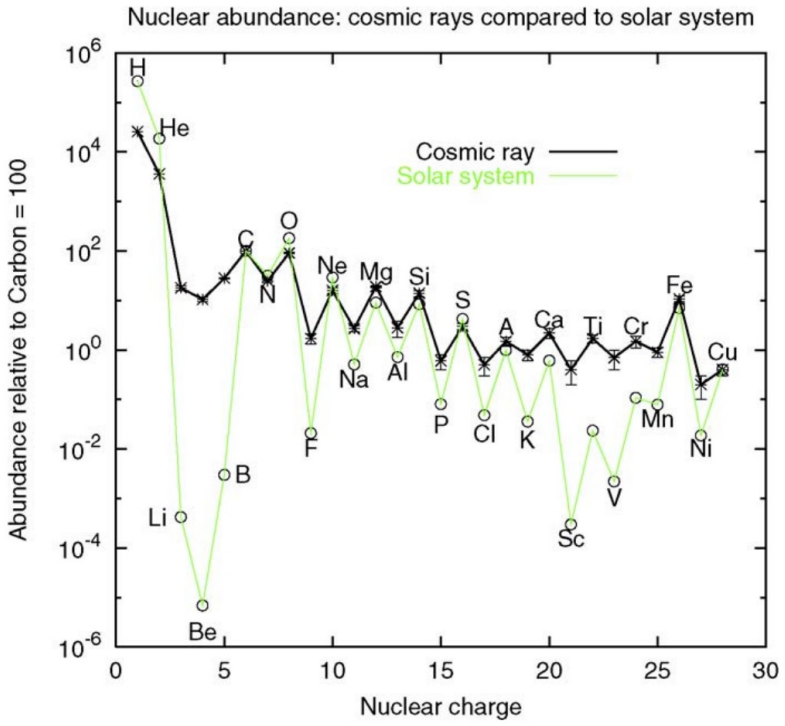


**Figure 2.3:** Comparison of Solar system and cosmic-ray elemental abundances. From [22].

where $\rho(h)$ is the air density at altitude $h$, and $\theta$ is the zenith angle. When a nucleon passes through an infinitesimal element of atmosphere $dX$, the probability of interaction is given by $dX/\lambda_N$, with $\lambda_N$ the nucleon interaction length in air [23]. The parameters describing the development of a shower include its size $N(X)$, the number of particles as a function of the atmospheric depth traversed, and the atmospheric depth $X_{max}$ at which N reaches its maximum value. The energy deposited per unit atmospheric depth follows the same trend as the number of particles and can be parametrized by the Gaisser-Hillas function [24]:

$$\frac{dE}{dX} = \left(\frac{dE}{dX}\right)_{\max} \left(\frac{X - X_0}{X_{\max} - X_0}\right)^{\frac{X_{\max}-X_0}{\lambda}} \exp\left(\frac{X_{\max} - X}{\lambda}\right), \tag{2.3}$$

with $X_0$ and $\lambda$ shape parameters. Furthermore, secondary particles are generated with a non-zero transverse momentum (relative to the direction of propagation of the primary particle), and when the shower reaches ground level, depending on the energy of the primary, it can span an area of hundreds of square kilometers. The particle density at a distance $r$ from the shower axis is called lateral distribution function (LDF) and can be described with the modified Nishimura-Kamata-Greisen (NKG) function:

$$S(r) \propto r^{\beta}(r + r_1)^{\beta+\gamma}, \tag{2.4}$$

with $r_1 = 700\,\text{m}$, and the parameters $\beta$ and $\gamma$ depends on the zenith angle and shower size.

When the cosmic ray enters the Earth's atmosphere, most commonly, the first interaction will produce both charged and neutral pions. Neutral pions decay quickly

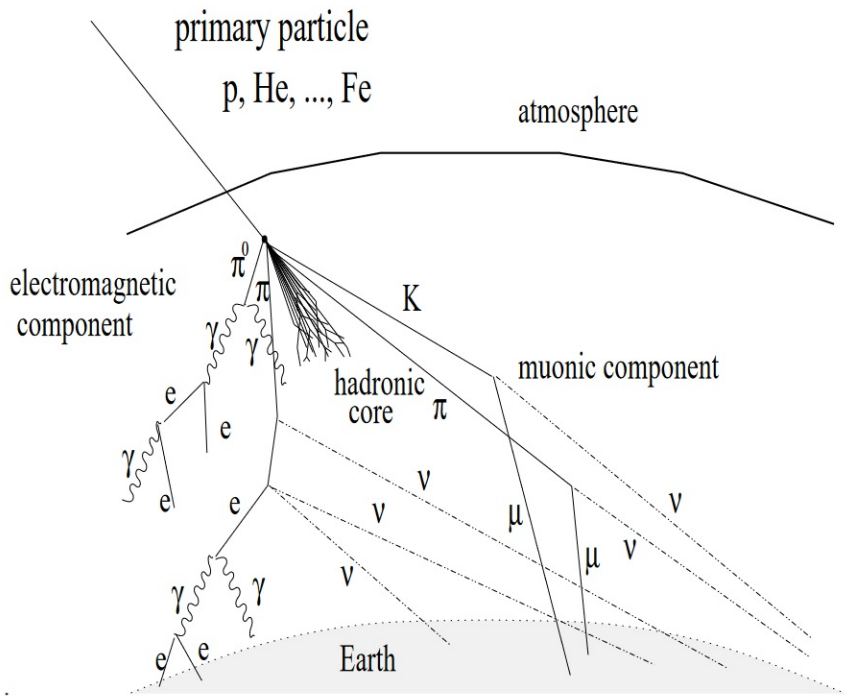


**Figure 2.4:** Schematic view of an air shower. From [25].

(lifetime $\tau_0 = 8.5 \times 10^{-17}$ s) into two gamma photons, thus giving rise to the electromagnetic cascade. Charged pions, on the other hand, decay into muons and neutrinos, but having a longer lifetime (26 ns), they can also undergo hadronic interactions with air nuclei. To sum up pions can decay as

$$\pi^0 \to \gamma + \gamma,$$

$$\pi^+ \to \mu^+ + \nu_\mu,$$

$$\pi^- \to \mu^- + \bar{\nu}_\mu.$$

As a consequence, there are three main components of such a shower: a hadronic component, an electromagnetic component, and a muonic component.

### 2.5.1 Electromagnetic component

Neutral pions decay quickly in two gamma photons. These photons will undergo pair production, with the creation of an electron-positron pair. Electrons and positrons will then undergo Bremsstrahlung photon emission, starting the electromagnetic shower component.
The number of particles increases until the average energy of each particle reaches the critical energy $E_c$ (at which the energy loss due to radiation is equal to the energy loss due to ionization) and then starts to decrease.

The development of the electromagnetic cascade can be described by a simple model devised by Heitler [26]. According to this model, each electron with energy $E_0$ much greater than $E_c$, will emit a photon with half of the initial energy after traveling a radiation length $\lambda$. In turn, the photon will give rise to an electron-positron pair to which it will transfer half of its energy. After $n = X/\lambda$ steps, the

particle number is given by

$$N(X) = 2^{\frac{X}{\lambda}}, \tag{2.5}$$

while the energy for each particle is

$$E(X) = \frac{E_0}{N(x)}. \tag{2.6}$$

The maximum size of the shower is

$$N(X_{\max}) = \frac{E_0}{E_c} \tag{2.7}$$

for

$$X_{\max} = \frac{\lambda \ln (E_0/E_c)}{\ln 2}. \tag{2.8}$$

The last equation says that $X_{\max}$ is proportional to $\ln E_0$, the energy of the particle that generated the cascade.

### 2.5.2 Hadronic component

If the primary cosmic ray consists of a nucleon or a nucleus, the cascade starts with a hadronic interaction. This hadronic component forms a dense shower core in an extensive air shower (EAS), which in turn feeds the electromagnetic shower component. The interaction of a primary cosmic ray with the atmosphere produces multiple hadrons, pions and kaons.
The maximum size depth $X_{\max}$ is proportional to $\ln E$, the energy of the primary particle and its value is linked to the nature of the primary cosmic ray.

As in the case of the electromagnetic component, the hadronic component of the shower can be described by a semi-empirical model similar to the Heitler model, the Heitler-Matthews model [27]. The atmosphere is divided into layers of thickness $\lambda_I \ln 2$, with $\lambda_I$ the interaction length for strongly interactive particles. After traversing an atmospheric layer, the hadrons interact, producing $N_{ch}/2$ neutral pions and $N_{ch}$ charged pions. The charged pions cross another layer and interact again, until the energy of the new charged pions falls below the critical energy and they decay, giving rise to muons. After $n$ layers, the energy of charged pions is thus

$$E_\pi = \frac{E_0}{\left(\frac{3}{2}N_{ch}\right)^n}, \tag{2.9}$$

with $E_0$ the energy of the primary particle. The neutral pions decay instead into photons which give rise to the electromagnetic shower. The primary energy $E_0$ is thus divided between the pions and the electromagnetic particles produced within the particle shower.
The model predicts for a proton induced EAS

$$X^p_{\max} = X_{\max} + X_0 - \lambda \ln 3N_{ch}, \tag{2.10}$$

where $X_{\max}$ is the depth of maximum of the electromagnetic component, $X_0 = \lambda_I \ln 2$ is the atmospheric depth of the first interaction, and $\lambda$ is the radiation length in the medium. This result can be extended to a nucleus with atomic number $A$ and energy

$E_0$ using the superposition model. The nucleus is treated as $A$ single nucleons of energy $E_0/A$ and the depth of maximum development of the shower is given by

$$X^A_{\max} = X^{\mathrm{p}}_{\max} - \lambda \ln A, \tag{2.11}$$

while the primary energy is

$$E_0 = 0.85\,\mathrm{GeV}(N_e + 25N_\mu), \tag{2.12}$$

with $N_e \approx \frac{2}{3}N_{\max}$ (the Heitler model overestimates the ratio of electrons to photons), and $N_\mu$ the number of muons ($N_\mu = N_\pi$).
Thus, from the observation of the extensive air showers, it is possible to obtain information about the nature and energy of the primary particle.

### 2.5.3 Muonic component

Muons can decay in electrons, positrons and neutrinos:

$$\mu^+ \to e^+ + \bar{\nu}_\mu + \nu_e,$$

$$\mu^- \to e^- + \nu_\mu + \bar{\nu}_e,$$

with an average lifetime $\sim 2.2\,\mu$s and can contribute to the electromagnetic component of an EAS. Moreover, thanks to relativistic effects, some muons can reach the ground and can be detected by the surface detectors. The arrival times of the muons enable the reconstruction of their geometric production heights along the shower axis, and since muons are produced from the decay of charged pions and kaons, the distribution of muons production depths contains information on the hadronic component [28]. Therefore, it is crucial to distinguish the muonic component from others and various efforts have been made in this direction within cosmic ray observatories.

## 2.6 Detection

Since the flux of cosmic rays reaching our planet decreases significantly at high energies, various techniques have been developed for their detection. In general, the aim is to detect a statistically significant number of events. The expected number of events detected by an observatory within an energy range is determined by the particle flux at that energy multiplied by the observatory's exposure. The latter quantity is defined as the integral of the aperture (the area of the observatory multiplied by its efficiency and the observed solid angle) over time and it is measured in $\mathrm{km}^2\,\mathrm{yr}\,\mathrm{sr}$.

The direct observation of primaries occurs for cosmic rays with energies up to $10^{15}\,\mathrm{eV}$, whose flux is sufficiently high. For this reason, detection apparatuses are relatively compact and can be mounted on balloons or satellites to detect particles before they interact with the atmosphere.

From energies of $10^{14}\,\mathrm{eV}$ and above, when the primary interacts with the atmosphere, a shower of secondary particles is produced, which can be detected. The indirect detection of cosmic rays involves precisely the observation of these secondary particles and the Cherenkov or fluorescence radiation produced.

The production of fluorescence light becomes significant for energies above $10^{17}$ eV. The number of fluorescence photons produced is directly proportional to the energy deposited by the shower in the atmosphere and is mainly due to the inelastic collisions of electrons and positrons with nitrogen molecules [29]. Photons are emitted in a wavelength range from 290 nm to 430 nm. The number of photons per wavelength interval $d\lambda$ and traversed atmospheric depth $dX$, can be expressed as

$$\frac{d^2N_\gamma^0}{dXd\lambda} = \int Y(\lambda, P, T, u, E)\frac{dN_\mathrm{e}}{dE}\frac{dE_\mathrm{dep}}{dX}dE, \tag{2.13}$$

where Y is the fluorescence light yield which depends on the atmospheric pressure $P$, temperature $T$, humidity $u$, and in principle on the energy of the electrons $E$, $dN_\mathrm{e}/dE$ is electron energy spectrum, and $dE_\mathrm{dep}/dX$ is the energy deposited in a layer of atmosphere.
Regarding the UHECRs, there are two main types of detectors: surface detectors (SDs) and fluorescence detectors (FDs). Surface detectors are arrays of ground particles detectors, such as plastic scintillator or water Cherenkov detectors, which detect secondary particles that survive down to ground level. SDs allow the retrieval of the lateral distribution function of the shower, have a duty cycle of almost 100 %, but the estimation of primary particle's energy is strongly model-dependent.
On the other hand, fluorescence detectors are telescopes observing the fluorescence light emitted after the passage of charged secondary particles. They allow the reconstruction of the longitudinal development of the shower and the estimation of the shower maximum depth $X_\mathrm{max}$ and the maximum size of the shower $N(X_\mathrm{max})$ which are linked to the nature and energy of the primary particle. The main disadvantage of fluorescence detectors is that they can only operate at night and under good atmospheric conditions. In this case, the duty cycle is on the order of 15 %. The observations are further complicated by the fact that in order to infer the number of produced fluorescence photons from the observed ones, it is necessary to accurately know the atmospheric conditions. The number of detected fluorescence photons is indeed given by [29]

$$\frac{dN_\gamma}{dX} = \int \frac{d^2N_\gamma^0}{dXd\lambda}T_\mathrm{atm}(\lambda, X)\epsilon_\mathrm{FD}(\lambda)d\lambda, \tag{2.14}$$

where $T_\mathrm{atm}$ is the transmission of the atmosphere, and $\epsilon_\mathrm{FD}$ is the efficiency of the fluorescence detector. The atmospheric conditions therefore influence both the transmission of fluorescence light and its production (fluorescence light yield in Eq. 2.13) and not considering its effects can introduce systematic errors. As an example, at the Pierre Auger Observatory (see Chapter 3), the systematic uncertainties on air fluorescence measurements, due to the aerosol optical depth, are of 4-8 % for shower energy, and 4-8 g cm$^{-2}$ for $X_\mathrm{max}$ [30].

In the most modern observatories, both types of detectors are implemented (hybrid detectors) allowing the measurement of the same properties of the primary particles using different techniques with different systematic uncertainties. Thanks to hybrid events, which are those detected by both the Surface Detector (SD) and the Fluorescence Detector (FD), it is possible to calibrate the SD events using fluorescence measurements and thus study cosmic rays with the high efficiency of the SD, and reducing the dependence on hadronic interaction models.

## 2.7 Recent advances in UHECR physics

Despite many years have passed since the discovery of cosmic rays, many questions regarding their origin and propagation remain open. This section presents the latest results obtained from the study of ultra-high energy cosmic rays at the Pierre Auger Observatory [31].

In Figure 2.5, a combination of energy spectrum measured with the surface detector and fluorescence detector of the Observatory is reported. The fit is obtained using a function of six power-laws [32].
In the energy spectrum, it is possible to identify points, with unprecedented accuracy thanks to the enormous exposure accumulated at the Pierre Auger Observatory, where the spectral index changes. For the first time, the low energy ankle which, as the second knee, is probably due to the change of composition of galactic cosmic rays, has been identified at $(2.8 \pm 0.3 \pm 0.4) \times 10^{16}$ eV. The other inflection points are the second knee at $(1.58 \pm 0.05 \pm 0.2) \times 10^{17}$ eV, the ankle at $(5.0 \pm 0.1 \pm 0.8) \times 10^{18}$ eV, the instep at $(1.4 \pm 0.1 \pm 0.2) \times 10^{19}$ eV, and the suppression at $(4.7 \pm 0.3 \pm 0.6) \times 10^{19}$ eV. The first uncertainty is statistical and the second one systematic.

The best observable for mass composition estimation is the depth of the maximum size of the shower $X_{\max}$. The mean of this parameter is in fact related to the mass of the primary cosmic ray (Eq. 2.11). From Auger observations it can be inferred that the cosmic ray flux of energy above $10^{17}$ eV consists of atomic nuclei, whose mass decreases with energy until reaching a minimum around $3 \times 10^{18}$ eV, and then increases again. Figure 2.6 shows how much, different primary mass groups, contribute to the total flux. The reported fractions are the result of the fit of the distributions of $X_{\max}$ [33].

Another fundamental element for the study of cosmic rays is their arrival direction as it can provide important information about their sources. In the left panel of Figure 2.7, a map of the cosmic ray flux for energy above 8 EeV is shown in equatorial coordinate. A dipolar modulation is found, with the dipole pointing 115° away from the Galactic center, suggesting an extragalactic origin for these cosmic rays [34]. The dipole directions in different energy bins are reported in the right panel of Figure 2.7 and no clear trend is observed in the change of direction of the dipole as a function of energy.

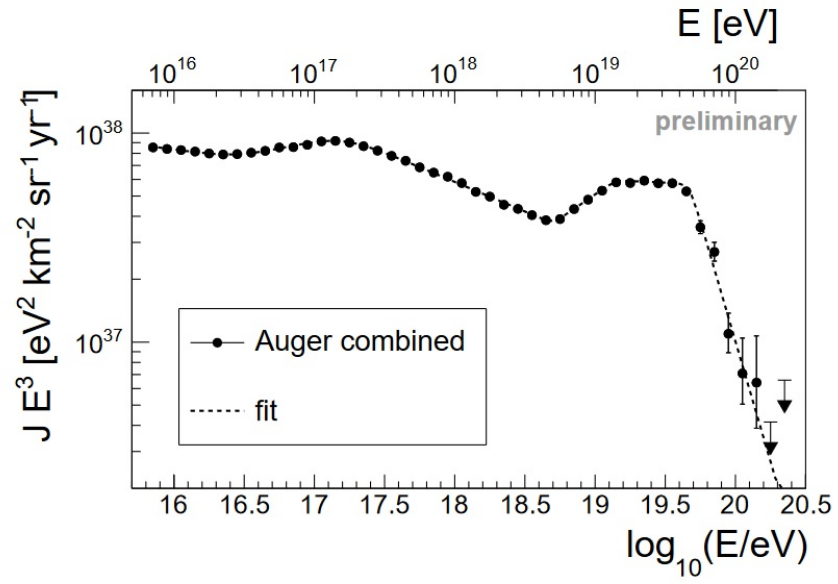


**Figure 2.5:** Combined energy spectrum multiplied by $E^3$ together with the fit function. From [32].

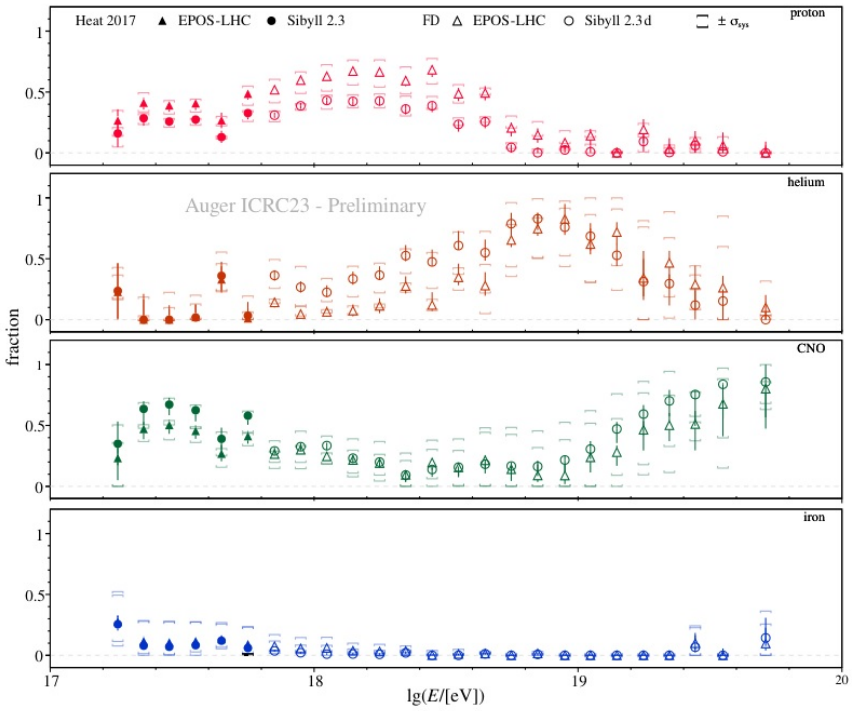


**Figure 2.6:** Fits of the fractional mass composition of the UHECR flux from $X_{\max}$ data. Fits are performed for p, He, CNO, and Fe.

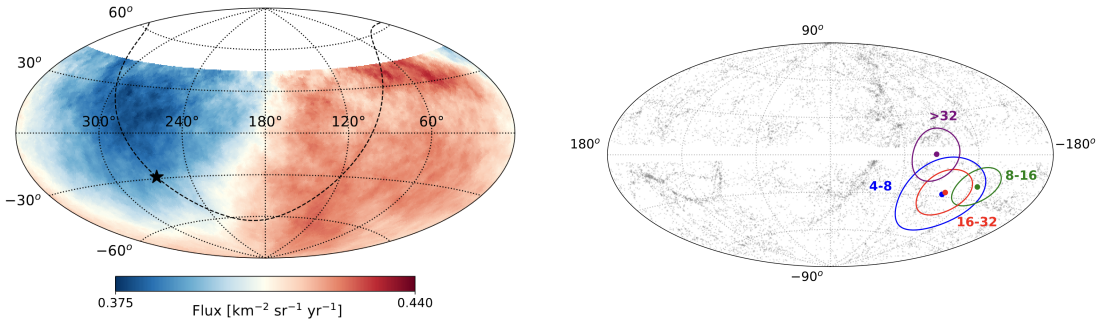


**Figure 2.7:** Left panel: map of the flux of cosmic rays above 8 EeV in equatorial coordinates averaged on top-hat windows of 45° radius. Right panel: reconstructed dipole directions in different energy bins and corresponding 68% C.L. uncertainty, in Galactic coordinates. The dots indicate the positions of 2MRS galaxies within 100 Mpc. From [34].

# Chapter 3

# The Pierre Auger Observatory

## 3.1 Introduction

The Pierre Auger Observatory is the world's largest operating cosmic ray observatory [35]. It is located in the Argentinian Pampa Amarilla, in the Mendoza Province, and it covers an area of about $3000\,\mathrm{km}^2$ at an altitude of about 1400 m above sea level. The main purpose of the Observatory is to study the origin of ultra high energy cosmic rays, particles with energy above $10^{18}\,\mathrm{eV}$, and how these particles propagate through space and interact with the environment. Considering that the flux of particles of the highest energy which the Earth rapidly decreases with energy, their detection requires detectors covering large areas. The construction of the observatory was completed in 2008, and since then measurements have been carried out with an exposure exceeding $40000\,\mathrm{km}^2\,\mathrm{sr\,yr}$.

Like the most modern observatories, the structure of the Pierre Auger Observatory is hybrid. It consists of a surface array of 1660 water Cherenkov detectors arranged on a triangular grid and separated by 1500 m, and two smaller array with station separated by 750 m and 433 m (Surface Detector, SD). The area above the SD is overlooked by four optical stations, each composed of six telescopes, which collect fluorescence light emitted by nitrogen molecules excited by extensive air showers (Fluorescence Detector, FD). In addition to these 24 telescopes, in 2010 three fluorescence telescopes with high elevation field of view (HEAT) were added. EASs recorded by both SD and FD are labeled as hybrid events and allows the study of properties of primary cosmic rays with different systematic uncertainties, allowing an intercalibration of the two systems.
Besides the shower detectors, there are many atmospheric monitoring instruments for the retrieval of height-dependent state of the atmosphere. The knowledge of the state of the atmosphere is necessary for a correct reconstruction of atmospheric showers. An overview of the Observatory area is reported in Figure 3.1.

In addition to the astroparticle physics, the observatory has also produced significant results in various other domains, with a particular emphasis on atmospheric electricity phenomena such as lightning, terrestrial gamma ray flashes and ELVES [37].

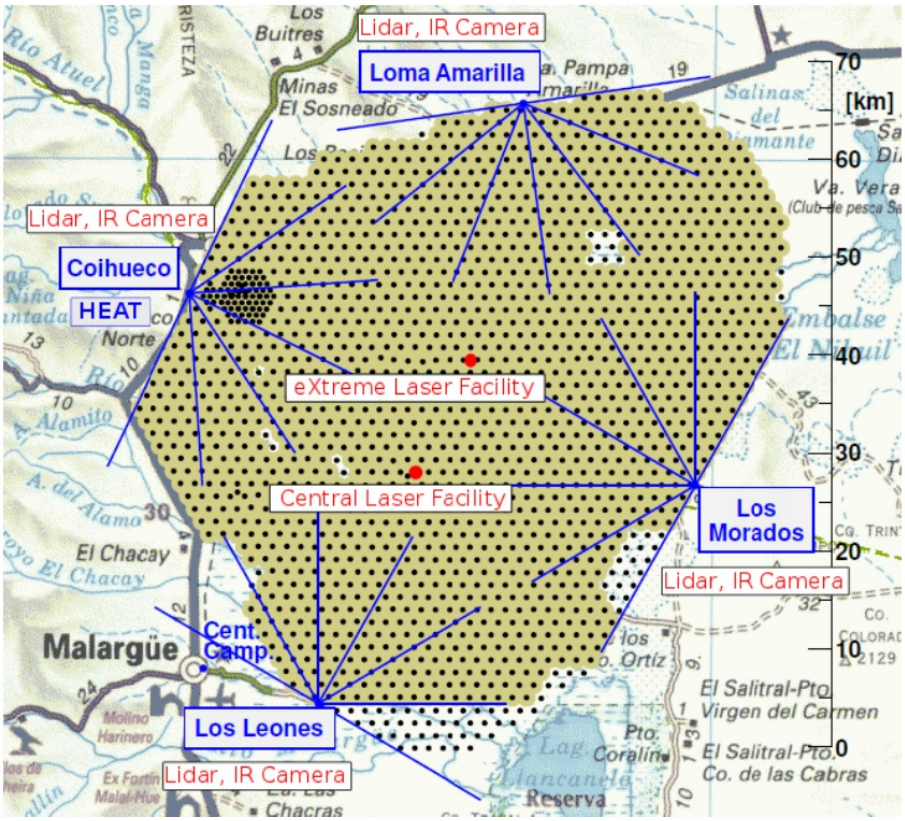


**Figure 3.1:** The Pierre Auger Observatory area. From [36].

## 3.2 SD detectors

The SD consists of an array of 1600 water Cherenkov detectors (WCD) arranged on a triangular grid with a spacing of 1.5 km (SD-1500) plus a smaller nested array of 61 additional detectors spaced by 750 m (SD-750) [38] and a further array of 19 WCD separated by 433 m (SD-433) [39], which extends the minimum threshold for the study of cosmic rays down to $5 \times 10^{16}$ eV. This kind of detectors was chosen because of its high solidity and low cost. The spacing between each detectors is the result of a compromise between cost-effectiveness and energy threshold. In fact, despite the main purpose of the observatory is the detection of cosmic rays with energy greater than $10^{18}$ eV, the observation of cosmic rays with lower energy allows important cross-checks with other experiments. The SD has a duty cycle of almost 100 %, allowing to record a large number of events.
Each water Cherenkov detector includes a 3.6 m diameter water tank containing a sealed liner with a reflective inner surface. The liner contains 12000 l of pure water with which charged particles can interact. When particles pass through the water volume, three nine-inch photomultiplier tubes (Photonis XP1802) collect the produced Cherenkov light. The PMTs are symmetrically distributed on the surface of the liner at a distance of 1.20 m from the center of the tank and look downwards through windows of clear polyethylene into the water. Each station is equipped with solar panels, a GPS receiver, a radio transceiver and a power controller [40]. A schematic view of the detector is in Figure 3.2.

When an extensive air shower is detected by the surface detector, the direction of the primary particle is obtained comparing the arrival times of the shower front at

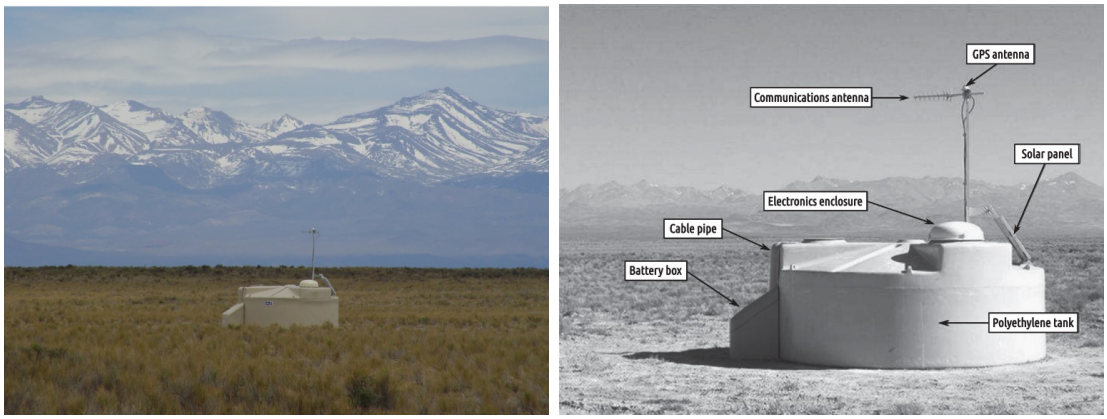


**Figure 3.2:** A surface detector station. On the right side a schematic view of the detector. From [35].

different surface stations. Because the number of triggered stations increases with energy and zenith angle, the angular resolution do the same.
The estimation of the energy of the primary particle is performed using the Lateral Distribution Function (LDF) or more precisely, by the particle density at a distance of 1000 m from the core of the shower S(1000). Within the Pierre Auger Observatory the lateral distribution is fitted to a modified NKG (Nishimura-Kamata-Greisen) function [35]:

$$S(r) = S(1000)\left(\frac{r}{1000}\right)^{\beta}\left(\frac{r+700}{1700}\right)^{\beta+\gamma} \tag{3.1}$$

where r is the distance to the shower axis in meters, and the S(1000) parameter is the energy estimator for the SD events. The conversion from S(1000) to energy is done through air shower simulations making the energy retrieval model dependent and introducing a systematic error related to the choice of the model.

## 3.3 FD detector

The Fluorescence Detector allows to follow the longitudinal development of the shower by detecting the fluorescence light in the 300-430 nm range due to the interaction of charged secondary particles with the Earth's atmosphere. The FD operates during moonless nights and under good atmospheric conditions. Hence the duty cycle is of the order of 10 %.
The FD consists of 24 telescopes located in four sites: Los Leones, Los Morados, Loma Amarilla, and Coihueco. Each building is climate-controlled and houses six telescopes with a field of view (FOV) of 30° x 30° for an overall FOV of 180° in azimuth and 30° in elevation [41]. The Observatory has been designed so that any event recorded by the FD is also seen by the SD. With the three additional HEAT telescopes cosmic rays with ten times lower energy ($10^{17}$ eV) can be detected observing the atmosphere at greater elevations.
The optical design of the telescope is essentially a modified Schmidt which corrects spherical aberration and coma (Figure 3.3).
Before reaching the primary mirror, the light passes through a circular diaphragm of 1.1 m radius covered with a Schott MUG-6 filter. This filter absorbs visible light

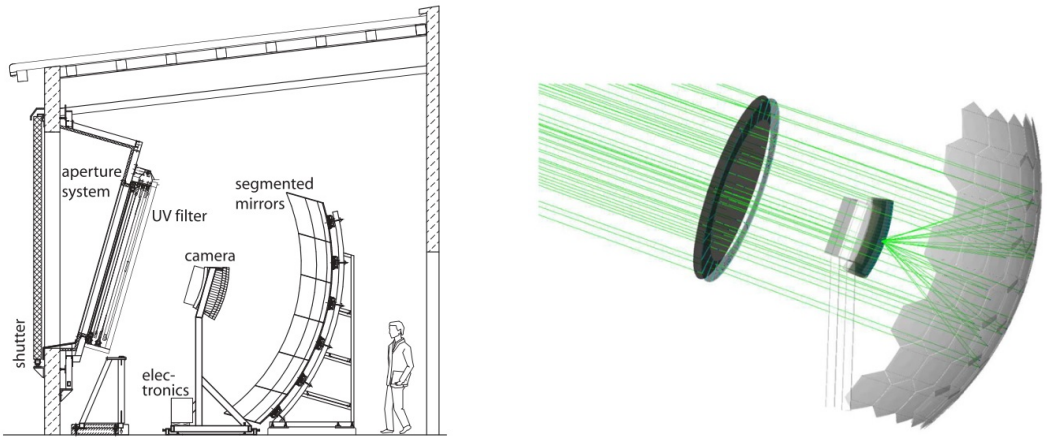


**(a)** **(b)**

**Figure 3.3:** On the left side a schematic view of a fluorescence telescope. On the right side a ray tracing simulation of the optical system. From [41].

**Figure 3.4:** FD building at Los Leones. From [35].

allowing the detection of the transmitted UV photons (nitrogen fluorescence spectrum included). A corrector ring is used to minimize aberrations and to simplify the production. Light is then focused by a mirror of 3.6 m diameter onto a camera of 440 pixels with photomultiplier tubes. Due to the large area, the primary mirror is segmented with two segmentation configurations adopted: a tessellation of 36 rectangular anodized aliminum mirrors of three different size; a structure of 60 hexagonal glass mirrors [41].
The camera pixels are arranged in a matrix of 22 rows by 20 columns on a spherical surface of 1.743 m radius. The PMTs used are the hexagonal Photonis XP3062. Because between the photocatodes it is present a certain amount of area insensitive to light, to maximize light collection, the PMTs are surrounded by light collectors [41].

An example of geometric reconstruction of a shower with the FD is shown in Figure 3.5. To determine the geometry of an FD event, it is first necessary to identify the shower detector plane (SDP), the plane which includes the telescope and the shower axis. Subsequently, by using the arrival time of the signal at the $i$-th, it is possible to determine the shower axis. This is characterized by two parameters, the perpendicular distance $R_p$ from the camera to the track, and the angle $\chi_0$ between the track and the horizontal line. The $i$-th pixel is illuminated at the time [41]

$$t_i = t_0 + \frac{R_p}{c} \tan[(\chi_0 - \chi_i)/2], \tag{3.2}$$

where $\chi_i$ is the pointing direction of the $i$-th pixel, and the parameters $t_0$, $R_p$, and $\chi_0$ are obtained by fitting the experimental data.

Since the number of fluorescence photons is proportional to the number of secondary charged particles, the longitudinal development of the shower can be retrieved. The obtained profile is fitted with the Gaisser–Hillas function (Eq. 2.3) to gain information on the primary energy and nature.

## 3.4 AugerPrime

AugerPrime is an upgrade of the Observatory with the aim of trying to find answers to the following open questions [42]:

- understand the origin of the flux suppression;
- assess the potential presence of a fraction of protons at the highest energy levels;
- gain information about hadronic interactions, in a range of energy not accessible by man-made accelerators.

The main elements of the AugerPrime upgrade are a plastic scintillator above each water Cerenkov detector, an underground muon detector, new electronics of the SD stations, and radio antenna mounted on top of each surface detector unit [42]. More in details the upgrade includes:

- a surface scintillator detector (SSD) above each SD station which allows for a better knowledge of the shower composition;

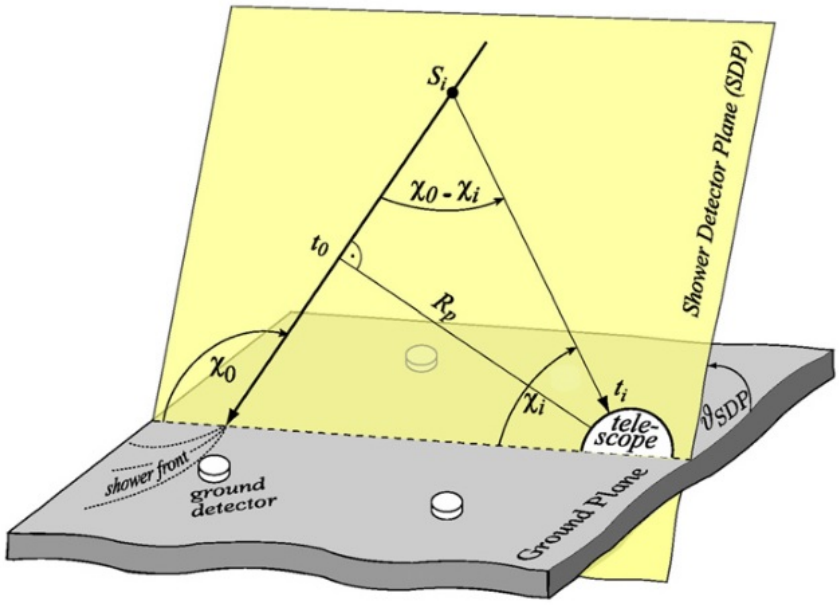


**Figure 3.5:** Reconstruction of the geometry of an extensive air shower. From [41].

- extended dynamic range of WCD by inserting a fourth small PMT (Hamamatsu R8619) at each surface station;
- a radio antenna (Radio Detector, RD) above each SD station which provides information on the composition of horizontal showers (zenith angle from 60° to 84°);
- new and faster electronics (Upgraded Unified Board, UUB) for the processing of signals from WCD, SSD and RD.
- an array of underground detectors to minimise the contamination from electromagnetic shower particles.

## 3.5 The Atmospheric Monitoring System

Atmospheric monitoring is a key function within the Observatory (and in general within astroparticle physics observatories [43]). The state of the atmosphere not only affects both the production and transmission of fluorescence light [29, 30], but also has an impact on observations with SD [44]. Also the Cherenkov light emission, which is detected by the Fluorescence Detector, and thus must be subtracted, is affected by the state of the atmosphere. Thus atmospheric data play a crucial role in accurately determining the shower energies and the depths of shower maxima.

The transmission of fluorescence light is attenuated by scattering and absorption by molecules and aerosols. The intensity of light that reaches the FD telescopes is given by [30]

$$I = I_0 T_{\mathrm{mol}} T_{\mathrm{aer}} (1 + H.O.) \frac{d\Omega}{4\pi} \tag{3.3}$$

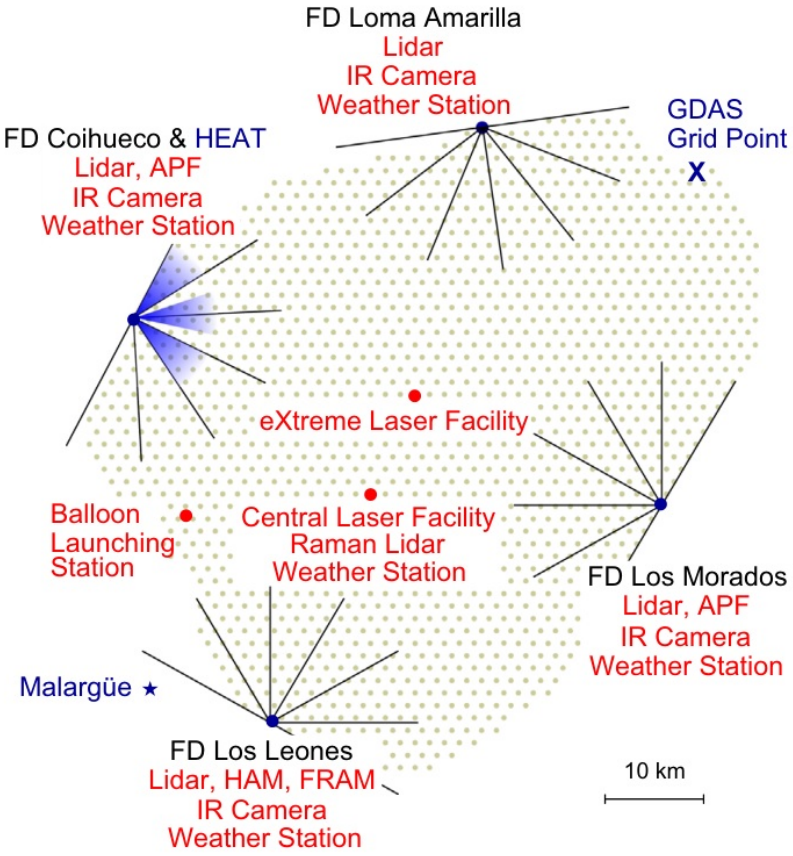


**Figure 3.6:** Overview of the Pierre Auger Observatory. The atmospheric monitoring instruments are shown. From [35].

where $I_0$ is the emitted intensity, $T_{\text{mol}}$ and $T_{\text{aer}}$ are the transmission factors due to molecules and aerosols respectively, $H.O.$ is a higher order correction to the Lambert-Beer law.
The attenuation due to aerosol scattering is less than the attenuation due to molecular (Rayleigh) scattering. However, the concentration of aerosols in the atmosphere exhibits much greater spatial and temporal variability than that of molecules. For this reason, in order to determine the emitted fluorescence light $I_0$, it is of fundamental importance to monitor the transmission factor due to aerosols. Within the Observatory the following aerosol properties are measured [45]:

- the vertical profile of the optical depth;
- the angular distribution of light scattered by aerosols;
- the wavelength dependence of the optical depth.

The locations of the atmospheric monitoring instruments are shown in Figure 3.6. In particular, at each FD site, there is a weather station, an infrared camera for cloud cover monitoring and an elastic lidar station for aerosols and clouds monitoring which scan the sky outside the field of view of the telescopes. Regarding the molecular part of the atmosphere, it is monitored with weather baloons, weather ground stations, and with GDAS (Global Data Assimilation System [46]). GDAS data are now used instead of balloon measurements. The aerosol properties are

instead monitored with instruments such as APF (Aerosol Phase Function), HAM (horizontal attenuation monitor), and FRAM (ph(F)otometric Robotic Atmospheric Monitor). The aerosol optical depth is retrieved observing with the FD the light scattered from two vertical laser beam emitted by the Central Laser Facility (CLF) and by the eXtreme Laser Facility (XLF) [47]. To all these instruments for aerosol monitoring, a Raman lidar has also been added at the CLF site (see Chapter 5).

## 3.6 Aerosol monitoring at the Pierre Auger Observatory

### 3.6.1 The Central Laser Facility and the eXtreme Laser Facility

The Central Laser Facility (Figure 3.7) is located approximately in the middle of the SD detector [48]. It is almost equidistant from three of the four FD buildings: Los Leones, Coihueco, and Los Morados.
The objectives of CLF include the atmospheric monitoring, the cross-checking of the absolute energy scale, and the improving of the geometric reconstruction of the showers. It also allows several FD monitoring tests, including measuring the relative timing and the relative calibration. The facility is an independent system, housed in a modified and insulated shipping container, with no externally wired connections.

The hardware configuration of CLF is outlined in Figure 3.8. The core of the system is a frequency tripled Nd:YAG laser (Big Sky Laser Technologies) which emits linearly polarized light pulses at 355 nm, with a width of 7 ns and a maximum energy per pulse of 7 mJ. Because the laser output contains some residuals of the first two harmonics, the beam is cleaned through the use of two harmonic beam splitters. A portion of the beam is then diverted into a photo-diode detector to measure the relative energy of each laser pulse.
A flipper mirror then selects between two vertical paths. If this mirror is flipped out the beamline, the light passes directly to the sky. Along this path a second energy monitor is also installed. If the mirror is rotated into the beamline, the light is sent to a steering head which can direct the beam towards any direction above the horizon. Along this path, it is possible to remotely insert a filter to attenuate the laser light. Since the laser beam is polarized, each beam path then contains a depolarizer which randomize the polarization.
A further important feature of the facility is that an optical fiber runs from CLF to the nearest SD tank Celeste to provide a simultaneous signal in both the SD and the FD. The entire system is controlled by a single board computer which requires only 5 W of power.

In 2008 a similar structure, called eXtreme Laser Facility (XLF), was installed. Similarly to CLF, XLF is used with the FD to measure the aerosol optical depth in the line of sight of each FD telescope four times per hour.

**Figure 3.7:** The Central Laser Facility (CLF) and the SD tank Celeste. From [48].

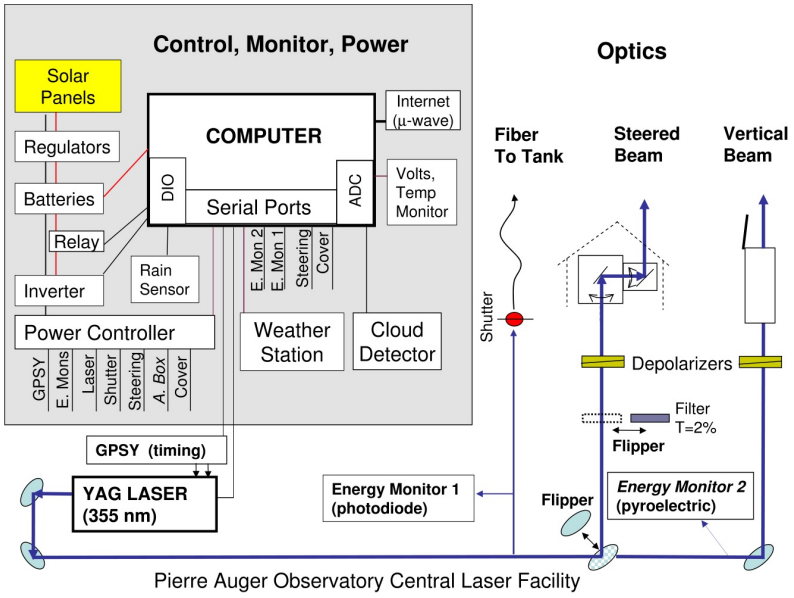


**Figure 3.8:** Schematic diagram of the CLF hardware. From [48].

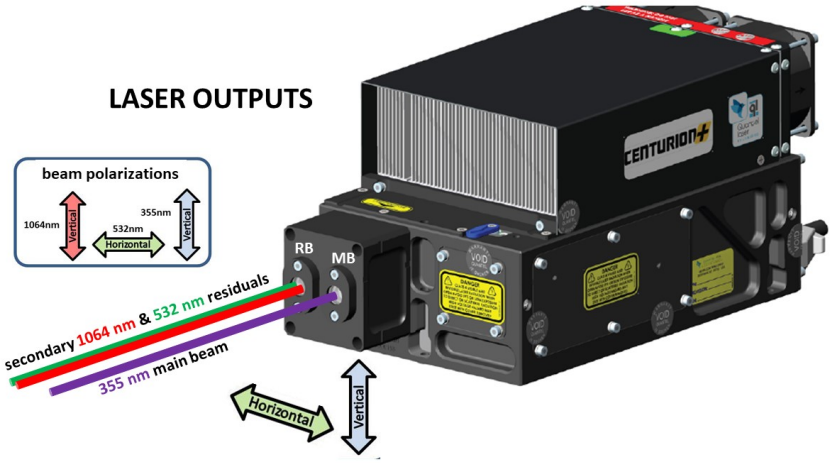


**Figure 3.9:** The layout of the Centurion+ laser with the characteristics (wavelength and polarization) of the emissions: 1064 and 532 nm Residual Beam (RB) and the Main Beam (MB) at 355 nm and vertical polarization.

### The new laser for CLF

In the lidar laboratory of DSFC/UNIVAQ, I performed tests of the new Centurion+ Quantel laser (Figure 3.9) which should replace the old one at CLF. The laser technical specifications are reported in Table 3.1.
The pulse energy measurements were conducted with the Thorlabs PM100D (PMC) console and the thermal sensor S310C (OPM), in the configuration depicted in Figure 3.10. The results of the measurements are shown in Figure 3.11. The left panel depicts the pulse energy of the 355 nm laser beam as a function of the Q-Switch delay: the energy increases until reaching its peak value at a Q-Switch delay of 131 µs, after which it begins to decrease. In the right panel, the laser pulse energy is graphed against the pump diode frequency, and the energy fluctuations fall within the measurement errors. An additional test involved measuring the light transmitted by the beam splitters (using a Q-Switch delay of 131 µs and a repetition rate of 10 Hz): the pulse energy transmitted at the backside of the first beam splitter, BS #1, was found to be $(0.44 \pm 0.01)$ mJ. This observation suggests the presence of residual laser light at other wavelengths within the main beam. The vertical polarization of the third harmonic of laser light was then confirmed using a Glan prism (Thorlabs GL15-A).
Also the divergence of the laser beam, obtained measuring the beam diameter at two different distances from the laser output, complies with the manufacturer's specifications.
To conclude, the overall performances are in agreement with the specifications, but dichroic beam splitters could be necessary to remove the residuals of the second and main harmonics.

## 3.6.2 Aerosol optical depth profiles

Every 15 minutes, 50 vertical laser shots are emitted by CLF and XLF. The tracks recorded by the FD telescopes are used to obtain hourly measurements of the vertical

**Table 3.1:** Beam parameters provided by laser manufacturer. The data are taken with the following settings: diode current 146 A; diode pulse width 130 µs; pulse rate 100 Hz; Q-Switch delay 131 µs; pumphead temperature 43.0 °C

| Parameter | 355 nm | 532 nm | 1064 nm |
|---|---|---|---|
| Energy (mJ) | 8.65 | 9.36 | 24.9 |
| Near Field Beam width (mm), Major axis | 3.05 | 3.36 | 3.88 |
| Near Field Beam width (mm), Minor axis | 2.64 | 3.34 | 3.55 |
| Pulse Width - FWHM (ns) | 8.60 | 9.17 | 12.6 |
| Divergence (mrad), Major axis | 4.69 | 4.96 | 7.41 |
| Divergence (mrad), Minor axis | 4.38 | 4.38 | 7.19 |
| First Shot Stability (%) | 0.81 | 0.60 | 0.61 |

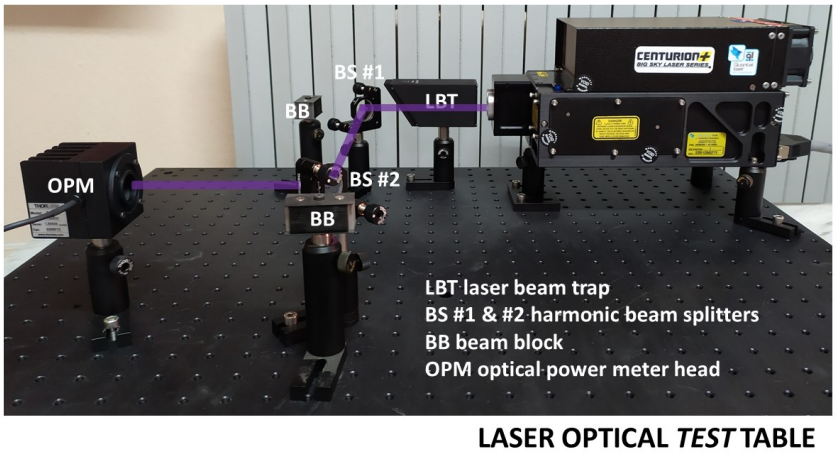


**Figure 3.10:** Setup used in the laboratory to perform pulse energy measurements. The main laser beam at 355 nm is indicated in violet; the residual beam goes directly into the beam trap. The 355 nm beams is sent to the optical power meter using two dichroic beam splitters BS #1 and BS #2.

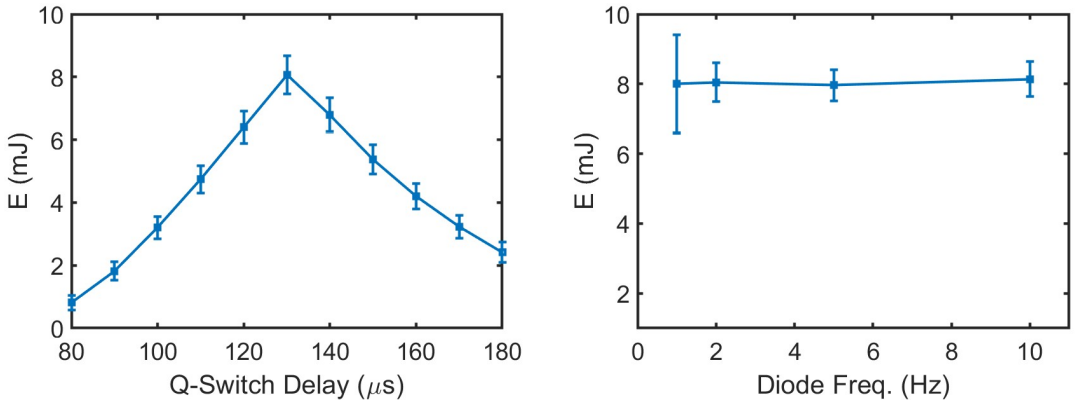


**(a)** **(b)**

**Figure 3.11:** (a) Pulse energy in function of Q-Switch delay at the repetition rate of 10 Hz. The maximum energy value occurs for a Q-Switch delay around 130 µs. (b) Pulse energy in function of diode frequency at the Q-Switch delay of 131 µs.

aerosol optical depth (VAOD or $\tau$).
Within the Pierre Auger Observatory two methods for the VAOD estimation have been developed [47]:

1. Data Normalization Analysis;
2. Laser Simulation Analysis.

In the Data Normalization Analysis the number of detected photons is converted to the number of photons of 1 mJ laser beam. Each set of 50 shots are used to build an average profile. Comparing the transmission $T_{aer}$ with the transmission of a reference clear nights $T_{clear}$, clouds and holes in the in the profile are identified and a maximum valid height $h_{valid}$ is determined.
For vertical laser shots, the vertical aerosol optical depth can be computed as

$$\tau_{aer}(h) = \frac{\ln N_{mol}(h) - \ln N_{obs}(h)}{1 + \mathrm{cosec}(\varphi_2)}, \tag{3.4}$$

where $N_{mol}$ is the number of photons from the reference clear profile, $N_{obs}$ is the number of photons from the observed hourly profile, and $\varphi_2$ is the elevation angle of the point of the laser beam, as observed by the FD. Between the ground and the bottom of the field of view of the FD telescope, the VAOD is obtained through interpolation.
In the Laser Simulation Analysis, the VAOD is instead obtained comparing the measured profile with simulated profiles under different atmospheric conditions. The aerosol distribution is assumed to be horizontally uniform and the aerosol attenuation is parametrized with a 2-parameter model:

$$\tau_{aer}(h_2 - h_1) = -\frac{H_{aer}}{L_{aer}} \left[ \exp\left(-\frac{h_2}{H_{aer}}\right) - \exp\left(-\frac{h_1}{H_{aer}}\right) \right], \tag{3.5}$$

where $L_{aer}$ is the aersol horizontal attenuation length, $H_{aer}$ is the aerosol scale height. The transmission along the path s between the laser beam and the FD telescope is

$$T_{aer}(s) = \exp\left( \frac{H_{aer}}{L_{aer} \sin\varphi_2} \left[ \exp\left(-\frac{h_2}{H_{aer}}\right) - \exp\left(-\frac{h_1}{H_{aer}}\right) \right] \right). \tag{3.6}$$

For each set of laser shots the values $L_{\rm aer}^{\rm best}$ and $H_{\rm aer}^{\rm best}$ are obtained and thus the aerosol attenuation.

### 3.6.3 Aerosol Phase Function Monitors

The angular distribution of light scattered by aerosols can be described by a phase function $P(\theta)$. While for molecular scattering the phase function behaves as $1+\cos^2\theta$ (in case of isotropic scattering), for aerosols it is much more complex and strongly depends on their size and shape.
Within the Observatory the aerosol phase function is measured on an hourly basis using two aerosol phase function (APF) light sources [49]. The APF monitors use a collimated broad-band Xenon flash lamp which operates between 300 nm and 400 nm. Light is directed horizontally across the FD field of view at Coihueco and Los Morados and signal observed by the ith pixel of the FD is:

$$S_i = I_0 T_i \left[ \frac{1}{\Lambda_{\rm m}} \left( \frac{1}{\sigma_{\rm m}} \frac{d\sigma_{\rm m}}{d\Omega} \right) + \frac{1}{\Lambda_{\rm a}} \left( \frac{1}{\sigma_{\rm a}} \frac{d\sigma_{\rm a}}{d\Omega} \right) \right], \tag{3.7}$$

where $I_0$ is the light source intensity, $T_i$ is the transmission of the atmosphere, $\Lambda_{\rm m}$ and $\Lambda_{\rm a}$ are the molecular and the aerosol extincion lengths, and $\sigma_{\rm m}^{-1} d\sigma_{\rm m}/d\Omega$ and $\sigma_{\rm a}^{-1} d\sigma_{\rm a}/d\Omega$ are the molecular and aerosol phase functions.
The aerosol phase function is parametrized by the Henyey–Greenstein function [50] (for pure forward scattering) plus a second term which describes the non-negligible backscattering:

$$P_{\rm a}(\theta) = \frac{1-g^2}{2\pi} \left( \frac{1}{(1+g^2-2g\cos\theta)^{3/2}} + f \frac{3\cos^2\theta - 1}{2(1+g^2)^{3/2}} \right), \tag{3.8}$$

where $\theta$ is the scattering angle, $g = <\cos\theta>$ is the asymmetry parameter, and $f$ is a parameter which describes the relative strength of forward to backward scattering. Therefore the scattering parameters are obtained performing the fit of the recorded signal with the following 4-parameter model:

$$S_i = A(1+\cos^2\theta_i) + B(1-g^2) \left( \frac{1}{(1+g^2-2g\cos\theta_i)^{3/2}} + f \frac{3\cos^2\theta_i - 1}{2(1+g^2)^{3/2}} \right). \tag{3.9}$$

### 3.6.4 Horizontal Attenuation Monitor

The aerosol attenuation is modeled by a falling power law of the wavelength. For the aerosol optical depth we can write

$$\tau(\lambda) \propto \lambda^{-\gamma},$$

where $\gamma$ is the Ängstrom exponent. This parameter is obtained by the Horizontal Attenuation Monitor (HAM) [45] which consists in a high intensity discharge lamp located next to the Coihueco FD site. The emitted light is then recorded by a filtered CCD camera at the Los Leones FD site and the horizontal atmospheric attenuation is obtained at five wavelengths between 350 and 550 nm. During 2006 to 2007 the average value of the Ängstrom exponent was $\gamma = 0.7$, value expected in desert-like environments.

### 3.6.5 FRAM

Another system for the measurement of the wavelength dependence of the optical depth is the (F/ph)otometric Robotic Telescope for Astronomical Monitoring (FRAM) [51] and it is located at the Los Leones FD site. FRAM is a robotic telescope for atmospheric monitoring through stellar photometry. This system does not emit any light and it has the advantage of not interfering with the FD observations. The operating principle is rather simple. The difference between the observed star brightness and the predicted value is due to the transparency of the atmosphere. Therefore it is possible to retrieve the atmospheric extinction observing stars at different altitudes above the horizon and the wavelength dependence of the aerosol extinction performing observations in several wavebands (astronomical photometric filters, such as the Johnson BVRI system, are usually used).

# Chapter 4

# Lidars for aerosols monitoring

## 4.1 Introduction

The atmospheric Lidar (light detection and ranging) is the only remote sensing instrument that allows for vertical characterization of the atmosphere with both high spatial and temporal resolution. Depending on the type of interaction with atmospheric constituents of the emitted radiation, it is possible to obtain profiles as a function of range, i.e., as a function of distance from the instrument, of various atmospheric characteristics such as temperature, humidity, wind, as well as measurements of aerosols, trace gases, and clouds.
The Lidar techniques that we will consider are the elastic-backscatter lidar and the Raman lidar. With the former only the elastically backscattered (Rayleigh-Mie scattering) emitted photons are recorded while with a Raman lidar the inelastic scattered light (Raman scattering) at a specific wavelength, the wavelength shift from the emitted light is a characteristic of the molecules, is recorded as well.
The primary products of a Raman lidar are the aerosol extinction coefficient and the aerosol backscatter coefficient:

$$\alpha_{\lambda}^{\mathrm{aer}}(z) = \int_0^{\infty} \pi r^2 Q_{\mathrm{ext}}(r, m, \lambda) n_{\mathrm{aer}}(z, r) dr,$$

$$\beta_{\lambda}^{\mathrm{aer}}(z) = \int_0^{\infty} \pi r^2 Q_{\mathrm{bck}}(r, m, \lambda) n_{\mathrm{aer}}(z, r) dr,$$

where $Q_{\mathrm{bck}}(r, m, \lambda)$ and $Q_{\mathrm{ext}}(r, m, \lambda)$ are the Mie backscattering and extinction efficiencies respectively, $n_{\mathrm{aer}}(z, r)$ is the aerosol size distribution, $r$ the particle size and $m$ the index of refraction. As a result, these coefficients depend on the shape and size of the scattering particles.
The ratio between these two quantities is called lidar ratio and provides information about the aerosol type [52]. Alongside lidar ratio, using multiple elastic and Raman channels leads to a better characterization of aerosols, yielding range-resolved microphysical properties such as effective radius and refractive index [53, 54].

After a brief introduction to the history of lidar, in this chapter, I will provide a general description of the structure of a lidar system for atmospheric monitoring, the basic form of the lidar equation that describes the acquired signals, and how, from these equations, it is possible to derive the aerosol properties of interest.

## 4.2 Lidar history

A valuable starting point for those interested in the historical aspects of lidar technique is represented by [55, 56]. It should be noted that in this brief historical overview, I have focused on works that more directly relate to my field of study. During my historical research, I came across other works of significant impact that should be mentioned in a more general history of lidar.

The introduction of the lidar technique predates the invention of the laser. The first one to introduce a technique for investigating the uppermost part of the atmosphere, approximately up to 50 km when measurements with sounding balloons did not extend beyond 20 km, was Synge in the 1930s [57]. Synge proposed to analyze the intensity of light, emitted by searchlight, scattered by atmospheric gas molecules. Assuming the composition of the atmosphere remains constant with altitude, the scattering is approximately proportional to the gas density. Synge also calculated that at an altitude of 30 km, the contribution of scattered light is negligible compared to the background, and the use of a large number of searchlights was necessary.
In 1935, Tuve proposed the use of a modulated light source [58]. In this approach, the background limit was no longer represented by all the light from the night sky entering the receiver, but only by the Fourier component with a frequency equal to that of the emitted light modulation.
The first observations in the upper atmosphere appeared in the 1937 [59] and in 1938 [60]. In the latter is also shown that the technique could be applied to measurements up to 90 km. In 1953, the first vertical profiles of atmospheric temperature were obtained [61].

In the same year, the acronym lidar, standing for light detection and ranging, was first used by Middleton and Spilhaus in their book 'Meteorological Instrument'. Later, in the late 1950s, the term 'Remote Sensing' was coined by Evelyn Pruitt [62].

But the breakthrough in the development of the lidar instruments for atmospheric monitoring occurred with the invention of the laser [63] and of the Q-Switching technique [64]. Soon, Fiocco and Smulling used the new invention, first to obatin optical echoes from the Moon [65] then to detect scattering layers in the upper atmosphere [66, 67].
Then, in 1966, the first Raman measurement occurred [68, 69, 70]. Cooney also showed that using the Raman lidar it is possible to identify the fraction of the returning signal due to aerosol scatter only [71]. Finally, the first measurement of Raman scattering by water vapor was conducted by Melfi [72].

## 4.3 Basic lidar systems

The architecture of a lidar system can be divided into two main blocks (Figure 4.1):

- transmitter;
- receiver.

The transmitter includes a monochromatic and collimated light source capable of emitting short-duration light pulses to achieve sufficient vertical resolution. Typically, more than one wavelength is used, and the choice depends on the type of

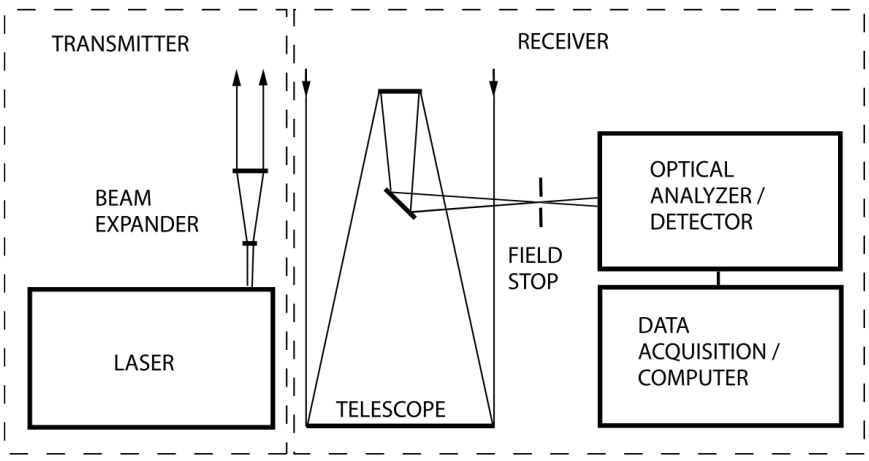


**Figure 4.1:** Basic lidar architecture from [55].

interaction with atmospheric constituents being studied. Nowadays, the most commonly used source in Raman lidar for aerosol studies is the Nd:YAG laser, which provides light radiation at 355 nm, 532 nm, and 1064 nm through the use of nonlinear optical systems. Along with the laser, the transmitter also includes beam splitters used to deflect laser beams and eliminate unwanted wavelengths (beam splitters reflect a specific wavelength at a precise angle of incidence and allow other wavelengths to pass through). Finally, there are beam expanders that reduce the divergence of the laser beam.

The so emitted light radiation interacts with atmospheric constituents, including molecules and aerosols, and the fraction of it that is backscattered is collected and analyzed by the receiver. This is composed by one or more telescopes, an optical system for selecting wavelengths of interest, and detectors which convert a light signal into an electrical signal. Because of the high dynamics of the returned signal (its amplitude varies on several orders of magnitude), these detectors must have a good linearity in response to incident light and they usually are photomultiplier tubes or avalanche photodiodes for IR wavelengths. The whole instrument is controlled by a computer dedicated to data acquisition and data analysis. The backscattered signal is recorded in function of time, and the interval between laser emission and signal detection provide the range (distance from the instrument) where backscattering occurred. The acquisition can be made using two main techniques: analog acquisition (A/D) and photon counting (PC). The former is more suitable for lower ranges where the photon counting rates are too high to avoid pile-up effects. The latter, instead, is used for larger ranges.

From a geometric perspective, there are two Lidar configurations. In the bistatic configuration, the transmitter and receiver are placed at a remarkable distance from each other, while in the monostatic configuration, the transmitter and receiver are in the same location. The first configuration allows for higher spatial resolution, while the second enables the investigation of lower atmospheric layers due to a shorter full overlap distance. Additionally, if in the monostatic configuration the optical axis of the telescope coincides with the axis of the laser beam, then the configuration is referred to as monoaxial.

## 4.4 Lidar equation

The equation that describes the acquired signal from a lidar system as a function of distance is called the lidar equation. In the following part of this paragraph, the lidar equation is elucidated based on the work of Wandinger [55].
The acquired signal can be written as

$$P(R) = KG(R)\beta(R)T(R), \tag{4.1}$$

where P(R) is the power received from a distance or range R, the factor K summarizes the performance of the lidar system, G(R) describes the range-dependent measurement geometry, $\beta$(R) is the backscatter coefficient and T(R) is the transmission. The first two terms are entirely determined by the instrumental setup, whereas the last two incorporate information about the atmosphere.
In greater detail, the system factor can be written as

$$K = P_0 \frac{c\tau}{2} A\eta. \tag{4.2}$$

$P_0$ is the power of a single laser pulse, $\tau$ its temporal length and c$\tau$ is the length of volume illuminated by laser at a given time t. The factor 1/2 is due to an apparent folding of the laser pulse caused by the backscatter process. Exactly, the volume edges from which the detected signal at time t comes back, are $R_1 = ct/2$ and $R_2 = c(t-\tau)/2$. So the effective pulse length is $\Delta R = R_1 - R_2 = c\tau/2$. The other terms included in Equation 4.2 are the area of the primary mirror (or lens, depending from the telescope) of the receiver $A$ and the overall system efficiency $\eta$.
The geometric factor

$$G(R) = \frac{O(R)}{R^2} \tag{4.3}$$

incorporates the overlap function $O(R)$, representing the intersection between the laser beam and the telescope field of view. It varies between 0, near the telescope where backscattered radiation is not seen by the receiver, and 1 where the overlap is complete. The factor $1/R^2$ is due to the fact that the telescope area makes up a part of a sphere's surface with radius $R$ that encloses the scattering volume and is also the main responsible for the high dynamic range of the lidar signal.
The backscatter coefficient $\beta(R, \lambda)$ quantifies the amount of light scattered in the backward direction and is the primary atmospheric parameter determining the strength of the lidar signal. If $N_j$ is the concentration of scattering particles of kind j, and $\mathrm{d}\sigma_{j,SCA}(\theta, \lambda)/\mathrm{d}\Omega$ is the differential scattering cross section, the backscatter coefficient can be written as

$$\beta(R, \lambda) = \sum_j N_j(R) \frac{d\sigma_{j,SCA}}{d\Omega}(\pi, \lambda) \tag{4.4}$$

where the sum is over all the scattering components. Within the atmosphere, scattering can occur from both molecules and particles, hence

$$\beta(R, \lambda) = \beta_{\mathrm{mol}}(R, \lambda) + \beta_{\mathrm{aer}}(R, \lambda). \tag{4.5}$$

The last factor of Eq. 4.1, the transmission, states the fraction of light lost on the

optical path, and for the elastic backscatter case, is given by

$$T(R) = T(R,\lambda)^2 = exp\left[-2\int_0^R \alpha(R',\lambda)dR'\right] \tag{4.6}$$

while for the inelastic case, in which photons are backscattered at a different wavelength $\lambda'$, by

$$T(R) = T(R,\lambda) \times T(R,\lambda') = exp\left[-\int_0^R \alpha(R',\lambda)dR'\right] \times exp\left[-\int_0^R \alpha(R',\lambda')dR'\right] \tag{4.7}$$

where $\alpha(R,\lambda)$ is the extinction coefficient and it is defined as

$$\alpha(R,\lambda) = \sum_j N_j(R)\sigma_{j,\text{ext}}(\lambda) \tag{4.8}$$

with $\sigma_{j,\text{ext}}$ the extinction cross section. Extinction can result from the scattering and absorption of light by molecules and particles alike. Therefore, $\alpha(R,\lambda)$ represents the cumulative effect of four distinct terms:

$$\alpha(R,\lambda) = \alpha_{\text{mol,sca}}(R,\lambda) + \alpha_{\text{mol,abs}}(R,\lambda) + \alpha_{\text{aer,sca}}(R,\lambda) + \alpha_{\text{aer,abs}}(R,\lambda) \tag{4.9}$$

To sum up, the lidar equations for both elastic and inelastic cases, can be written respectively as

$$P(R,\lambda) = P_0\frac{c\tau}{2}A\eta\frac{O(R)}{R^2}\beta(R,\lambda)T(R,\lambda)^2, \tag{4.10}$$

$$P(R,\lambda,\lambda') = P_0\frac{c\tau}{2}A\eta\frac{O(R)}{R^2}\beta(R,\lambda,\lambda')T(R,\lambda) \times T(R,\lambda') \tag{4.11}$$

with $\lambda$ the laser wavelength and $\lambda'$ the wavelength of the radiation backscattered inelastically. Thus $\beta(R,\lambda,\lambda')$ is the Raman backscatter coefficient for an incident wavelength $\lambda$ and a backscattered wavelength $\lambda'$.
In addition to the just described lidar signal, the detected signal will always include a background contribution $P_\text{b}$. The background is due to to scattered light, coming from sources other than the laser, within the telescope field of view.
In the figure below (4.2), two simulated lidar signals are displayed. The signals were obtained with a MATLAB program developed at the Department of Physical and Chemical Sciences of the University of L'Aquila and at CETEMPS (Center of Excellence Telesensing of Environment and Model Prediction of Severe events) by M. Iarlori. In this simulation there are aerosols in the planetary boundary layer, a dust layer at about 5 km, and a cirrus above 10 km.

## 4.5 Aerosol optical properties from lidar signals

Since an elastic backscatter lidar detects the total backscattered radiation without distinguishing between the contribution from molecules and that from aerosols, the inversion of the corresponding lidar equation requires assumptions about the relationship between the extinction and backscatter coefficients of aerosols (see Appendix A).
On the contrary, a Raman lidar detects at least two signals. A first elastic signal at

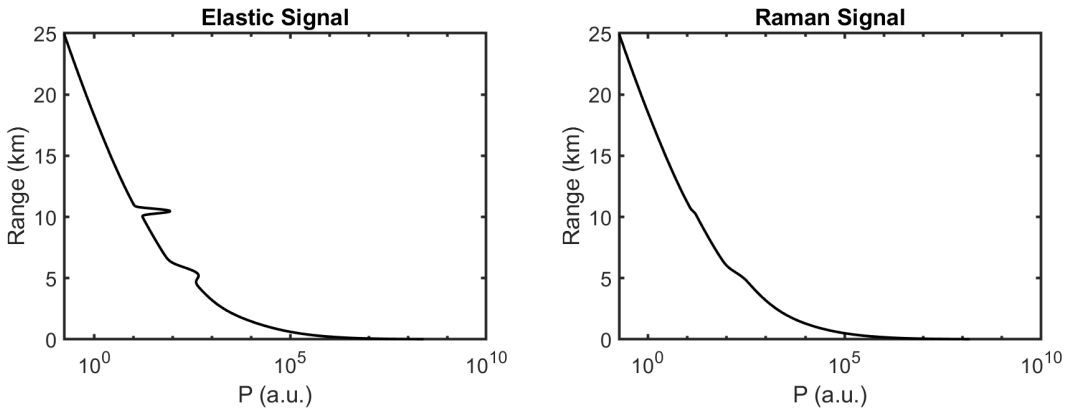


**Figure 4.2:** Simulated lidar signals. On the left panel the elestic signal at 355 nm and on the right the Raman signal at 386 nm.

the same wavelength of the laser beam and a second signal due to Raman scattering of a molecular species, whose concentration as a function of range can be known. Typically, the backscattered radiation from nitrogen molecules with a Raman shift of 2327 $cm^{-1}$ or oxygen molecules with a Raman shift of 1556 $cm^{-1}$ is detected.
Since the Raman signal depends only on aerosol extinction and not on aerosol backscatter, this allows for the determination of aerosol extinction coefficient without making assumptions, as in the elastic case [73, 74].

### 4.5.1 Aerosol extinction coefficient

The Raman lidar equation Eq. 4.11 can be rewritten as

$$P(R,\lambda_{\mathrm{L}},\lambda_{\mathrm{R}}) = \frac{BO(R)}{R^2}\beta(R,\lambda_{\mathrm{L}},\lambda_{\mathrm{R}}) \times exp\left\{-\int_0^R \left[\alpha(R',\lambda_{\mathrm{L}}) + \alpha(R',\lambda_{\mathrm{R}})\right] dR'\right\} \tag{4.12}$$

where all the range independent parameters have been included in the coefficient B. Being $\mathrm{N_R}$ the number density of the molecules which give the Raman backscattering, and $\mathrm{d}\sigma/\mathrm{d}\Omega$ the Raman differential cross section, the backscatter coefficient is

$$\beta(R,\lambda_{\mathrm{L}},\lambda_{\mathrm{R}}) = N_{\mathrm{R}}(R)\frac{d\sigma(\lambda_{\mathrm{L}},\lambda_{\mathrm{R}},\pi)}{d\Omega} \tag{4.13}$$

The profile of both nitrogen and oxygen can be used since their number densities are well known.
From Eqs. 4.12 and 4.13 follows that

$$\alpha(R,\lambda_{\mathrm{L}}) + \alpha(R,\lambda_{\mathrm{R}}) = \frac{d}{dR}\left[\ln\frac{O(R)N_{\mathrm{R}}(R)}{R^2P(R)}\right] \tag{4.14}$$

with $P(R) \equiv P(R,\lambda_{\mathrm{L}},\lambda_{\mathrm{R}})$. With the complete overlap condition and separating the individual contributions to extinction, we have

$$\alpha_{\mathrm{aer}}(R,\lambda_{\mathrm{L}}) + \alpha_{\mathrm{aer}}(R,\lambda_{\mathrm{R}}) = \frac{d}{dR}\left[\ln\frac{N_{\mathrm{R}}(R)}{R^2P(R)}\right] - \alpha_{\mathrm{mol}}(R,\lambda_{\mathrm{L}}) - \alpha_{\mathrm{mol}}(R,\lambda_{\mathrm{R}}) \tag{4.15}$$

and finally, assuming a wavelength dependence of the aerosol extinction such as

$$\frac{\alpha_{\mathrm{aer}}(\lambda_{\mathrm{L}})}{\alpha_{\mathrm{aer}}(\lambda_{\mathrm{R}})} = \left(\frac{\lambda_{\mathrm{R}}}{\lambda_{\mathrm{L}}}\right)^k \tag{4.16}$$

we get the extinction coefficient profile as

$$\alpha_{\text{aer}}(R,\lambda_{\text{L}}) = \frac{\frac{d}{dR}\left[\ln\frac{N_{\text{R}}(R)}{R^2P(R)}\right] - \alpha_{\text{mol}}(R,\lambda_{\text{L}}) - \alpha_{\text{mol}}(R,\lambda_{\text{R}})}{1+\left(\frac{\lambda_{\text{L}}}{\lambda_{\text{R}}}\right)^{k}} \tag{4.17}$$

The exponent $k$ is called the Ångstrom exponent and a suitable value for our measurements is roughly $k = 1$. Its value can also be estimated using other instruments, such as a sun photometer, and in general, it is range dependent. The effects of the choice of the Ångstrom exponent are shown in Figure 4.3. The introduced systematic error is generally small compared to other sources of error.

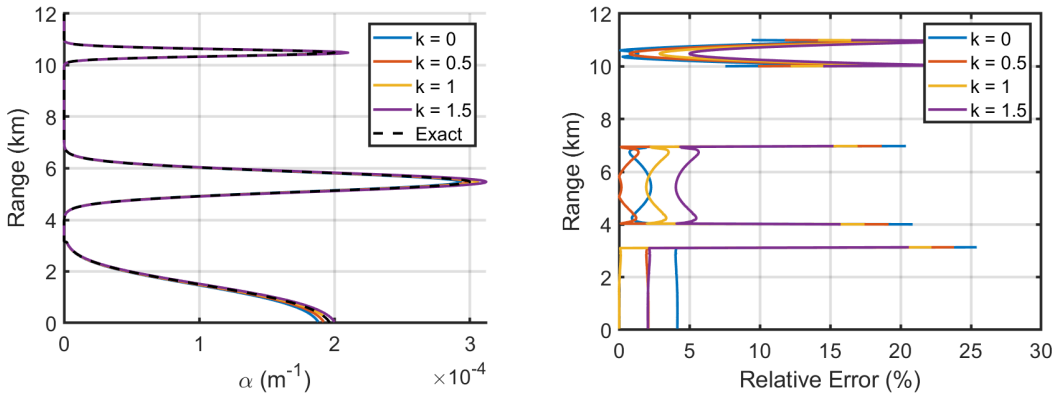


**Figure 4.3:** Effects of the choice of the Ångstrom exponent on the retrieval of the aerosol extinction coefficient from simulated lidar signals of Figure 4.2.

The values of the molecular concentration and of $N_{\text{R}}(R)$ are determined from vertical profiles of temperature and pressure measured by radiosonde (if available), or from a standard atmosphere model. Then $\alpha_{\text{mol}}(R,\lambda_{\text{L,R}})$ can be computed with the Rayleigh theory [75]. Details on the calculations can be found in [76, 77].
The integral of the aerosol extinction coefficient is referred to as the aerosol optical depth and is given by

$$\tau_{\text{aer}}(R,\lambda_{\text{L}}) = \int_0^R \alpha_{\text{aer}}(R',\lambda_{\text{L}})dR'. \tag{4.18}$$

### 4.5.2 Aerosol backscatter coefficient

The aerosol backscatter coefficient can be derived from both elastic and Raman signals. This is accomplished by computing the ratio

$$\frac{P(R,\lambda_{\text{L}})P(R_0,\lambda_{\text{R}})}{P(R_0,\lambda_{\text{L}})P(R,\lambda_{\text{R}})}$$

where, as usual, $\lambda_{\text{L}}$ and $\lambda_{\text{R}}$ are respectively the laser wavelength and the inelastically backscattered radiation wavelength and $R_0$ is a reference height. Using the respective

lidar equations (Eqs. 4.10 and 4.11), we can write

$$\begin{aligned}\beta_{\mathrm{aer}}(R,\lambda_{\mathrm{L}}) &= -\beta_{\mathrm{mol}}(R,\lambda_{\mathrm{L}}) + [\beta_{\mathrm{aer}}(R_0,\lambda_{\mathrm{L}}) + \beta_{\mathrm{mol}}(R_0,\lambda_{\mathrm{L}})] \\ &\times \frac{P(R_0,\lambda_{\mathrm{R}})P(R_0,\lambda_{\mathrm{L}})N_{\mathrm{R}}(R)}{P(R,\lambda_{\mathrm{R}})P(R,\lambda_{\mathrm{L}})N_{\mathrm{R}}(R_0)} \\ &\times \frac{exp\left\{-\int_{R_0}^{R}\left[\alpha_{\mathrm{aer}}(R',\lambda_{\mathrm{R}}) + \alpha_{\mathrm{mol}}(R',\lambda_{\mathrm{R}})\right]dR'\right\}}{exp\left\{-\int_{R_0}^{R}\left[\alpha_{\mathrm{aer}}(R',\lambda_{\mathrm{L}}) + \alpha_{\mathrm{mol}}(R',\lambda_{\mathrm{L}})\right]dR'\right\}}.\end{aligned}$$

The reference height is usually chosen such that $\beta_{\mathrm{mol}}(R_0,\lambda_{\mathrm{L}}) \gg \beta_{\mathrm{aer}}(R_0,\lambda_{\mathrm{L}})$ so that $\beta_{\mathrm{mol}}(R_0,\lambda_{\mathrm{L}}) + \beta_{\mathrm{aer}}(R_0,\lambda_{\mathrm{L}}) \approx \beta_{\mathrm{mol}}(R_0,\lambda_{\mathrm{L}})$. These conditions are typically met in the upper troposphere. Consequently, the expression for the backscatter coefficient can be reformulated as

$$\beta_{\mathrm{aer}}(R,\lambda_{\mathrm{L}}) = -\beta_{\mathrm{mol}}(R,\lambda_{\mathrm{L}}) + C \times \frac{P(R,\lambda_{\mathrm{L}})}{P(R,\lambda_{\mathrm{R}})}N_{\mathrm{R}}(R) \times \frac{T(R,\lambda_{\mathrm{R}})}{T(R,\lambda_{\mathrm{L}})}, \tag{4.19}$$

where the calibration constant $C$ includes all the terms determined at the reference height $R_0$ and is given by

$$C = \frac{\beta_{\mathrm{mol}}(R_0,\lambda_{\mathrm{L}})P(R_0,\lambda_{\mathrm{R}})}{P(R_0,\lambda_{\mathrm{L}})N_{\mathrm{R}}(R_0)} \times \frac{T(R_0,\lambda_{\mathrm{L}})}{T(R_0,\lambda_{\mathrm{R}})}. \tag{4.20}$$

### 4.5.3 Lidar Ratio

The lidar ratio is then computed as

$$LR_{\mathrm{aer}}(R,\lambda_{\mathrm{L}}) = \frac{\alpha_{\mathrm{aer}}(R,\lambda_{\mathrm{L}})}{\beta_{\mathrm{aer}}(R,\lambda_{\mathrm{L}})}. \tag{4.21}$$

Its value depends on size, shape and spatial orientation of the scattering particles and thus contains information regarding their microphysical properties [52]. The lidar ratio thus helps to identify the type of aerosol.

## 4.6 Water vapor

Although in principle this technique can be applied to any Raman-active gas, it is, in fact, used only for the most abundant species. This is due to the small values of the Raman cross-sections if compared to Rayleigh cross-sections.
Through the use of a Raman lidar, the water vapor mixing ratio is derived by measuring the ratio of water-vapor-to-reference signals, where nitrogen serves as the reference gas [78, 79]. The wavelengths $\lambda_{\mathrm{R}_1}$ and $\lambda_{\mathrm{R}_2}$ correspond to the inelastically backscattered radiation by nitrogen (Raman shift of $2327\,\mathrm{cm}^{-1}$) and water vapor (Raman shift of $3652\,\mathrm{cm}^{-1}$), respectively. Inserting the corresponding Raman lidar equations, the mixing ratio is given by

$$m(R) = K_m \frac{P_{\mathrm{H_2O}}(R,\lambda_{\mathrm{R}_2})}{P_{\mathrm{N_2}}(R,\lambda_{\mathrm{R}_1})} \times \frac{exp\left\{-\int_0^R\left[\alpha_{\mathrm{aer}}(R',\lambda_{\mathrm{R}_1}) + \alpha_{\mathrm{mol}}(R',\lambda_{\mathrm{R}_1})\right]dR'\right\}}{exp\left\{-\int_0^R\left[\alpha_{\mathrm{aer}}(R',\lambda_{\mathrm{R}_2}) + \alpha_{\mathrm{mol}}(R',\lambda_{\mathrm{R}_2})\right]dR'\right\}}, \tag{4.22}$$

where the molecular extinction is obtained using the Rayleigh theory of scattering, and the aerosol extinction coefficient is derived from the nitrogen Raman signal. This latter value is affected by the overlap function and it might be preferable to use the aerosol backscatter coefficient multiplied by a constant lidar ratio [80].
The system constant $K_m$ can be theoretically determined by knowing the Raman cross-sections and the overall system efficiencies in function of wavelength. However, since this quantities are not well known and the calibration accuracy is usually not better than 10% [81], it is preferred to obtain $K_m$ by comparing the water vapor mixing ratio with that measured by another technique.

The most commonly used method is the normalization to radiosonde measurements [82]. This calibration technique may suffer from nonsimultaneity and noncolocation of the lidar and the radiosonde. As a consequence, it is preferable to use multiple radiosondes for each Lidar observation, thus increasing costs.
During a measurement campaign it could be necessary to compute the calibration constant several times, and doing so using radiosondes can prove to be costly.

To take into account the instrument stability, it is possible to use a calibrated lamp [82]. Since the water vapor mixing ratio is obtained from the ratio of the water vapor Raman signal and the nitrogen Raman signal, the relative efficiency of the two Raman channels can be checked by the ratio of the two signals acquired using a lamp as the only light source which directly illuminates the primary mirror. The use of a calibrated lamp then allows the use of a hybrid calibration technique, which does not require absolute calibration using radiosondes for each observational campaign.
Let's consider three observational campaigns. In the first campaign, by using radiosondes, we can relate the Raman signals ratio $P_1$ to the transmission ratio of the two channels $T_1$ and the water vapor mixing ratio $m_1$:

$$P_1 = T_1 m_1.$$

Then, the ratio of the two signals acquired with the lamp, $P_1'$, is calculated, and we can compute the factor $L$ defined as

$$L_1 = \frac{P_1'}{T_1}.$$

As a consequence, the water vapor mixing ratio can then be written as

$$m_1 = L_1 \frac{P_1}{P_1'}.$$

In the second campaign, radiosondes are not used, only the lamp is utilized. The mixing ratio is given by $m_2 = L_1 P_2 / P_2'$. Finally, in the third campaign, we proceed as in the first one. If the value of L didn't change no action is required. Otherwise, if L drifted, in the second campaign, a linear combination of L1 and L3 should be used, and the mixing ratio should be recalculated afterwards with the new value of L.

An alternative method is the comparison with a co-located photometer [83]. Since sun photometer provides the column water vapor content, the same quantity must be computed with lidar measurements in order to perform the system calibration. Moreover, nowadays, there are sun-sky-moon photometers that can operate

even during the night. This method allows for the continuous calibration of water vapor lidar observations.
The precipitable water content retrieved with the Raman lidar is computed as [83]

$$PWV(K_m) = \int_{R_0}^{R_1} \rho_{\mathrm{H_2O}}(R, K_m) dR, \tag{4.23}$$

where $\rho_{\mathrm{H_2O}}(R, K_m)$ is the water vapor concentration and it is given by

$$\rho_{\mathrm{H_2O}}(R, K_m) = m(R, K_m)\rho_{\mathrm{air}}(R). \tag{4.24}$$

The air density $\rho_{\mathrm{air}}(R)$ can be computed as

$$\rho_{\mathrm{air}}(R) = 348.328 \frac{p(R)}{T(r)} \left[ p(R) \left( 57.9 \times 10^{-8} - \frac{0.94581 \times 10^{-3}}{T(R)} + \frac{0.25844}{T^2(R)} \right) \right] \tag{4.25}$$

with the vertical profiles of pressure $p(R)$ (in hectopascal) and temperature $T(z)$ (in Kelvin) taken from GDAS. In order to obtain the calibration constant $K_m$, $PWM(K_m)$ is compared with the precipitable water vapor retrieved with a sun photometer ($PWV_{\mathrm{SP}}$), satisfying the following relation:

$$\frac{PWV_{\mathrm{SP}}}{PWV(K_m)} = 1. \tag{4.26}$$

The combination of water vapor mixing ratios and GDAS temperature profiles facilitates the derivation of relative humidity profiles with a relative uncertainty ranging from 10 % to 20 % [83].

Another possibility for calibrating lidar observations is to use the integrated water vapor obtained from a co-located microwave radiometer (MWR). This method provides a calibration constant very stable with a relative uncertainty of 5 % [80]. However, it should be noted for the calibration methods that use integrated water quantities, that lidar observations do not start from the ground but from a minimum range of few tens or hundreds meters. Below this range, information needs to be extrapolated.

## 4.7 Data analysis

### 4.7.1 Signal noise

An actual lidar signal, is susceptible to noise, which has the potential to diminish the precision of a measurement or completely obscure the physical signal. Noise can have optical or thermal origin. The main kind of noise affecting lidar signals are [12]:

- noise in signal (quantum noise);
- dark-current noise;
- thermal noise;
- background noise.

The first three terms represent different forms of shot noise. The last term instead depends on the environment and can be determined in the far range of the lidar signal or in the pre-trigger range before the laser pulse, where no backscatter signal is expected.
We are primarily interested in signal characteristics characterized by low-frequency structures, while noise exhibits high frequencies. Typically, to enhance the signal-to-noise ratio, a considerable number of lidar signals are averaged. Subsequently, noise reduction can be achieved through the application of a low-pass filter, a process known as smoothing. However, this smoothing procedure also results in a reduction of vertical resolution. Conversely, for the retrieval of aerosol extinction coefficients, a numerical derivative is required, which accentuates high frequencies. To address this, the numerical derivative is often coupled with a smoothing filter. As outlined in [84], discrepancies may arise if data are not compared at the same resolution, as exemplified in the calculation of the lidar ratio (Eq. 4.21).
Hence, to obtain the lidar ratio profile, the aerosol extinction coefficient is determined by evaluating the smoothed first derivative of $N_{\mathrm{R}}(R)/R^2 P_{\mathrm{R}}(R)$. Subsequently, the same low-pass filter embedded in the numerical derivative is applied to smooth the backscatter coefficient.
With a more detailed approach, a digital filter with a finite impulse response (FIR) $h(k)$ which transforms a sequence of numbers $x(n)$ in $y(n)$, can be written as

$$y(n) = \sum_{k=-N}^{N} h(k)x(n-k), n = N, \ldots, n_{\max} - N - 1. \tag{4.27}$$

The frequency response is given by the Fourier transformation of $h(k)$

$$H(\omega) = \sum_{k=-N}^{N} h(k)e^{-j\omega k}. \tag{4.28}$$

For the ideal first derivative the frequency response is $H^{(1)}(\omega) = j\omega$ and grows with $\omega$ amplifying the noise present in the lidar signal. The first derivative is thus used in cascade with a low pass filter:

$$H^{(1)\mathrm{L}}(\omega) = H^{(1)}(\omega)H^{\mathrm{L}}(\omega), \tag{4.29}$$

where $H^{\mathrm{L}}(\omega)$ is the frequency response of the low pass filter that must be used for smoothing the backscatter coefficient.
The frequency response of the smoothed first derivative is given by

$$H^{(1)\mathrm{L}}(\omega) = -j \sum_{k=-N}^{N} h^{(1)\mathrm{L}}(k) \sin \omega k, \tag{4.30}$$

and the frequency response of the embedded low pass filter is

$$H^{\mathrm{L}}(\omega) = \frac{H^{(1)\mathrm{L}}(\omega)}{H^{(1)}(\omega)} = \frac{-\sum_{k=-N}^{N} h^{(1)\mathrm{L}}(k) \sin \omega k}{\omega}. \tag{4.31}$$

This is the low pass filter that should be used to smooth the backscatter coefficient.

### 4.7.2 Photon-Counting nonlinear response

Another important consideration is that a real signal acquired in photon counting mode needs to be corrected for detector dead time before any further processing. As outlined in [85], dead time refers to the shortest interval between two events necessary for them to be detected as distinct pulses. It is determined by both the detector and its associated electronics. Two prevalent models are typically encountered (see Figure 4.4). In a paralyzable detector, an event during the dead time prolongs the dead time interval, whereas in a nonparalyzable detector, this does not occur. If $m$ is the recorded count rate, $n$ the true rate and $\tau$ the system dead time, the rate of losses for a nonparalyzable system is

$$n - m = nm\tau,$$

and thus

$$n = \frac{m}{1 - m\tau.} \tag{4.32}$$

For a paralyzable system the dead periods do not have a fixed length. The measured rate $m$ is given by that events with time intervals between true events greater than $\tau$. The probability to have a time interval between $T$ and $T + dT$ is given by

$$P_1(T)dT = ne^{-nT}dT,$$

and the probabilty to have time intervals greater than $\tau$ is

$$P_2(\tau) = \int_\tau^\infty P_1(T)dT = e^{-n\tau},$$

so the relation between the true rate and the counted rate is

$$m = ne^{-n\tau}. \tag{4.33}$$

As reported in [86], since both $m$ and $n$ must be greater than zero, Eq. 4.32 can be solved only if

$$m < \frac{1}{\tau}, \tag{4.34}$$

while inversion of Eq. 4.33 requires

$$m < \frac{1}{e\tau}. \tag{4.35}$$

### 4.7.3 Error analysis

Every physical measurement is affected by an error, and comes with an associated uncertainty. A measurement without its uncertainty might lack any meaningful significance.
An error has two components, a statistical or random component which arises from stochastic variations of influence quantities, and a systematic error which arises from a systematic effect. If a systematic effect is not recognized it won't contribute to the uncertainty of the result of a measurement but it will contribute to its error.

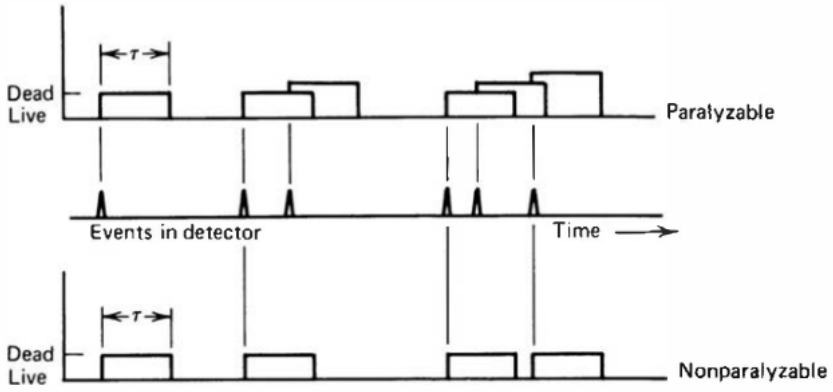


**Figure 4.4:** Paralyzable and nonparalyzable models. From [85].

A comprehensive commentary on systematic uncertainties in the context of lidar measurements can be found in [74].

In a lidar measurements, the statistical error arises due to signal or photon noise. In the case of photon counting, it is assessed using error propagation and Poisson statistics. In other words, it is assumed that the uncertainty of the total number of photon events is equivalent to the square root of the total photons counted.
On the other hand, systematic errors stem from the estimation of temperature and pressure profiles, the estimation of ozone profiles, the wavelength dependence of the Ångstrom exponent, and the omission of multiple scattering. Other sources of systematic error are the zero bin range (see Section 6.4) and the choice of the reference range for the backscatter coefficient computation. Furthermore, if the aerosol scattering properties vary significantly, it is essential to exercise great care when averaging the lidar signals [74]. All these effects must be considered in the estimation of the uncertainty of the final result and this is usually done through numerical simulation.

The main contribution to the uncertainty arises from the photon noise. To reduce this contribution, lidar signals must be smoothed. Temperature and pressure profiles are used for the computation of the Rayleigh extinction and are usually obtained from a standard atmosphere model. In absence of strong inversion layers, the effect of temperature uncertainty is small [74]. The effects of ozone absorption can instead be neglected for the laser wavelengths used, and the effects of multiple scattering dependes on the aerosol load [87]. The choice of the Ångstrom exponent can contribute to the overall uncertainty for a few percent (Figure 4.3). The effects of the zero bin range can instead be large and thus it must be checked periodically. It mainly affects the lower ranges (below 1 km) in the aerosol extinction coefficient retrieval. Also the effects of the choice of the reference range in the computation of $\beta_{\text{aer}}$ can be minimized using statistical tests for its determination [88].

Finally, also the used retrieval algorithm can introduce an error and contributes to the uncertainty of the final result. In particular time averaging, smoothing, first derivative and more in general signal filtering must be considered in the estimation of the uncertainty.

The uncertainties of lidar products can be determined in two ways, which are illustrated below: through the standard error propagation [89] and using Monte Carlo methods [86, 90].

**Standard error propagation**

If we have $N$ different measurements of a quantity $x$, the best estimation is given by the arithmetic average:

$$\bar{x} = \frac{1}{N}\sum_{i=1}^{N} x_i,$$

while the best estimation of uncertainty is given by standard deviation:

$$\sigma_x = \sqrt{\frac{1}{N-1}\sum_{i=1}^{N}(x_i - \bar{x})^2}.$$

In general for a function $f(x, y, \dots)$ derived from measured variables $x$,$y$,..., the uncertainty can be calculated as

$$\delta f^2 = \delta x^2 \left(\frac{\partial f}{\partial x}\right)^2 + \delta y^2 \left(\frac{\partial f}{\partial y}\right)^2 + \dots, \tag{4.36}$$

where $\delta x$,$\delta t$,..., are the uncertainties of the corresponding variables, and are uncorrelated.
In the photon counting mode, since for a poissonian distribution the standard deviation $\sigma = \sqrt{\mu}$ where $\mu$ is the expected mean value, the signal uncertainty after the background subtraction is given by

$$\delta N = \sqrt{N_\mathrm{S} + N_\mathrm{B}}, \tag{4.37}$$

where

$$N_\mathrm{B} = \frac{1}{n}\sum_{i=k}^{k+n} N_i, \tag{4.38}$$

is the background calculated over $n$ bins. For the analog acquisition the signal uncertainty, after the average of several acquisitions, is instead given by

$$\delta N = \sqrt{\delta_\mathrm{S}^2 + \delta_\mathrm{B}^2}, \tag{4.39}$$

where $\delta_S$ and $\delta_B$ are the standard deviations of the signals averaged.
If after the average of several signals, data binning is applied to the signal, then

$$\delta S = \frac{1}{b}\sqrt{\sum_{i=1}^{b}\sigma_i^2}, \tag{4.40}$$

where $b$ is the number of bins and $\sigma_i$ the standard deviations.
For a generic digital filter with a impulse response $h(k)$ with a finite number of non-zero elements described by Eq. 4.27, the error propagation gives

$$\delta y(n) = \sqrt{\sum_{k=-N}^{N} h(k)^2 \delta x(n-k)^2}, n = N, \dots, n_\mathrm{max} - N - 1, \tag{4.41}$$

with $n_\mathrm{max} \geq 2N+1$. If smoothing is employed during the data analysis, this formula can be used.

If molecular uncertainties are negligible, considering essentially only statistical uncertainty, it is possible using Eq. 4.36 to estimate the uncertainties associated to the retrieved lidar products.
For the aerosol extinction coefficient, using the Raman technique, the uncertainty is given by

$$\delta\alpha_{\mathrm{aer}}(R,\lambda_{\mathrm{L}}) = \left| \frac{\frac{d}{dR}\left(-\frac{\delta P(R)}{P(R)}\right)}{1+\left(\frac{\lambda_{\mathrm{L}}}{\lambda_{\mathrm{R}}}\right)^{k}} \right|. \tag{4.42}$$

For the aerosol backscatter coefficient we have

$$\frac{\delta\beta_{\mathrm{aer}}(R,\lambda_{\mathrm{L}})}{\beta_{\mathrm{aer}}(R,\lambda_{\mathrm{L}})} = \sqrt{\delta^2_{\mathrm{Raman}}(R)+\delta^2_{\mathrm{Elastic}}(R)}, \tag{4.43}$$

where

$$\delta^2_{\mathrm{Raman}}(R) = \left(\frac{\delta T_{\mathrm{aer}}(R,\lambda_{\mathrm{R}})}{T_{\mathrm{aer}}(R,\lambda_{\mathrm{R}})}\right)^2 + \left(\frac{\delta P(R,\lambda_{\mathrm{R}})}{P(R,\lambda_{\mathrm{R}})}\right)^2, \tag{4.44}$$

$$\delta^2_{\mathrm{Elastic}}(R) = \left(\frac{\delta T_{\mathrm{aer}}(R,\lambda_{\mathrm{L}})}{T_{\mathrm{aer}}(R,\lambda_{\mathrm{L}})}\right)^2 + \left(\frac{\delta P(R,\lambda_{\mathrm{L}})}{P(R,\lambda_{\mathrm{L}})}\right)^2, \tag{4.45}$$

and

$$\frac{\delta T_{\mathrm{aer}}(R,\lambda)}{T_{\mathrm{aer}}(R,\lambda)} = \int_0^R \delta\alpha_{\mathrm{aer}}(R',\lambda)dR'. \tag{4.46}$$

The lidar ratio uncertainty is

$$\frac{\delta LR_{\mathrm{aer}}(R,\lambda_{\mathrm{L}})}{LR_{\mathrm{aer}}(R,\lambda_{\mathrm{L}})} = \sqrt{\left(\frac{\delta\alpha_{\mathrm{aer}}(R,\lambda_{\mathrm{L}})}{\alpha_{\mathrm{aer}}(R,\lambda_{\mathrm{L}})}\right)^2 + \left(\frac{\delta\beta_{\mathrm{aer}}(R,\lambda_{\mathrm{L}})}{\beta_{\mathrm{aer}}(R,\lambda_{\mathrm{L}})}\right)^2}. \tag{4.47}$$

Finally, the uncertainty associated to water vapor mixing ratio is

$$\begin{aligned}\frac{\delta m(R)}{m(R)} = \Bigg\{ &\left(\frac{\delta P_{\mathrm{N_2}}(R,\lambda_{\mathrm{R_1}})}{P_{\mathrm{N_2}}(R,\lambda_{\mathrm{R_1}})}\right)^2 + \left(\frac{\delta P_{\mathrm{H_2O}}(R,\lambda_{\mathrm{R_2}})}{P_{\mathrm{H_2O}}(R,\lambda_{\mathrm{R_2}})}\right)^2 + \\ &+ \left(\frac{\delta T^{\mathrm{N_2}}_{\mathrm{aer}}(R,\lambda_{\mathrm{R_1}})}{T^{\mathrm{N_2}}_{\mathrm{aer}}(R,\lambda_{\mathrm{R_1}})}\right)^2 + \left(\frac{\delta T^{\mathrm{H_2O}}_{\mathrm{aer}}(R,\lambda_{\mathrm{R_2}})}{T^{\mathrm{H_2O}}_{\mathrm{aer}}(R,\lambda_{\mathrm{R_2}})}\right)^2 \Bigg\}^{\frac{1}{2}}\end{aligned} \tag{4.48}$$

**Montecarlo method**

Sometimes, employing the standard error propagation theory is either not feasible or too complex. This typically occurs when interpolation or smoothing routines are applied to handle lidar signals. In such instances, an alternative method to estimate the statistical uncertainties, based on Monte Carlo simulation, can be employed [86, 90].
If $s_i$ represents a lidar profile, $\Delta s_i$ the corresponding uncertainty and $F$ a generic operator which is applied to $s_i$ to obtain $S_i = F(s_i)$, this method allows the computation of the associated uncertainty $\Delta S_i$. The basic assumptions is that $s_i$ is a mean value with an uncertainty $\Delta s_i$ according to a statistical distribution. The initial step involves generating a synthetic lidar signal $s'_i$ following the assumed probability distribution. Gaussian statistics govern analog signals, while photon-counting signals adhere to Poissonian statistics. Next, the same operator $F$ is applied to the

synthetic signal, yielding $S'_i = F(s'_i)$.
By repeating this process a statistically significant number of times, the uncertainty profile $\Delta S_i$ can be estimated by calculating the standard deviation of the $S'_i$. Typically, around thirty variations of $S'_i$ suffice for this purpose.
The statistical uncertainty for a photon-counting signal can be estimated, as seen before, as the square root of the corresponding count. Instead, for analog signals, the corresponding statistical uncertainty time series are provided with signals, or, if they are not available, the uncertainty is estimated after time averaging of several signals by standard deviation. In all the operations done before the time average, the uncertainties of analog signals are not propagated.
In [90] the two methods for error propagation are compared, and they yield compatible results.

### 4.7.4 Workflow

To conclude the chapter, the following is the sequence of operations adopted to obtain the lidar products starting from photon counting signals:

1. dead time correction;
2. background removal;
3. trigger-delay correction;
4. time integration;
5. vertical binning;
6. aerosol extinction computation (with automatic smoothing);
7. aerosol backscatter computation;
8. lidar ratio computation.

# Chapter 5

# The Pierre Auger Raman lidar

## 5.1 Introduction

At the Pierre Auger Observatory for Ultra-High Energy Cosmic Rays (UHECRs), a Raman lidar is employed for aerosol monitoring, continuously collecting data since September 2013. While not directly utilized for correcting atmospheric shower parameters, lidar measurements are of fundamental importance for climatological studies of aerosols and serve as a cross-reference to determine the night with the least aerosol load (used in the data-normalised method for aerosol analysis [47]).
This chapter describes the instrument developed by DSFC/Univaq and presents the results of the lidar signal analysis conducted from 2014 to 2022. The findings presented here were presented by me at the collaboration meeting of the Pierre Auger Collaboration held in Brussels from June 4 to June 9, 2023.

## 5.2 Experimental Setup

The Auger Raman Lidar is located at the central laser facility (CLF). The system is autonomous and performs acquisitions before, during and after the FD shift without affecting the FD duty cycle (only four fluorescence telescopes are affected by lidar operations for about twenty minutes each night) [91]. Each acquisition last twelve minutes. The telescope is placed below an UV transmitting window (Figure 5.1) and a motorized roof, the opening of which is controlled by weather sensors.
The lidar has three channels: an elastic channel at 354.7 nm (Rayleigh-Mie scattering) and two Raman channels at 386.7 nm (molecular nitrogen Raman scattering), and at 407.6 nm (water vapor Raman scattering). The laser wavelength is at the center of the nitrogen fluorescence spectrum.
The receiver is composed by a parabolic mirror with a diameter of 50 cm and a focal length of 150 cm. A fiber optic guide transports the collected photons towards the detector box (Figures 5.2 and 5.3). Here the signal is splitted into the three channel wavelengths using beam splitters, interference and notch filters. Field lenses are also used to collimate the beam. Light is then converted into an electrical signal with three photomultiplier tubes and recorded with an FPGA card. Acquisition is performed in both photon counting mode and analog mode. The complete technical specifications can be found in Appendix D.

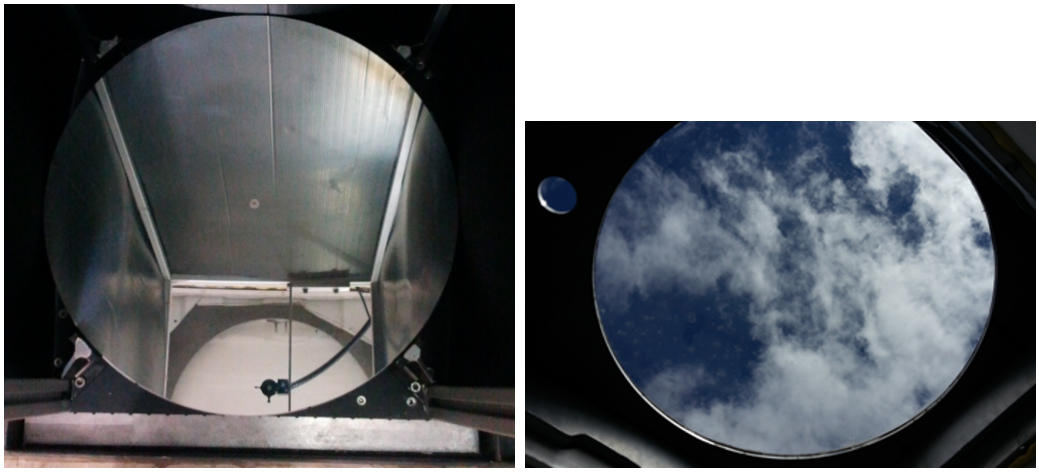

**Figure 5.1:** On the left the Auger Raman lidar primary mirror. On the right the UV transmitting silicon window.

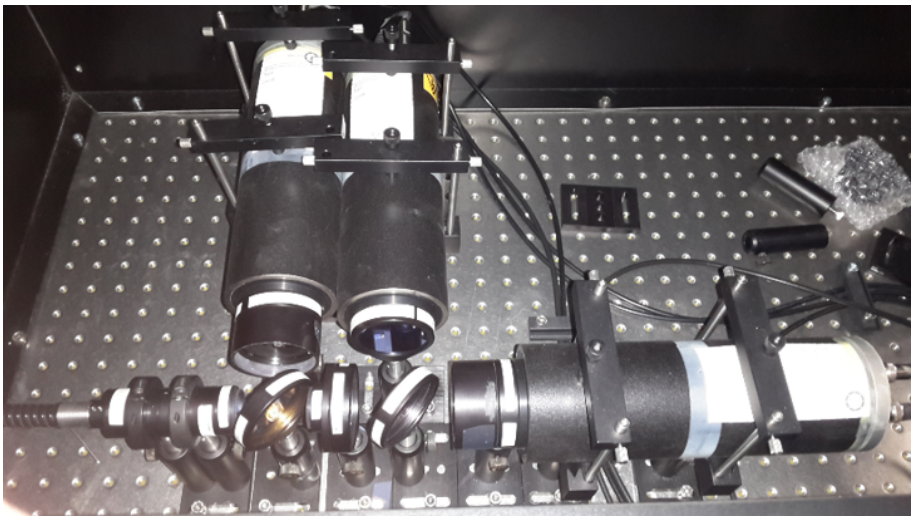

**Figure 5.2:** Detector box with optics for wavelength separation and photomultiplier tubes.

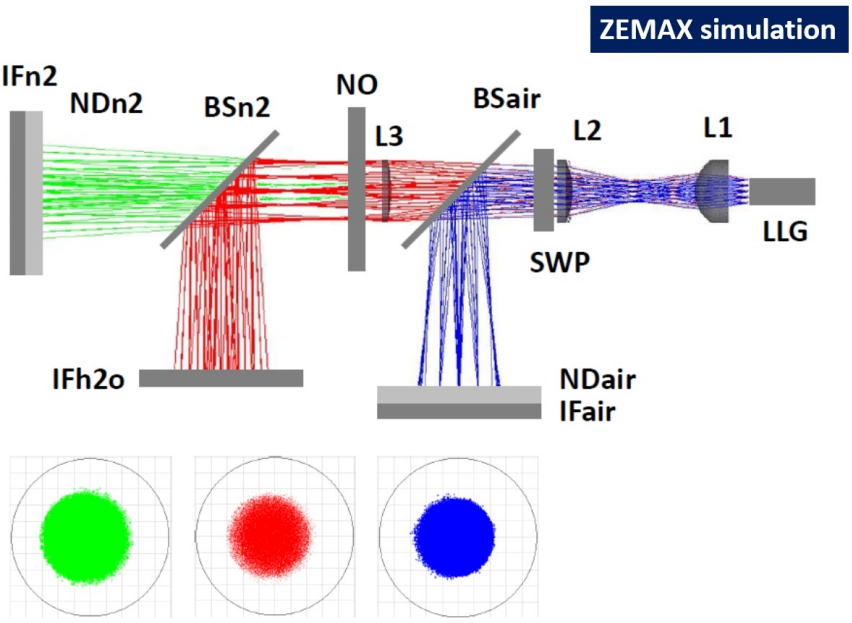


**Figure 5.3:** Detector box simulated with Zemax (same configuration as described in [92]). The meanings of the acronyms are: LLG liquid light guiding; L1, L2, L3 collimator lenses; SWP short wavelength pass filter; BSair and BSn2 beam splitters; NO notch filter; IFair, IFn2, and IFh2o interference filters; NDair and NDn2 neutral density filters. Details on the components are in Appendix D.

## 5.3 Aerosol optical properties at the Pierre Auger Observatory

The Auger Raman lidar can provide measurements of the vertical aerosol optical depth, the aerosol backscatter coefficient and the water vapor mixing ratio. In addition to these quantities, the aerosol extinction coefficient and the lidar ratio can also be computed.

To study the average atmospheric conditions during what are referred to as clear nights, profiles without the presence of clouds and high aerosol content have been selected. Starting from 5433 observations, distributed over time as shown in Figure 5.4, 675 observations have passed the selection criteria, and their distribution is shown in Figure 5.5. In 2019 the number of selected observations was drastically low. This year corresponds to a "bad period" in which the lidar performances were not optimal [93] because of optics disalignment. In the last years, on the other hand, the single board computer that manages the automatic operation of the lidar has started to show malfunctions. The number of these malfunctions are distributed as shown in Figure 5.6 and has increased over the years.

Before inverting, lidar signals are preprocessed. PC signals are corrected for the dead time, background and dark signals are subtracted, bin-shift is performed, and finally PC and AD signals are combined together.

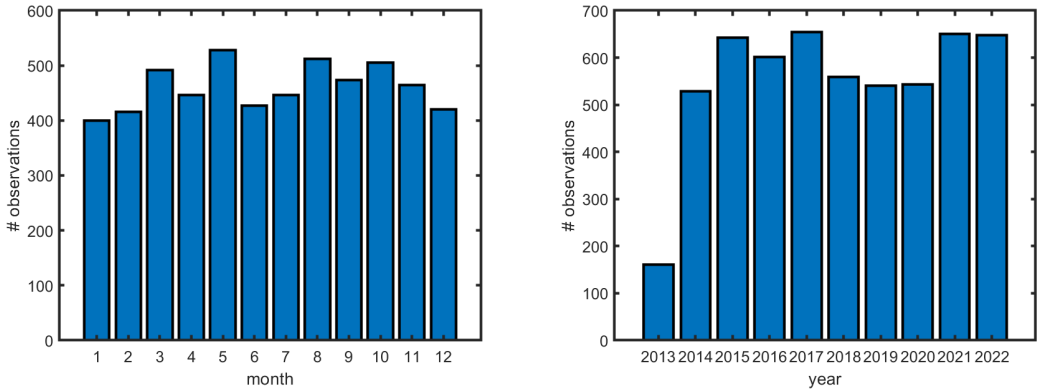


**Figure 5.4:** Distributions of the total number of observations, before filtering, over the months (left panel) and over the years (right panel).

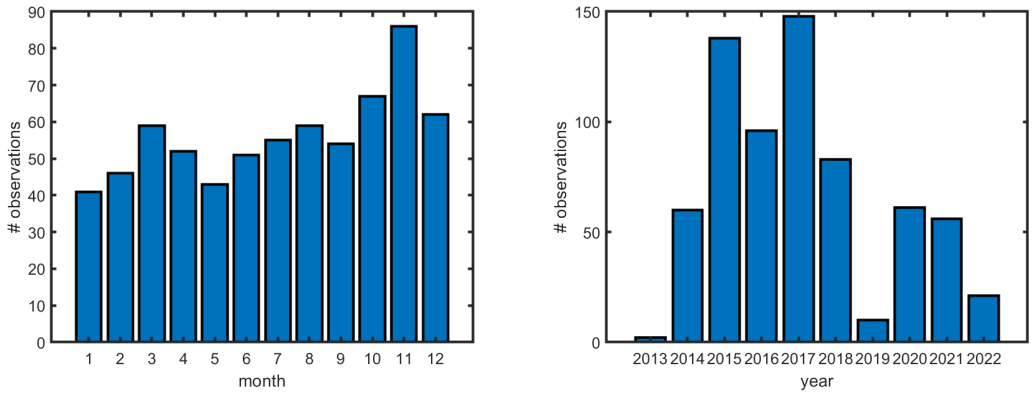


**Figure 5.5:** Observations distributions over time. On the left the distribution over the months, on the right over the years.

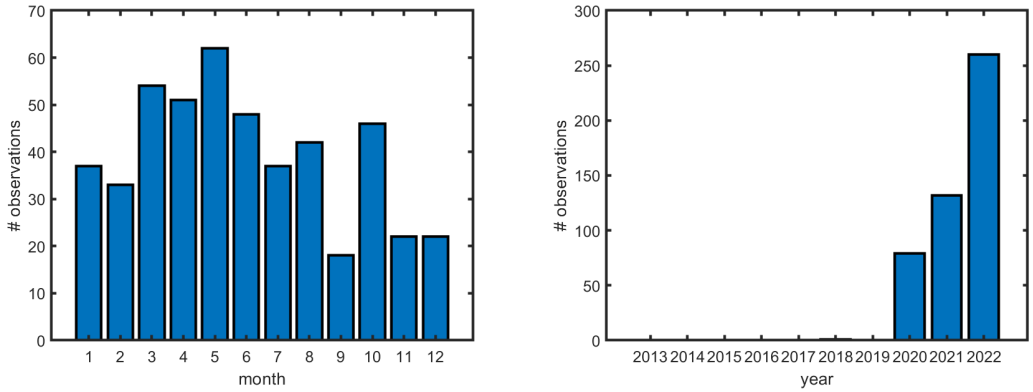


**Figure 5.6:** Number of failures of the single board computer over the months (left panel) and over the years (right panel). In recent years, this number has increased significantly.

### 5.3.1 Aerosol optical depth

From the moment the primary value we are interested in is the vertical aerosol optical depth (VAOD or $\tau$) and not the aerosol extinction coefficient, the inversion procedure is slightly different from that described in Chapter 4. The VAOD is obtained directly from the Raman lidar equation, avoiding the calculation of the first derivative that highlights high-frequency noise. If you are also interested in the extinction coefficient, then this can be obtained directly by deriving the VAOD.
Starting from the Raman lidar equation (Eq. 4.12), the vertical aerosol optical depth can be written as

$$\tau(R,\lambda_{\rm L}) = -\frac{1}{1+\left(\frac{\lambda_{\rm L}}{\lambda_{\rm R}}\right)^k} ln\left(\frac{P(R,\lambda_{\rm L},\lambda_{\rm R})R^2}{T_{\rm mol}(R,\lambda_{\rm L})T_{\rm mol}(R,\lambda_{\rm R})N_{\rm R}(R)}\right) + B \qquad (5.1)$$

where the constant $B$ contains all the range independent factors and the range R is in the region where the full overlap is met.
The molecular contribution was computed from the monthly average profiles from GDAS data [46] using the Rayleigh scattering theory and a 5-component ($N_2$, $O_2$, Ar, $CO_2$ and $H_2O$) atmosphere [77], while tha Ångstrom exponent $k$ was taken equal to 0.7 [45].
Since the value of $B$ is unknown, a calibration procedure must be applied. For low ranges, within the planetary boundary layer, the aerosol optical depth is assumed linear, i.e. the extinction coefficient is constant with range within the PBL:

$$\tau(R,\lambda_{\rm L}) = aR + b.$$

The value of $b$ can be retrieved with a linear regression between $R_{\rm min}$ and $R_{\rm max}$ (for example between 500 m and 1000 m) and it is then subtracted from $\tau$. For ranges where the condition of full overlap is not met, the vertical aerosol optical depth is replaced by this linear relation.

The overall mean profile of the vertical aerosol optical depth is reported in Figure 5.7a. The plot shows a linear behaviour of $\tau$ for small values of $R$ (within the planetary boundary layer) and above this region an asymptotic growth towards the total VAOD. The complete temporal sequence of $\tau$ at three different quotes, 1.5 km, 3.0 km, and 4.5 km above ground level, is shown in Figure 5.7b. A seasonal variability at 3.0 km and 4.5 km is clearly visible, highlighted more prominently in Figure 5.7c where the monthly average values are shown, with lower values in the winter months. Furthermore, periods when the lidar had poor performance are also identifiable. In 2015, the average VAOD is larger when compared to that of other years, and the temporal sequence shows a negative trend over the years. The VAOD values at the three reference heights are however within the estimated standard deviation, and the observed trend is due to the increased number of failures of the single board computer over the last three years, to the "bad periods" 2015 and 2019, and to the profile selection. Finally, in Figure 5.7d, the histograms of these quantities are shown. The average value of the vertical aerosol optical depth found analysing the Raman lidar data at 4.5 km is 0.040 with a standard deviation of 0.019. At 3 km above ground level the mean VAOD is 0.038 with a standard deviation of 0.017 and at 1.5 km it is 0.025 with a standard deviation of 0.011.
The monthly average profiles of $\tau$ are reported in Figure 5.8.

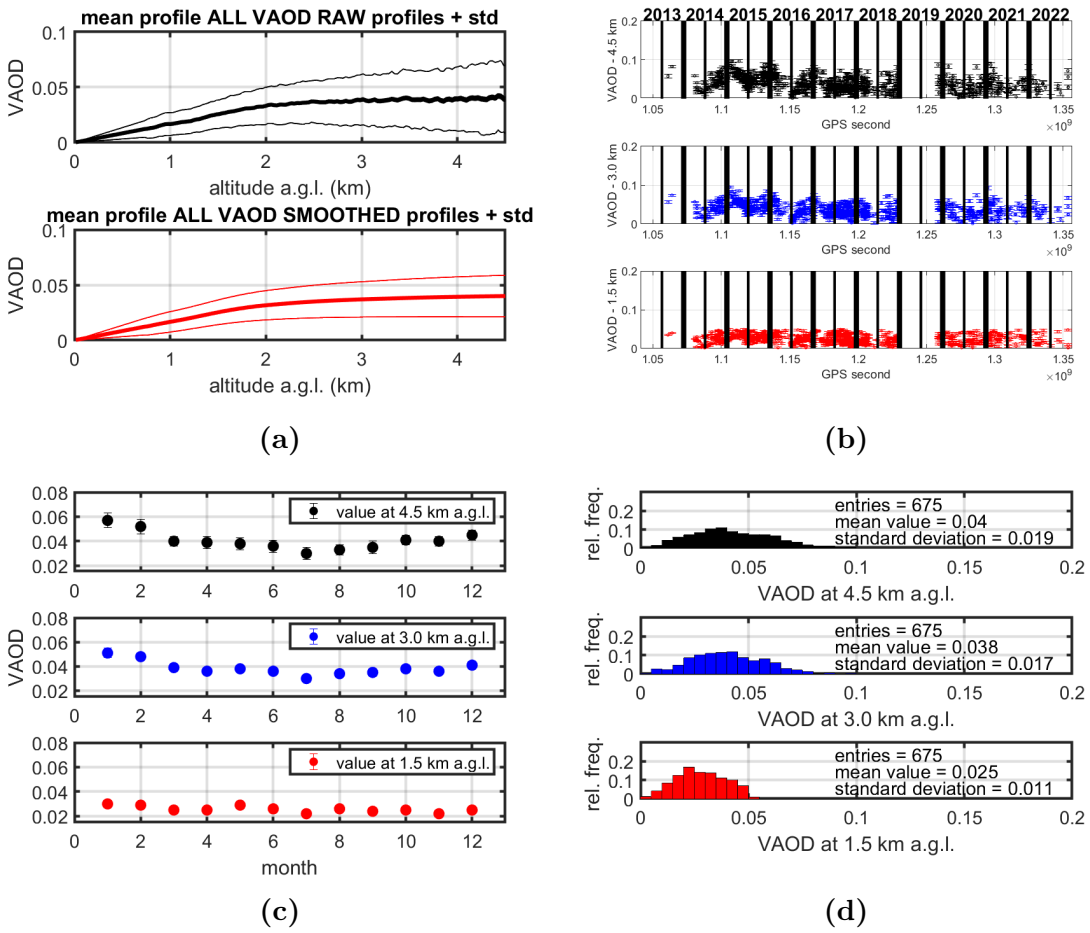


**Figure 5.7:** The vertical aerosol optical depth retrieved with the Auger Raman lidar: (a) overall mean profile; (b) time sequence of VAOD values at 1.5 km, 3.0 km, and 4.5 km; (c) monthly average values of VAOD at 1.5 km, 3.0 km, and 4.5 km; (d) histograms of VAOD values at 1.5 km, 3.0 km, and 4.5 km.

### 5.3.2 Aerosol backscatter coefficient

The procedure used for the retrieval of the aerosol backscatter coefficient is instead similar to the one already described in the previous chapter.
The overall mean profile of the aerosol backscatter coefficient is reported in Figure 5.9a. To make the results comparable with those of the vertical aerosol optical depth, the statistical analysis was performed on the integrated backscatter coefficient:

$$\mathrm{int}\beta(R, \lambda_\mathrm{L}) = \int_0^R \beta_\mathrm{aer}(R', \lambda_\mathrm{L}) dR'.$$

As expected, the same seasonal behaviour has been found: the aerosol integrated backscatter coefficient shows smaller values in the winter seasons (Figures 5.9b and 5.9c). In Figure 5.9d the distributions of the mean values of the integrated aerosol backscatter coefficient at 1.5 km, 3.0 km, and 4.5 km are reported. The average value of int$\beta$ at 4.5 km is 0.0011 1/sr with a standard deviation of 0.0004 1/sr. At 3 km above ground level the mean $int\beta$ is 0.0010 1/sr with a standard deviation of 0.0003 1/sr and at 1.5 km it is 0.0008 1/sr with a standard deviation of 0.0002 1/sr.

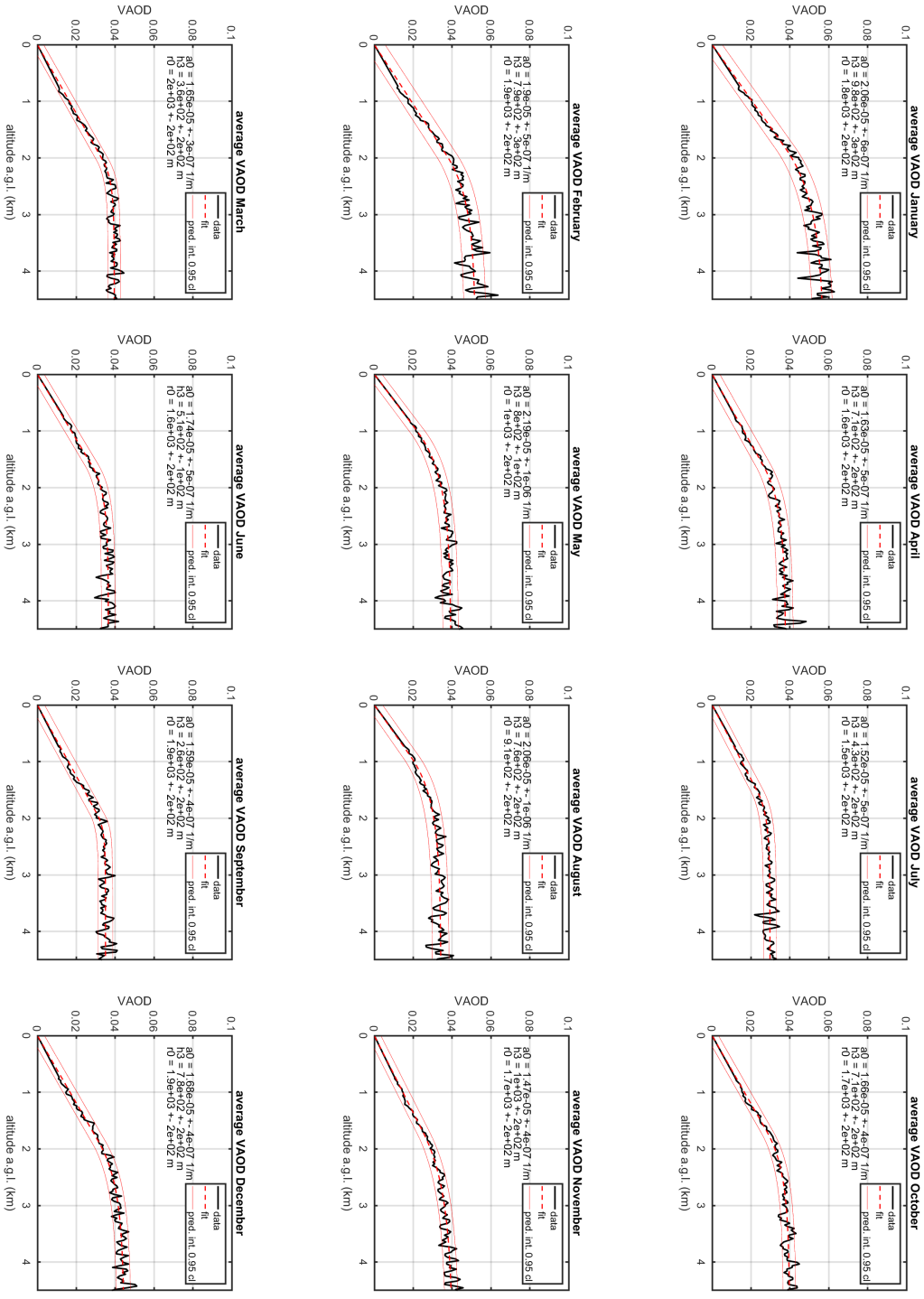


**Figure 5.8:** Monthly average profiles of the vertical aerosol optical depth. In black the measured profiles, in red the three-parameter model.

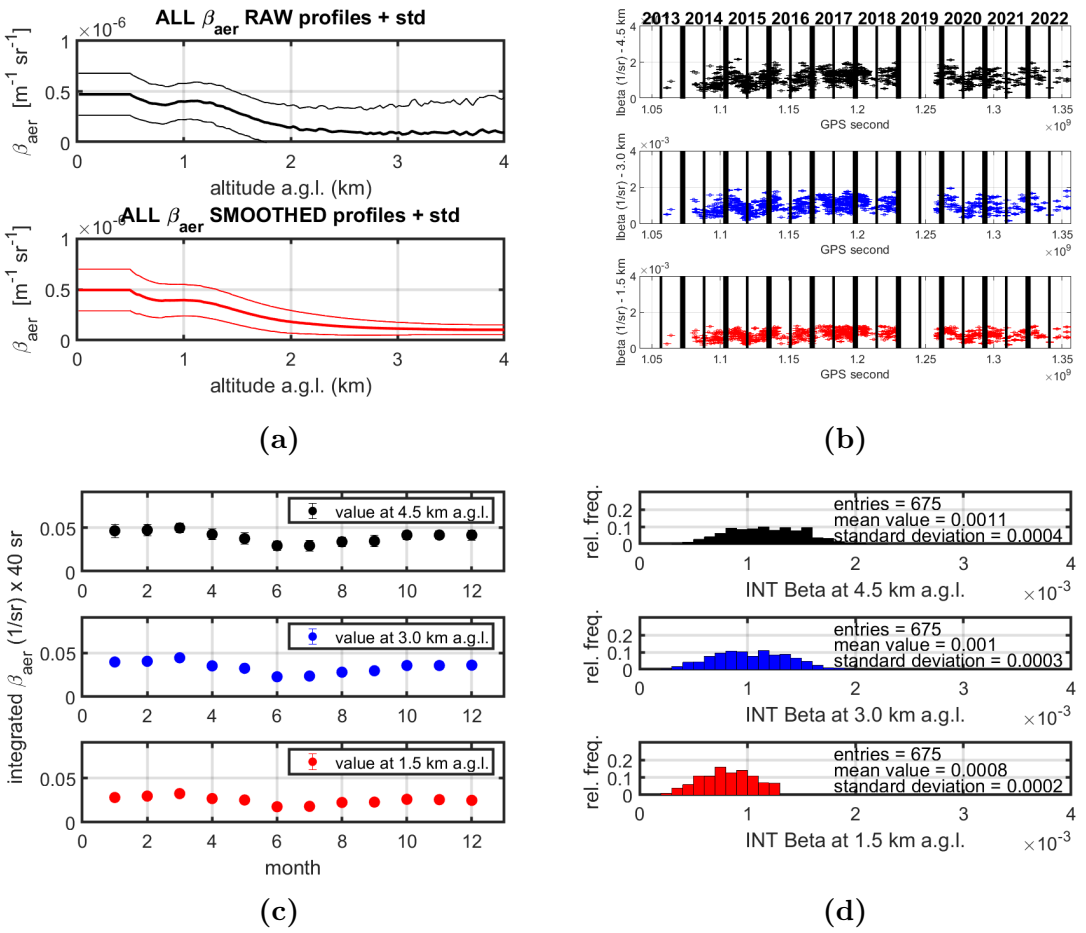


**Figure 5.9:** (a) overall mean profile of the aerosol backscatter coefficient; (b) time sequence of integrated aerosol backscatter coefficient at 1.5 km, 3.0 km, and 4.5 km; (c) monthly average values of int$\beta$ at 1.5 km, 3.0 km, and 4.5 km; (d) histograms of int$\beta$ values at 1.5 km, 3.0 km, and 4.5 km.

## 5.4 Aerosol vertical distribution: a simple model

Within the Pierre Auger Observatory, two independent techniques have been developed to provide the atmospheric aerosol load using CLF laser shots [47]:

- the Data Normalized Analysis;
- the Laser Simulation Analysis.

The first technique is based on the comparison of measured profiles with a clear night profile (no aerosols load). The second method, on the other hand, involves comparing the measured profiles with the simulated profile under different atmospheric conditions (more details in 3.6.2).
In the simulations, the aerosol attenuation is described using two parameters, the aerosol horizontal attenuation length $L_{\text{aer}}$ and the aerosol scale height $H_{\text{aer}}$:

$$\alpha_{\text{aer}}(R) = \frac{1}{L_{\text{aer}}} e^{-\frac{R}{H_{\text{aer}}}} \tag{5.2}$$

and

$$\tau(R) = \frac{H_{\text{aer}}}{L_{\text{aer}}} \left(1 - e^{-\frac{R}{H_{\text{aer}}}}\right) \tag{5.3}$$

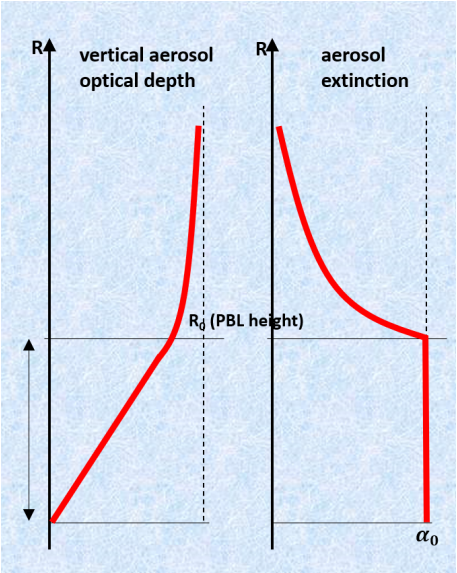


**Figure 5.10:** The three parameter model for aerosol modeling. On the left the vertical aerosol optical depth, on the right side the aerosol extinction coefficient.

In the forthcoming phase, a third parameter will be added to account for the planetary boundary layer. These three parameter model is depicted in Figure 5.10 and is described by:

$$\alpha_{\text{aer}}(R) = \begin{cases} \alpha_{\text{aer}}^{\text{PBL}} & \text{if } R < R_{\text{PBL}} \\ \alpha_{\text{aer}}^{\text{PBL}} e^{-\frac{(R-R_{\text{PBL}})}{H_{\text{aer}}}} & \text{if } R \geq R_{\text{PBL}} \end{cases} \tag{5.4}$$

and

$$\tau(R) = \begin{cases} \alpha_{\text{aer}}^{\text{PBL}} \cdot R & \text{if } R < R_{\text{PBL}} \\ \alpha_{\text{aer}}^{\text{PBL}} R_{\text{PBL}} - \alpha_{\text{aer}}^{\text{PBL}} H_{\text{aer}} \left( e^{-\frac{(R-R_{\text{PBL}})}{H_{\text{aer}}}} - 1 \right) & \text{if } R \geq R_{\text{PBL}} \end{cases} \tag{5.5}$$

with $R_{\text{PBL}}$ the PBL height, $\alpha_{\text{aer}}^{\text{PBL}}$ the aerosol extinction coefficient into the well-mixed PBL, and $H_{\text{aer}}$ the entrainment zone thickness. This means that the extinction coefficient takes constant values within the PBL and then exponentially decreases above this layer.

For this reason, I performed the fitting of the monthly averaged profiles obtained from lidar measurements using both models to see which of the two was more accurate. It should be noted that the same model can be applied to the integrated aerosol backscatter coefficient which is less sensitive to errors due to the overlap function. Results obtained fitting int$\beta$ can be found in [94].

Fit results are shown in Figure 5.11. Figures 5.11a and 5.11b show the parameters obtained from the fit. They exhibit a pronounced seasonal variability for the two-parameter model.

The overall mean values for the two-parameter model are (with their standard deviation):

$$L_{\text{aer}} = (40 \pm 5) \times 10^3 \,\text{m}$$
$$H_{\text{aer}} = (19 \pm 5) \times 10^2 \,\text{m}$$

and for the three parameter model:

$$R_{\text{PBL}} = (16 \pm 4) \times 10^2 \,\text{m}$$

$$H_{\rm aer} = (7 \pm 2) \times 10^2 \,{\rm m}$$
$$\alpha_{\rm aer}^{\rm PBL} = (18 \pm 2) \times 10^{-6} \,{\rm m}^{-1}$$

For each month, lidar measurements at the Pierre Auger Observatory are better described by the three-parameter model. Figure 5.11c shows the Root Mean Squared Error defined as

$$RMSE = \sqrt{\frac{SSE}{\nu}},$$

where $\nu$ is the residual degrees of freedom and $SSE$ is the summed squared of residuals. A value close to zero indicates a fit that is more useful for prediction. Figure 5.11d instead shows the R-Square, the square of the correlation between the predicted values and the experimental ones.

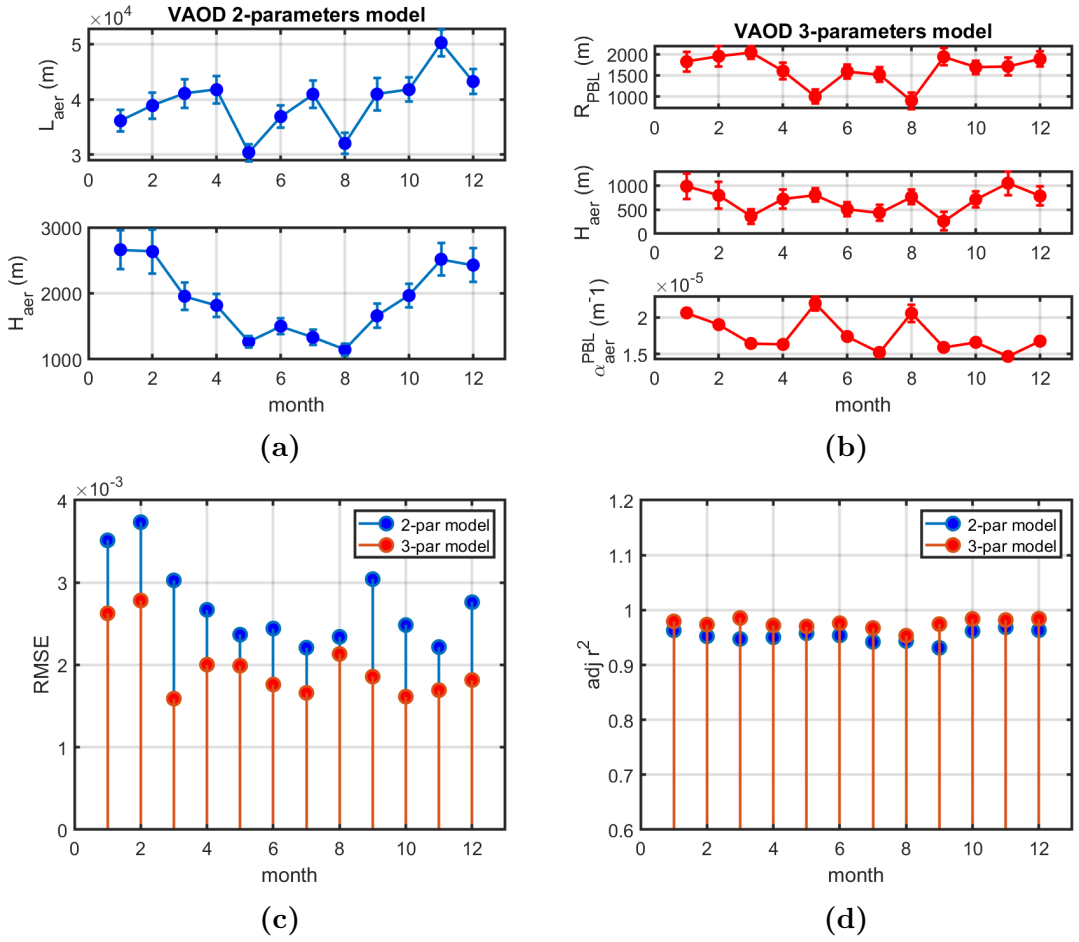


**Figure 5.11:** Results obtained fitting the vertical aerosol optical depth: (a) parameters obtained using the two-parameter model; (b) parameters obtained using the three-parameter model; (c) Root Mean Squared Error of the fit; (d) R-Square.

These Raman lidar data were used to derive the aerosol scale height (two-parameter model) of the reference night. In [95], a model for the upper limit on the possible bias in the measured VAOD is developed. In the Data Normalized Analysis, the clearest night of the year is assumed as night with no aerosol content. The method is therefore sensitive to how good, for this reference night, the approximation of aerosol absence is. Using the stereo energy balance technique [36], an

underestimation of VAOD has emerged. At the reference height of 4.5 km above sea level, it has been found a VAOD correction of 0.005 with an aerosol scale height $H_{\text{aer}} = 1.5\,\text{km}$. The new VAOD systematic uncertainty translates to an uncertainty in energy between 2 % and 4 %, lower than the previous values.

## 5.5 Overlap Function

From the acquired lidar signals it is possible to estimate the overlap function O(R). The evolution of this function over the months can be used as an indication of the alignment state of the system. Unfortunately, to not interfere with FD measurements, it is not possible to perform more accurate tests that require longer integration time (see 6.4).
The procedure to estimate O(R) is based on the fact that the deviation between the backscatter coefficient retrieved with the Klett-Fernald method (see Appendix A) and the Raman solution (described in the previous chapter) is due to the overlap function [96]. The overlap functions of the elastic lidar equation and of the Raman lidar equation are assumed to be the same and this can be a source of uncertainty. Another source of uncertainty is the input lidar ratio used in the Klett-Fernald method.
In this work the retrieved overlap functions were not used to correct the lidar signal but as a check of the system. The obtained curves can be described by [97]:

$$O(R) = A_2 + \frac{A_1 - A_2}{1 + \left(\frac{R}{R_0}\right)^p}.$$

Making hypothesis on the aerosol distribution it is also possible to derive the overlap function from the vertical profile of $\tau$.
Let $\tau$ be the vertical aerosol optical depth as derived in Eq. 5.1 without replacing the values with the linear relation, and $\tau'$ the VAOD obtained assuming that $\tau' = \alpha_{\text{aer}}^{\text{PBL}} \cdot R$ for $R \leq R_0$ (this linear relation is actually substituted in $\tau'$ for $R \leq R_0$) and that the lidar signal used in this second retrieval is corrected for the overlap function $P(R, \lambda_{\text{L}}, \lambda_{\text{R}})/O(R)$. Comparing the equations for $\tau$ and $\tau'$ we obtain

$$\ln O(R) = (\tau'(R) - \tau(R)) \left[1 + \left(\frac{\lambda_{\text{L}}}{\lambda_{\text{R}}}\right)^k\right]. \tag{5.6}$$

Unfortunately the systematic uncertainties in the overlap function retrieval can be large. An example of overlap function obtained with the two methods is shown in the following Figure 5.12.
It is possible to compare the experimentally obtained curves with the theoretical ones [12] shown in Figure 5.13. The overlap function obtained from the measurements on April 22, 2014, is consistent with the theoretical function corresponding to a laser misalignment between $-0.9\,\text{mrad}$ and $-1.2\,\text{mrad}$.

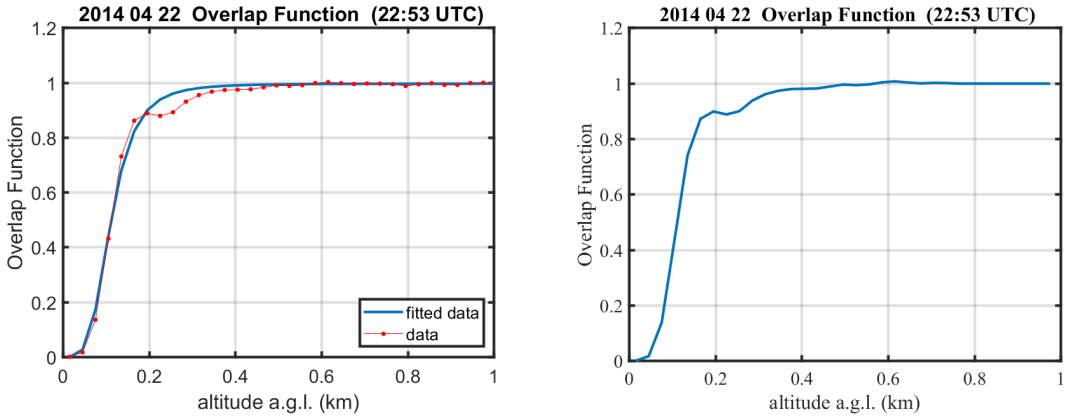


**(a)** **(b)**

**Figure 5.12:** Example of overlap function retrieved with the two methods described in the text: (a) comparing the backscatter coefficients retrieved with the Klett-Fernald method and with the Raman technique; (b) from the VAOD profile.

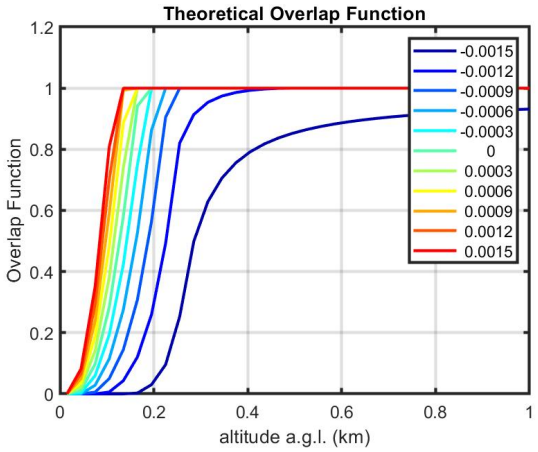


**Figure 5.13:** Theoretical overlap function of the Auger Raman lidar. The different curves correspond to different disalignments of the laser beam with respect to the optical axis of the telescope (ranging from -1.5 mrad to 1.5 mrad, with positive values for laser beam directions towards the telescope axis).

# Chapter 6

# The AQ Raman lidar

## 6.1 Introduction

As we have seen, atmospheric Lidars are of fundamental importance for characterizing the atmosphere both before the construction of an observatory for cosmic rays and during data collection. The most crucial parameters for these observatories are the optical thickness of aerosols and the mixing ratio of water vapor.
In the Lidar laboratory of DSFC/UNIVAQ, we are developing a Raman Lidar system that is easily upgradable, simple to maintain, does not require specialized personnel, and is relatively cost-effective. These objectives are achieved through the use of a fiber bundle in the receiver which splits the light collected by the telescope into five channels. With the Lidar's planned integration into ACTRIS, we are currently studying the addition of a channel for studying the depolarization ratio of aerosols and an elastic channel at 1064 nm.
Although the Lidar will remain at the University of L'Aquila, it will serve as a testbed for future instruments to be installed at astrophysical observatory sites. This chapter describes the instrument we have developed, the tests conducted, and presents the results of some measurements.

**Figure 6.1:** The lidar system described in this chapter.

## 6.2 Hardware

This system (Figure 6.1), called AQ Raman Lidar, is a multiwavelength Raman lidar with five working channels:

1. elastic channel at 354.7 nm (UV-AIR);
2. nitrogen Raman channel at 386.7 nm (UV-N2);
3. water vapor Raman channel at 407.6 nm (UV-H2O);
4. elastic channel at 532.1 nm (VIS-AIR);
5. nitrogen Raman channel at 607.6 nm (VIS-N2).

To these channels an elastic infrared channel at 1064 nm and a polarization channel will be added (a second telescope will be added for these channels).

### 6.2.1 Transmitter

**Laser**

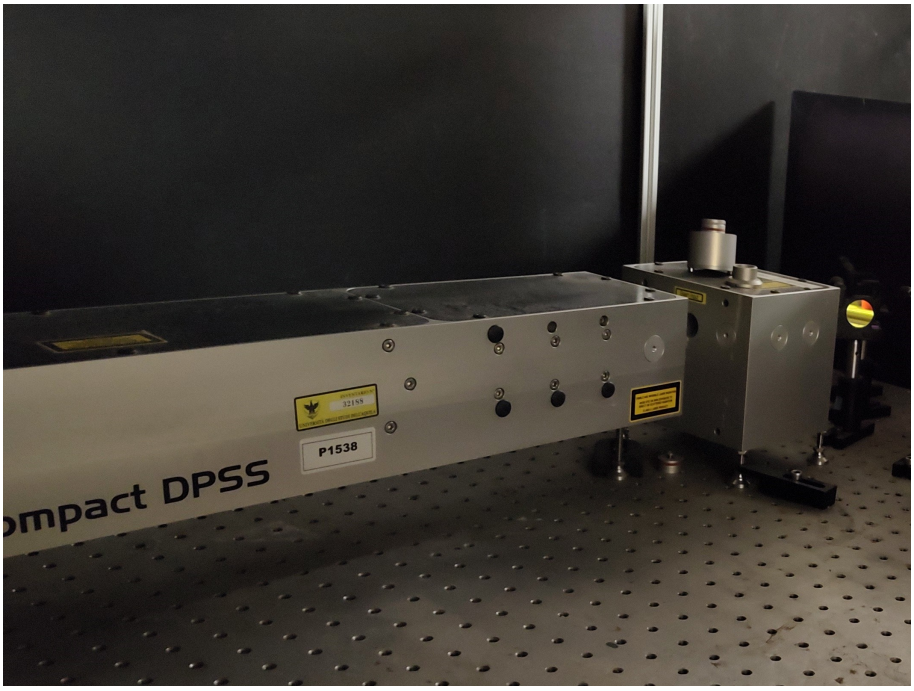


**Figure 6.2:** The Innolas SpitLight Compact DPSS 100 laser.

The laser utilized for this project is the SpitLight Compact DPSS 100, crafted by Innolas. This Nd-YAG laser, widely adopted in current applications, emits radiation at three wavelengths: 355 nm, 532 nm, and 1064 nm, achieved through frequency doubling and tripling. Key specifications, furnished by the manufacturer, are outlined in Table 6.1.
Operating at a repetition rate of 100 Hz, the laser necessitates a chiller to maintain optimal performance at this frequency.

**Table 6.1:** Innolas SpitLight Compact DPSS 100 specifications

| Laser parameters | Repetition Rate | Specifications for 100 Hz |
|---|---|---|
| Energy | Pulse Energy at 1064 nm | $> 100$ mJ |
| | Pulse Energy at 532 nm | $> 60$ mJ |
| | Pulse Energy at 355 nm | $> 30$ mJ |
| | Energy stability at 1064 nm | $< 0.5$ % |
| | Energy stability at 532 nm | $< 1.0$ % |
| | Energy stability at 355 nm | $< 1.5$ % |
| Beam Parameters | Pulse Width at 1064 nm | 8-10 ns |
| | Divergence | $< 0.5$ mrad |
| | Pointing Stability | $< \pm 50$ µrad |
| | Beam Diameter | 5 mm |
| | Temporal Jitter | $< \pm 1$ ns |
| Weights | Laser Head | 10 kg |
| | Power Supply | 25 kg |
| Dimensions | Laser Head (in infrared) | 370 x 115 x 91 mm |
| | Power Supply | 480 x 220 x 480 mm |

### Beam Splitters and Beam Expanders

The laser beam is directed into the sky using dichroic beamsplitters, optical systems designed to exhibit high reflectance only for radiation at specific wavelengths and precise incident angles. The Thorlabs HBSY11, HBSY12, HBSY13 (1-inch diameter), and HBSY21, HBSY22, HBSY23 (2-inch diameter) models are employed for this purpose.
Within the optical path, beam expanders are integrated between the 1-inch and 2-inch beam splitters. Essentially, these are Galilean telescopes that maintain a constant product of the beam aperture with the beam diameter. By increasing the beam section, they effectively reduce the beam's divergence.
The beam expanders utilized for the AQ Raman lidar are produced by Thorlabs, specifically the models BE05-355 and BE05-532. These beam expanders are optimized for wavelengths of 355 nm and 532 nm, respectively, expanding the beam diameter by a factor of five.

**Figure 6.3:** Transmission optics for laser beams at 355 nm (bottom) and 532 nm (top).

### 6.2.2 Receiver

The backscattered photons are collected by a reflector telescope with a parabolic mirror of 20 cm diameter and 60 cm focal length. The mirror was manufactured by the Italian company Marcon.

#### Optical Fiber

One of the peculiarities of our lidar system is the use of a bundle of optical fibers in the receiver to separate the photons collected by the telescope into five channels and deliver them to the photomultipliers. This solution eliminates the need for beam splitters to select the desired wavelength and simplifies the alignment of the optics in the receiving part. In standard lidar systems, height and orientation of beam splitters, notch filters, interference filters, collimator and focusing lenses must be adjusted with high precision. Using the fiber bundle, the tuning of the receiver is significantly simplified and does not require personnel experienced in LiDAR systems. Moreover, in some cases, to change the purpose of the channel, it is sufficient to replace only the interference filter. To the best of my knowledge, there are currently no other lidars utilizing this solution, and the purpose of this work is to test its functionality.

The fiber bundle entrance has a diameter of 8 mm while each output has a diameter of 3.6 mm. It consists of 925 optical fibers manufactured by CeramOptec. Each fiber has a core (made of fused silica glass) with a diameter of 200 µm, a cladding diameter of 220 µm, a buffer diameter of 245 µm, a numerical aperture of 0.22, a step-index profile, and a high OH content for enhanced performance in the UV region (although, it's worth noting that the presence of OH significantly reduces transmission for wavelengths greater than 1.4 µm). These distinct fibers are then randomly distributed among the five outputs.
Despite the randomization, when the beam spot size is too small, the distribution of photon numbers becomes uneven, resulting in output variations even with different positions of illumination at the bundle entrance. This phenomenon is illustrated in Figure 6.4, which presents the results of illumination tests. In (a), a LED lamp was employed to uniformly illuminate the entire input of the fiber bundle, resulting in consistent radiation measurements across all five outputs. In (b), a Melles Griot HeNe laser was used with a divergence of 1.7 mrad, yielding a small entering beam diameter of only 0.89 mm at a 12° input angle—close to the maximum accepted ($\theta_{MAX} = sin^{-1}NA$). Noticeable differences in outgoing radiation are observed. In (c) and (d), the same laser source was used but with a 5x beam expander (with input angles of 0° and 12° respectively), resulting in diminished differences.
In a lidar system, signals returning from different ranges could potentially be focused in various sections of the fiber bundle. However, by introducing a defocus of a few millimeters, the spot size at the entrance of the fiber bundle becomes sufficiently large to mitigate such issues. The five different positions utilized in our tests are illustrated in Figure 6.5.

Using a Thorlabs CCS100 spectrometer, I conducted an analysis of the spectral transmission of the optical fibers. A Hamamatsu xenon lamp served as the light source, enabling an investigation of the spectral response in the UV region as well. In Figure 6.6, the spectra of the Xe lamp before and after the fiber bundle are presented.

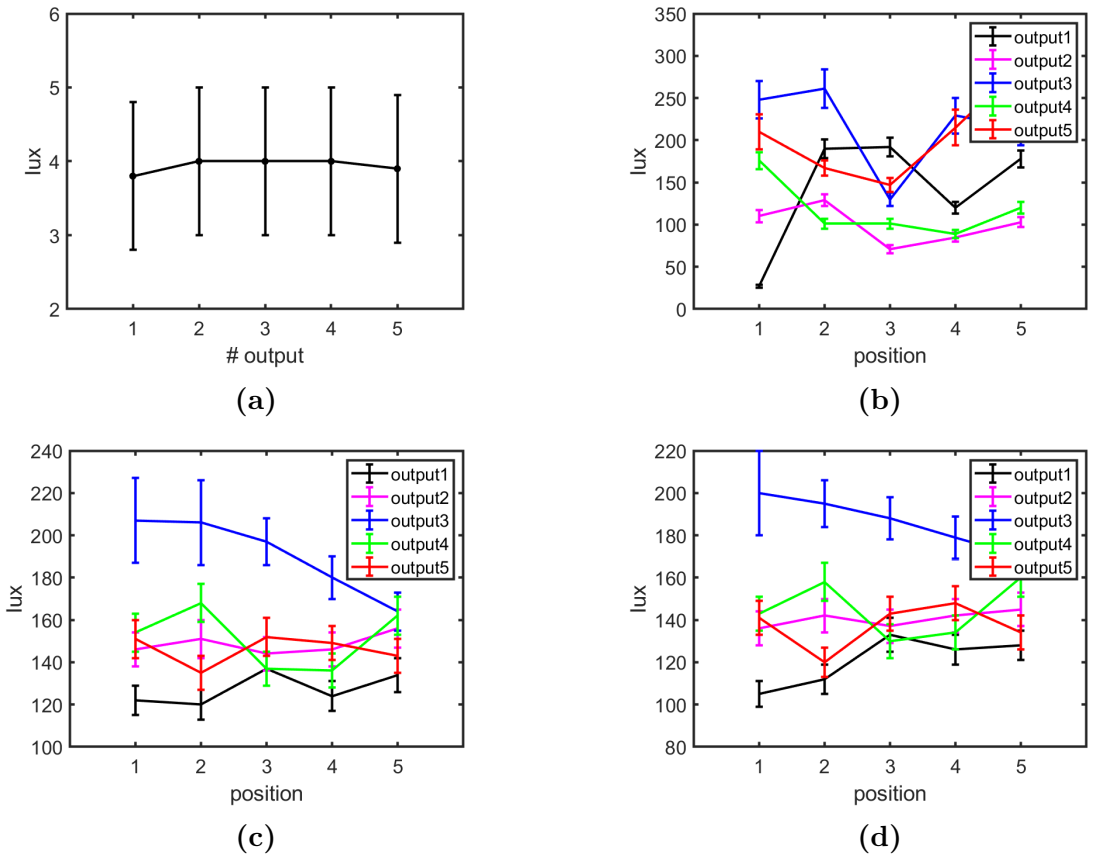


**Figure 6.4:** Fiber bundle illumination test: (a) uniform illumination of the bundle entrance with a led lamp; (b) illumination with a laser source with a beam diameter ∼1 mm and an input angle of ∼12°; (c)illumination with a laser source plus beam expander with a resulting beam diamter of ∼5 mm and an input angle of ∼0°; (d) as (c) but with an input angle of ∼12°.

### Interference Filters

The selection of the desired wavelengths is done with ultra-narrow band interference filters manufactured by Alluxa. The characteristics of the filters are reported in Table 6.2 while the transmission curves are reported in Figure 6.7. The experimental curves were obtained during my master thesis work with a calibrated lamp Hamamatsu L7810 and a spectrometer Thorlabs CCS100 (unfortunately the spectral range of the spectrometer is limited to 1000 nm and for the IR filter only the manufacturer curve is shown).

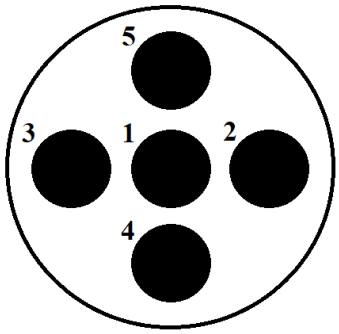


**Figure 6.5:** The fiber bundle entrance with the five positions of the incoming radiation (front view).

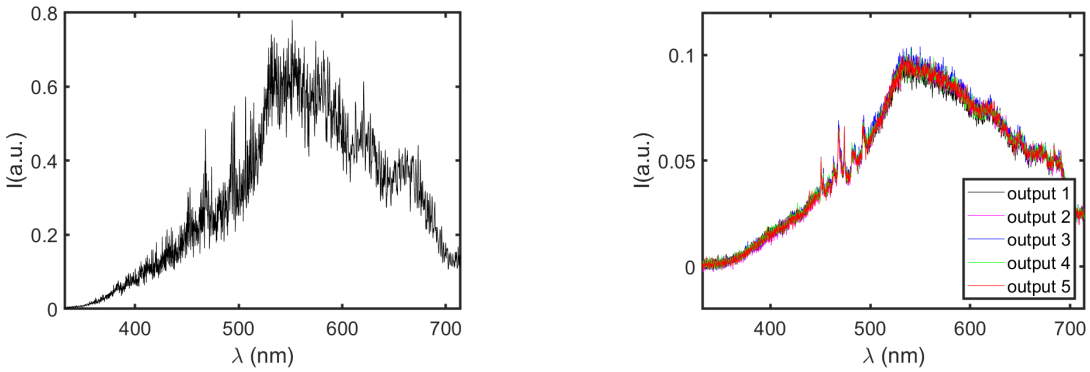


**Figure 6.6:** Hamamatsu Xe lamp spectrum before and after transmission through the fiber bundle.

**Table 6.2:** Interference filters specifications (provided by Alluxa)

| Center Wavelength (nm) | FWHM (nm) | T @peak (%) | OD average (out of band) | Effective Refractive Index |
|---|---|---|---|---|
| 354.70 ± 0.15 | 0.5 ± 0.1 | >70% | >7 | 1.83811 |
| 386.70 ± 0.15 | 0.5 ± 0.1 | >70% | >7 | 2.2274 |
| 407.60 ± 0.15 | 1.0 ± 0.1 | >70% | >7 | 2.08442 |
| 532.10 ± 0.15 | 0.5 ± 0.1 | >70% | >7 | 2.00224 |
| 607.60 ± 0.15 | 1.0 ± 0.1 | >70% | >7 | 1.84736 |
| 1064.10 ± 0.15 | 1.0 ± 0.1 | >70% | >7 | 1.95112 |

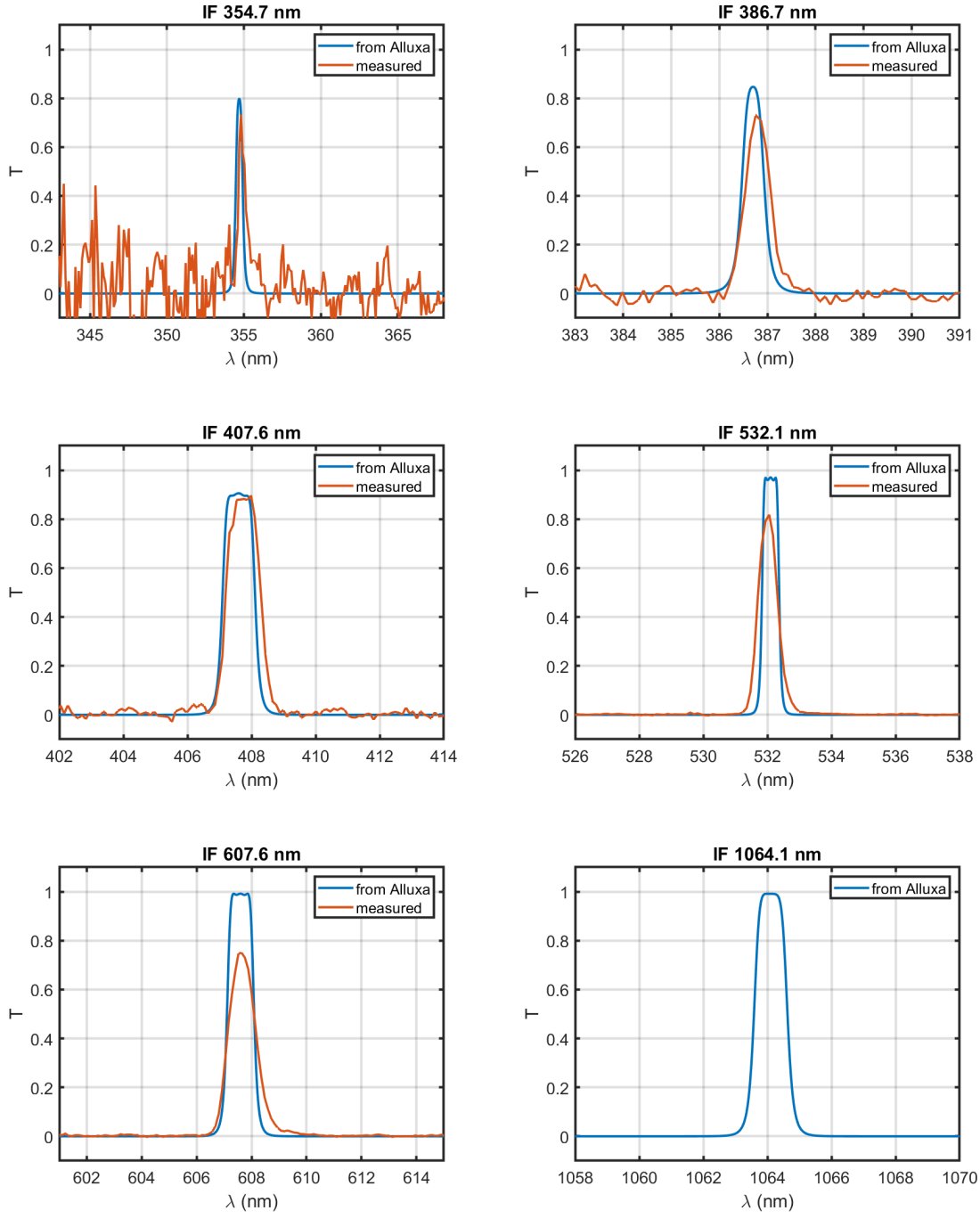


**Figure 6.7:** Interference filters transmissions: in blue the curves provided by Alluxa, in red the measured ones.

### Fiber Launcher

The task of the fiber launcher is to couple the output of the optical fiber with the detector. It consists of two plano-convex lenses (Thorlabs LA1951-A) assembled with Thorlabs 1" Lens Tubes (Figure 6.8). The interference filter is placed between the two lenses. Furthermore it is possible to mount neutral density filters before the detector to reduce the intensity of the backscattered light and avoid saturation. The filters used are the Thorlabs NUK01.


**Figure 6.8:** Assembled fiber launcher (VIS-AIR channel).

As the interference filter is tilted the transmission curve is shifted towards shorter wavelengths according to [98, 99]:

$$\lambda_\theta = \lambda_0 \sqrt{1 - \left(\frac{n_0}{n_{eff}} sin\theta\right)^2} \tag{6.1}$$

where $\lambda_0$ is the wavelength of the spectral feature at normal incidence, $\lambda_\theta$ is the wavelength of the same feature for angle of incidence $\theta$, $n_0$ is the refractive index of the medium, and $n_{eff}$ is the effective refractive index of the filter.
Due to this wavelength shift, the system selects different Raman lines whose backscattering cross-sections dependence on temperature varies with the rotational number J. Thus we can introduce a temperature dependence in the recorded signals, and since in the atmosphere temperature varies with altitude, we can introduce a range bias.

Using the software Zemax [100], I estimated the distance between the fiber output and the first lens of the fiber launcher for which light rays strike the interference filter with the smallest angle of incidence. The scheme of the fiber launcher is reported in Figure 6.9.
The Geometric Image Analysis in Zemax provide the efficiency, i.e. the fraction of light rays which strike a surface, in this case the interference filter, within a given numerical aperture ($NA_{\text{cutoff}}$). Hence I evaluated these efficiencies varying the distance between the fiber bundle output and the first lens for the five channels. In Zemax I defined several fields, i.e. points of the fiber bundle which act as light

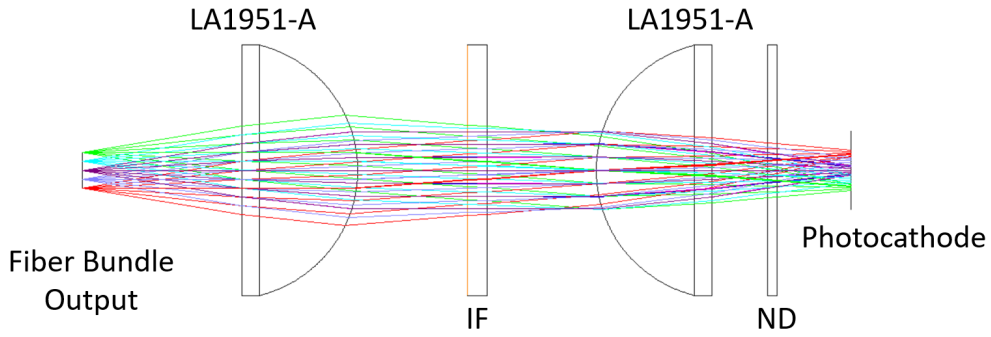


**Figure 6.9:** The fiber launcher in Zemax. Different colors correspond to different fields.

source. In Figures 6.10 and 6.11, field 1 indicates a fiber located at the center of the bundle, field 6 a fiber at 0.9 mm from the center, and field 2 a fiber at 1.8 mm from the center (edge of the bundle).

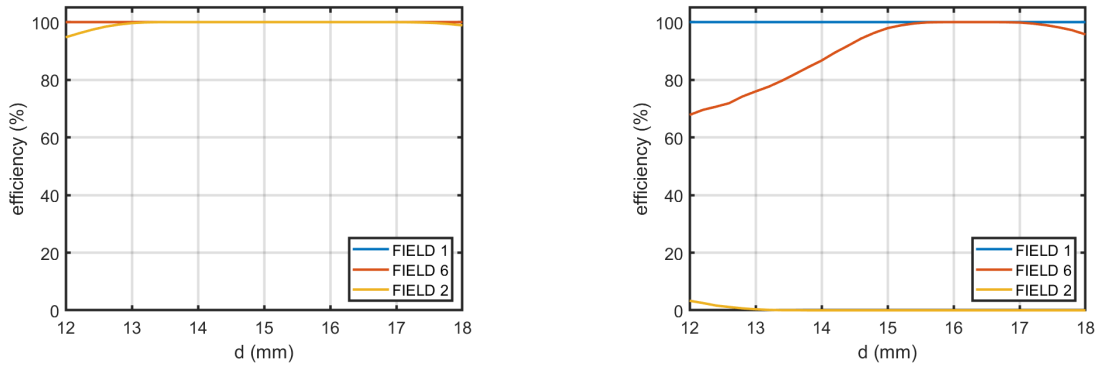


**(a)** $NA_{\text{cutoff}} = 0.10$ **(b)** $NA_{\text{cutoff}} = 0.05$

**Figure 6.10:** Efficiencies for several fields and cutoffs determined with Zemax. For distancis between 13 mm and 17 mm, all the rays reach the interfenrence filter with $NA \leq 0.10$, whileno ray from the edge of the fiber reaches the filter with $NA \leq 0.10$.

Results (Figure 6.10) show as efficiencies can reach 100% for all fields and $NA_{\text{cutoff}} = 0.10$ while with $NA_{\text{cutoff}} = 0.05$ the efficiencies for field 2 are almost zero. Therefore I have considered the case $NA_{\text{cutoff}} = 0.08$ (Figure 6.11). The maxima of the curves are reported in Table 6.3 and occur at distances slightly different from the back focal length of the lens.

With the results of the simulation I tried to determine an effective transmission of the Alluxa filters. Assuming the whole fiber output illuminated, I defined an average efficiency as

$$X(\text{NA}^i_{\text{cutoff}}) = \frac{\int_0^R \epsilon(r, \text{NA}^i_{\text{cutoff}}) 2\pi r \text{d}r}{\pi R^2} \tag{6.2}$$

where $\text{NA}_{\text{cutoff}} = [0.01,\ 0.02,\ 0.03,\ 0.04,\ 0.05,\ 0.06,\ 0.07,\ 0.08,\ 0.09,\ 0.10]$ is the numerical aperture cutoff (rays with larger angle of incidence on the interference filter are neglected), $\epsilon(r, \text{NA}^i_{\text{cutoff}})$ is the correspondent efficiency given by Zemax, $r$

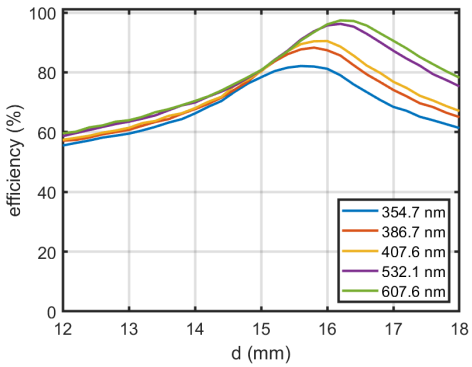


**Figure 6.11:** Efficiencies for field 2 and $NA_{\text{cutoff}} = 0.08$ determined with Zemax.

**Table 6.3:** Distances which maximize efficiencies for field 2 and $NA_{\text{cutoff}} = 0.08$

| Wavelength (nm) | Distance (mm) |
|---|---|
| 354.7 | 15.8 |
| 386.7 | 15.8 |
| 407.6 | 16.0 |
| 532.1 | 16.2 |
| 607.6 | 16.2 |

is the distance from the center of the fiber bundle output (Figure 6.12), $R$ is the radius of the fiber bundle output.
Then I determined the factors $X_2$ to weight the transmission curves of IFs:

$$X_2 = \left[X(\text{NA}^1_{\text{cutoff}}),\ X(\text{NA}^2_{\text{cutoff}}) - X(\text{NA}^1_{\text{cutoff}}), \ldots, X(\text{NA}^{10}_{\text{cutoff}}) - X(\text{NA}^9_{\text{cutoff}})\right]$$

The effective transmission can then be computed with

$$T_{\text{E}}(\lambda) = \sum_{i=1}^{10} T\left(\frac{\theta_i + \theta_{i-1}}{2}, \lambda\right) X_2(i) \tag{6.3}$$

where $T$ is calculated using Eq. 6.1.
For each channel, I also computed

$$F_X(T) = \frac{\displaystyle\int_{\Delta\lambda} \frac{\mathrm{d}\sigma_X(\lambda', \pi, T)}{\mathrm{d}\Omega} T_{\text{E}}(\lambda')\mathrm{d}\lambda' - \int_{\Delta\lambda} \frac{\mathrm{d}\sigma_X(\lambda', \pi, T = 300K)}{\mathrm{d}\Omega} T_{\text{E}}(\lambda')\mathrm{d}\lambda'}{\displaystyle\int_{\Delta\lambda} \frac{\mathrm{d}\sigma_X(\lambda', \pi, T = 300K)}{\mathrm{d}\Omega} T_{\text{E}}(\lambda')\mathrm{d}\lambda'} \tag{6.4}$$

(see Appendix B) where $\Delta\lambda$ is the filter passband and $X$ can be $N_2$, $O_2$ or $H_2O$. For the elastic channels I considered both nitrogen and oxygen cross sections multiplied by 0.79 and 0.21 respectively. The Raman backscattering cross sections are obtained following [79] for nitrogen and oxygen, and [101] for water vapour.
The introduced temperature dependences, Figures 6.13, 6.14, 6.15, 6.16 and 6.17, have turned out to be negligible.

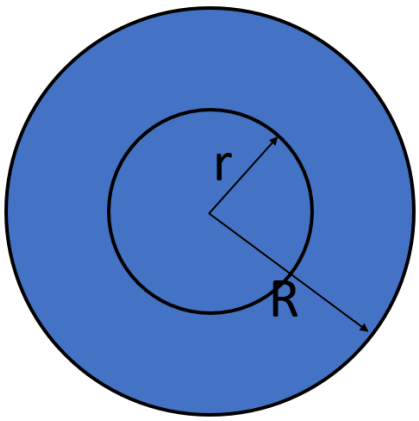


**Figure 6.12:** Fiber bundle output.

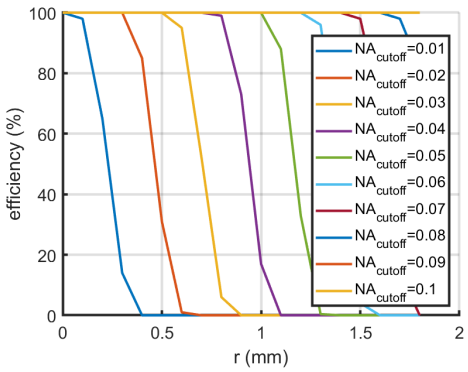


**(a)** Efficiencies

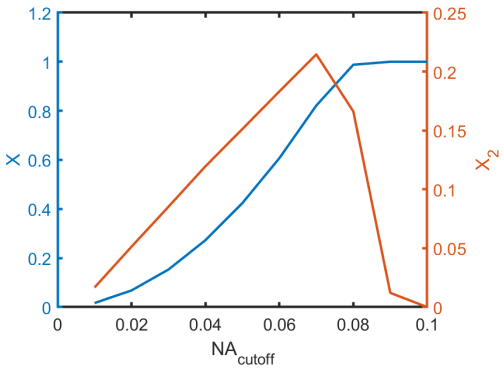


**(b)** Weights

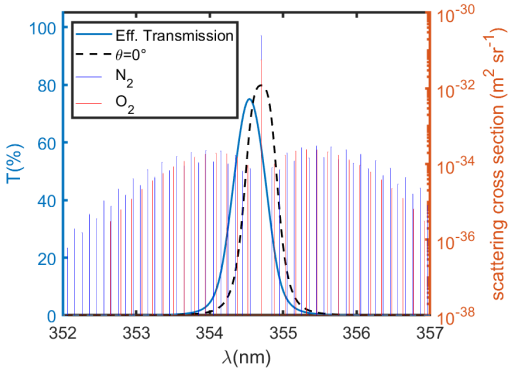


**(c)** Effective transmission

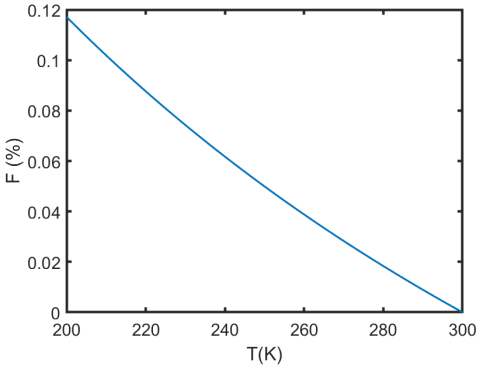


**(d)** Temperature dependence

**Figure 6.13:** UV-AIR channel effective transmission: (a) efficiencies determined with Zemax; (b) weights for the estimation of filter transmission; (c) effective transmission; (d) backscattering temperature dependence.

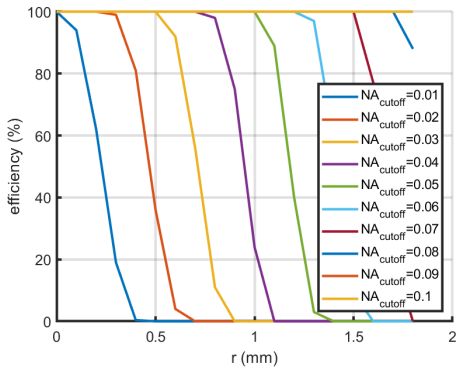


**(a)** Efficiencies

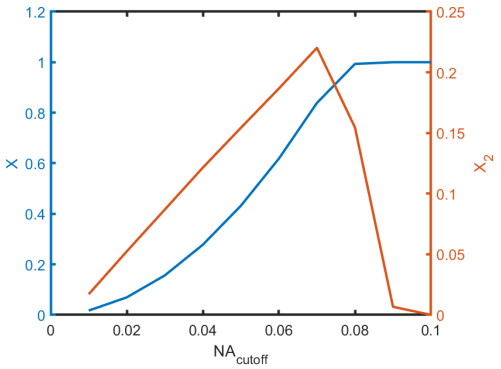


**(b)** Weights

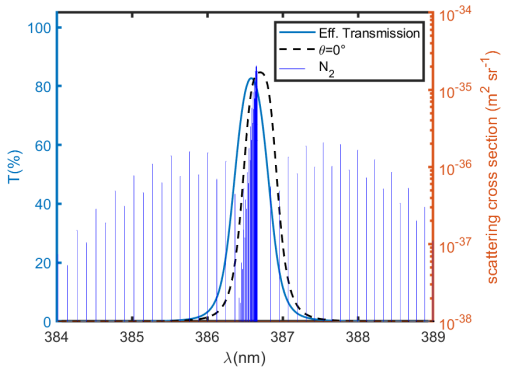


**(c)** Effective transmission

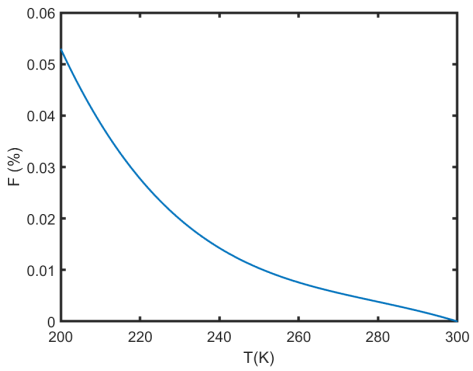


**(d)** Temperature dependence

**Figure 6.14:** UV-N2 channel effective transmission: (a) efficiencies determined with Zemax; (b) weights for the estimation of filter transmission; (c) effective transmission; (d) backscattering temperature dependence.

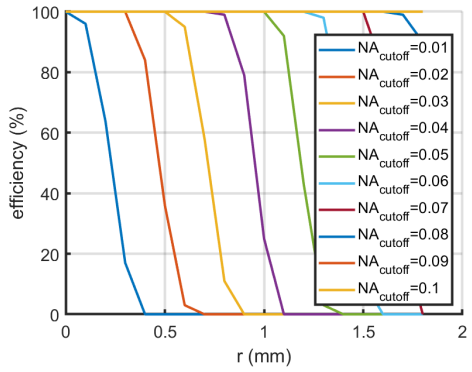


**(a)** Efficiencies

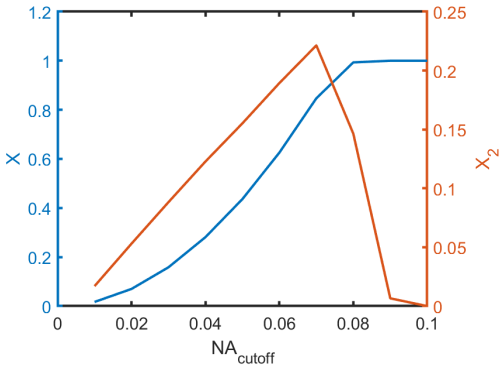


**(b)** Weights

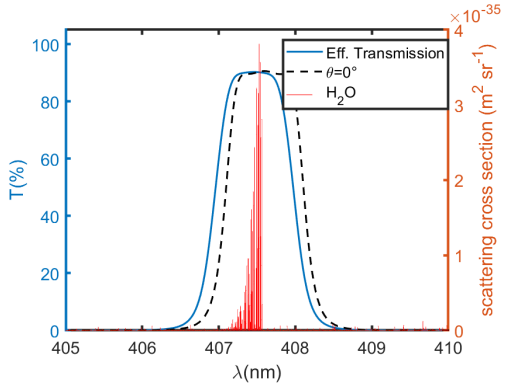


**(c)** Effective transmission

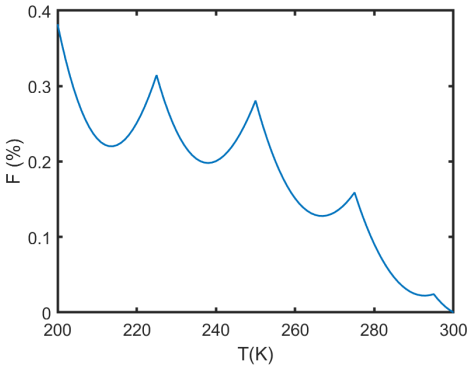


**(d)** Temperature dependence

**Figure 6.15:** UV-H2O channel effective transmission: (a) efficiencies determined with Zemax; (b) weights for the estimation of filter transmission; (c) effective transmission; (d) backscattering temperature dependence.

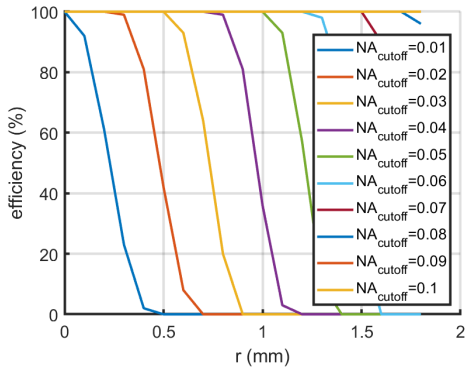


**(a)** Efficiencies

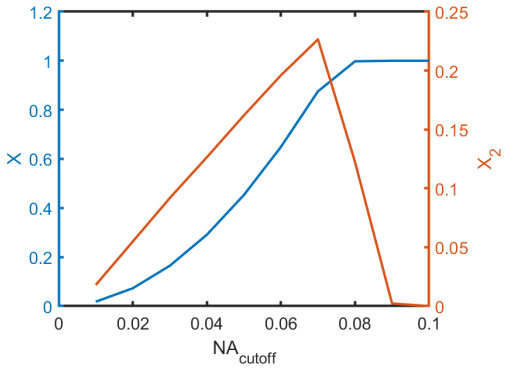


**(b)** Weights

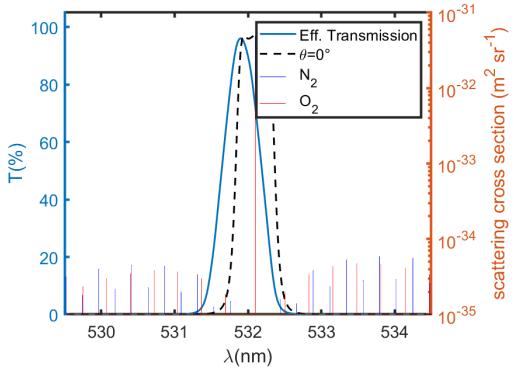


**(c)** Effective transmission

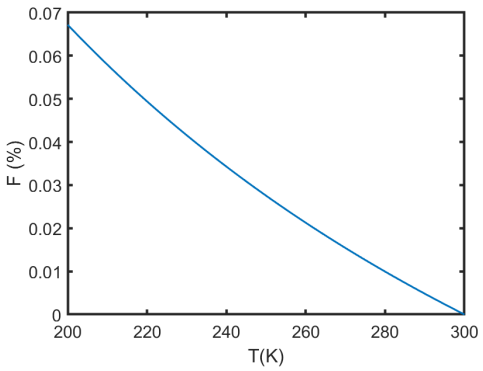


**(d)** Temperature dependence

**Figure 6.16:** VIS-AIR channel effective transmission: (a) efficiencies determined with Zemax; (b) weights for the estimation of filter transmission; (c) effective transmission; (d) backscattering temperature dependence.

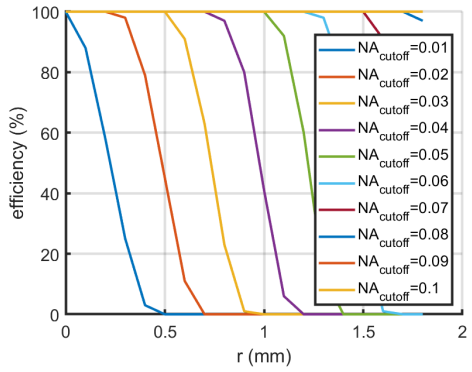


**(a)** Efficiencies

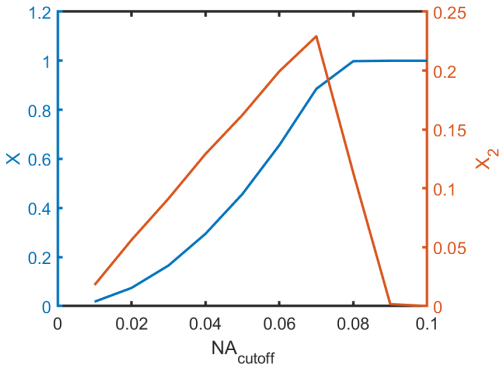


**(b)** Weights

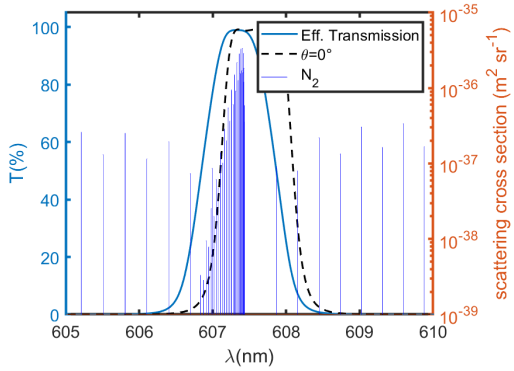


**(c)** Effective transmission

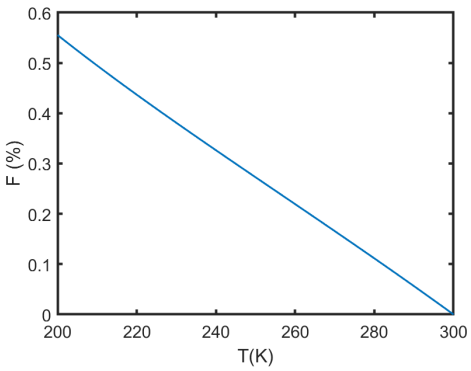


**(d)** Temperature dependence

**Figure 6.17:** VIS-N2 channel effective transmission: (a) efficiencies determined with Zemax; (b) weights for the estimation of filter transmission; (c) effective transmission; (d) backscattering temperature dependence..

### Photomultiplier Tubes

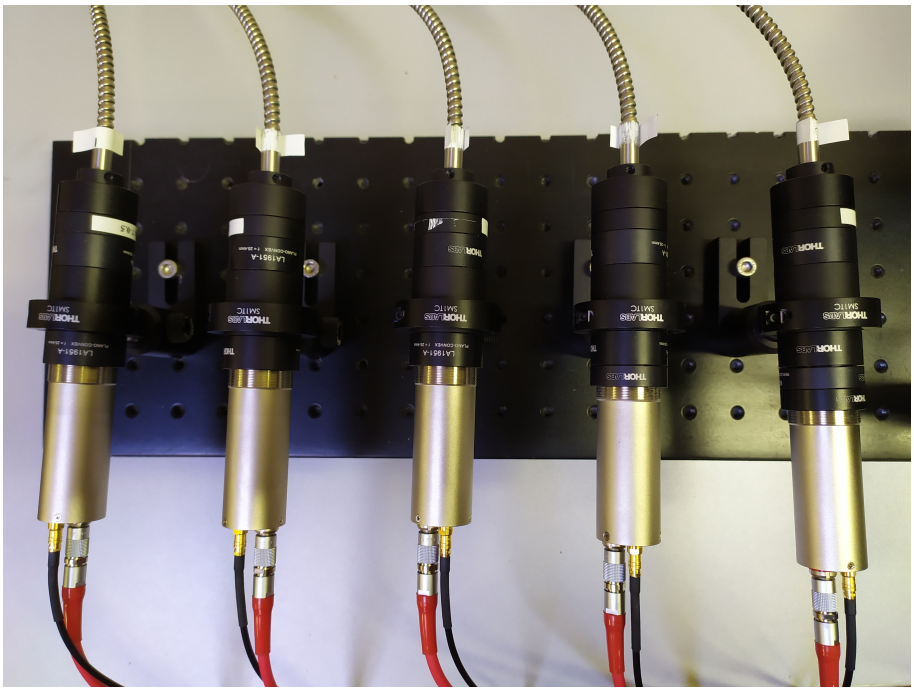

**Figure 6.18:** The five assembled photomultiplier tubes and the fiber launchers.

The photomultiplier tubes are built on the Hamamatsu R9880U-113 module. The specifications are listed in the following Table 6.4.

**Table 6.4:** Hamamatsu R9880U-113 specifications from datasheet

| R9880U-113 | |
|---|---|
| Wavelength Range (nm) | 185-700 |
| Wavelength Peak (nm) | 400 |
| Max Supply Volt. (V) | 1100 |
| Max Avg. Anode Current (mA) | 0.1 |
| Gain Typ. @ 1000 V | $2.0 * 10^6$ |
| Rise time Typ. @ 1000 V(ns) | 0.57 |
| Transit time Typ. @ 1000 V(ns) | 2.7 |
| Operating temperature (°C) | -80 to 50 |

The photomultipliers were tested connected to the fiber launcher, with the corresponding interference filters mounted. The objective of these tests is to initially determine, for each photomultiplier, the optimal supply voltage. Additionally, since the dark current pulses typically distribute on the left side of the histogram, the goal is to establish the threshold that effectively discriminates a light signal from noise. However, the precise adjustment of supply voltages and detection thresholds is carried out by directly observing a lidar return signal with an oscilloscope.
Figure 6.19 displays typical signals without amplification, showcasing single photoelectron pulses. The analysis of oscilloscope traces provides estimations for the pulse width (FWHM) denoted as $t_w$ and the rising time (time taken for the signal

to increase from 10% to 90% of its final value) represented as $t_r$, as summarized in Table 6.5.

The pulse height distributions for the five tubes are reported in Figure 6.20 for several values of the high voltage. Some voltages have been omitted from the plots for a better clarity, and the minima of the curves are reported in Table 6.6. The threshold values range between 0 and -25 mV and correspond to 64 discriminator levels.

In conclusion, a dead time of 3.9 ns was estimated by comparing lidar signals with the corresponding lidar signals suitably attenuated with a neutral density filter to avoid photon overlap [78].

**Table 6.5:** PMTs response pulse width and rising time. The estimated uncertainty is 0.5 ns

| Channel | $t_w$ (ns) | $t_r$ (ns) |
|---|---|---|
| 1 | 2.5 | 2 |
| 2 | 2.5 | 2 |
| 3 | 2.5 | 2 |
| 4 | 2.5 | 2 |
| 5 | 2.5 | 2 |

**Table 6.6:** Minima, in discriminator levels, of the pulse height distribution curves. One discriminator level corresponds to -0.4 mV

| HV (V) | UV-AIR | UV-N2 | UV-H2O | VIS-AIR | vis-N2 |
|---|---|---|---|---|---|
| -750 | - | - | - | - | - |
| -760 | - | - | - | - | - |
| -770 | - | 2 | - | 2 | - |
| -780 | 1 | 3 | 2 | 3 | 2 |
| -790 | 5 | 5 | 3 | 5 | 4 |
| -800 | 7 | 5 | 5 | 6 | 4 |
| -810 | 7 | 6 | 6 | 7 | 5 |
| -820 | 8 | 7 | 7 | 8 | 7 |
| -830 | 11 | 10 | 8 | 9 | 7 |
| -840 | 12 | 11 | 10 | 12 | 8 |
| -850 | 13 | 12 | 12 | 12 | 10 |
| -860 | 15 | 14 | 13 | 13 | 11 |
| -870 | 16 | 16 | 15 | 16 | 12 |

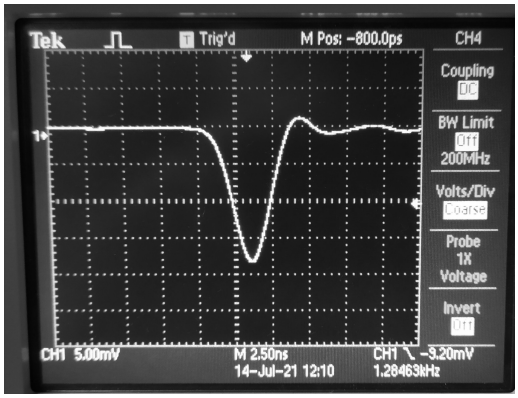


**(a)** UV-AIR

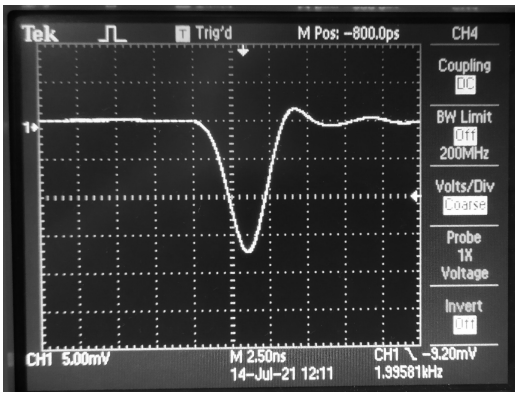


**(b)** UV-N2

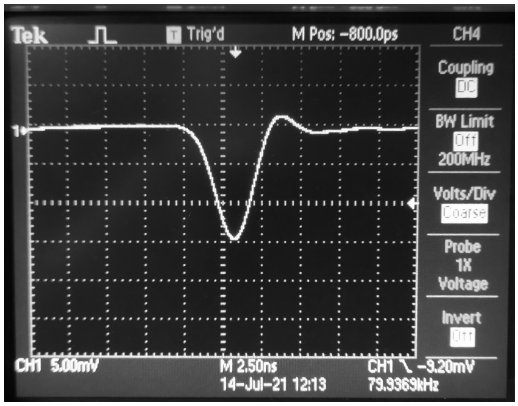


**(c)** UV-H2O

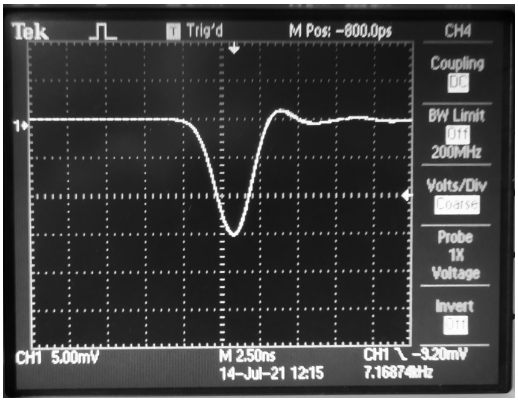


**(d)** VIS-AIR

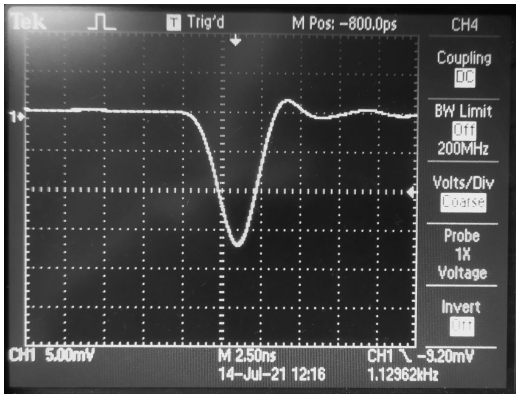


**(e)** VIS-N2

**Figure 6.19:** PMT pulses.

**Table 6.7:** Chosen HVs and thresholds

| Channel | HV (V) | threshold (level) |
|---|---|---|
| 1 | 800 | 7 |
| 2 | 820 | 8 |
| 3 | 830 | 8 |
| 4 | 820 | 8 |
| 5 | 840 | 8 |

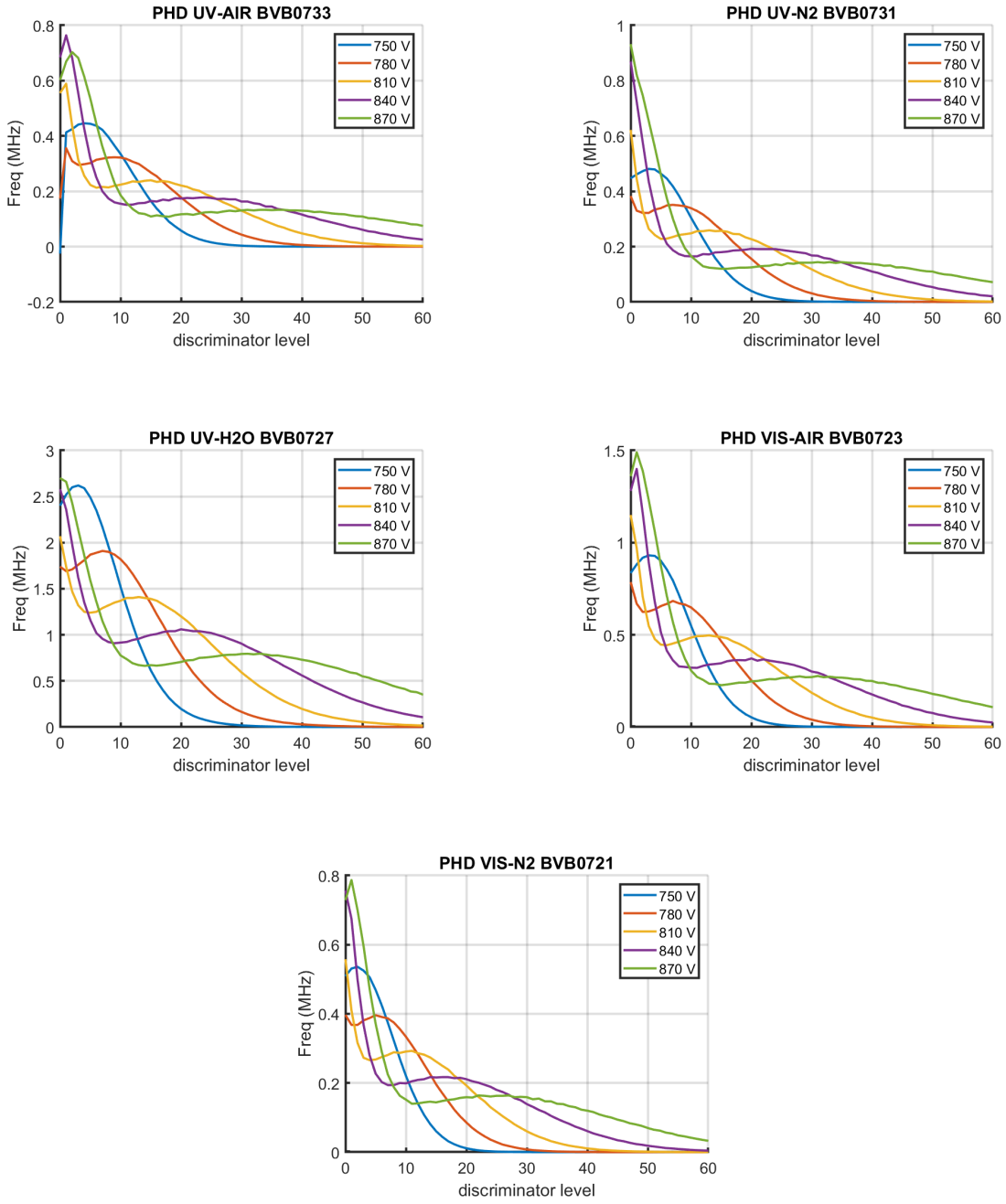


**Figure 6.20:** PMTs pulse height distributions. The curves are used to estimate the best high voltage and discriminator level.

### 6.2.3 Electronics

#### Relay Board

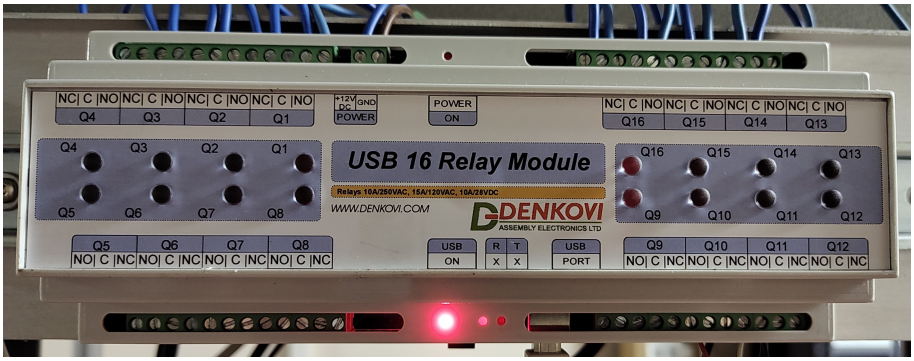


**Figure 6.21:** Relay module for power management.

The power supply for the lidar components is regulated using the USB 16 Relay Module, a product by Denkovi Assembly Electronics LTD [102]. The lidar software communicates with the relay board through the Denkovi Relay Command Line Tool, available for download from the Denkovi website.
The board allows us to switch on or off the trigger, the laser, the chiller, the Licel transient recorders and the PMTs. Furthermore it manage the dome opening/closing.

#### Licel's DAQ


**Figure 6.22:** Licel Ethernet Controllers. On top there are the transient recorders while on bottom there are the power supplies of the detectors.

The acquisition hardware is fabricated by Licel [103]. It consists of two ethernet controllers (ECs) in which several hardware units are mounted.
The first EC (located at the bottom of Figure 6.22) accommodates an APD power

supply and five PMT power supplies, each of which can be controlled either manually or remotely.
The second EC (shown at the top of Figure 6.22) hosts the transient recorders. One unit, the TR40, enables signal acquisition in both analog and photon counting modes, while the other four units, PR40, exclusively operate in photon counting mode.

For both acquisition modes, the range resolution is 3.75 m, and the memory depth is 32768 bins (equivalent to a range exceeding 120 km at the maximum resolution). Each transient recorder can accumulate up to 65534 acquisitions, and the TR40 can also store the sum of squared values, facilitating standard deviation computation. Analog signals are recorded by a 16-bit analog-to-digital converter, while photon counting involves detecting voltage pulses surpassing a chosen threshold, with a maximum count rate of 800 MHz.

### Trigger

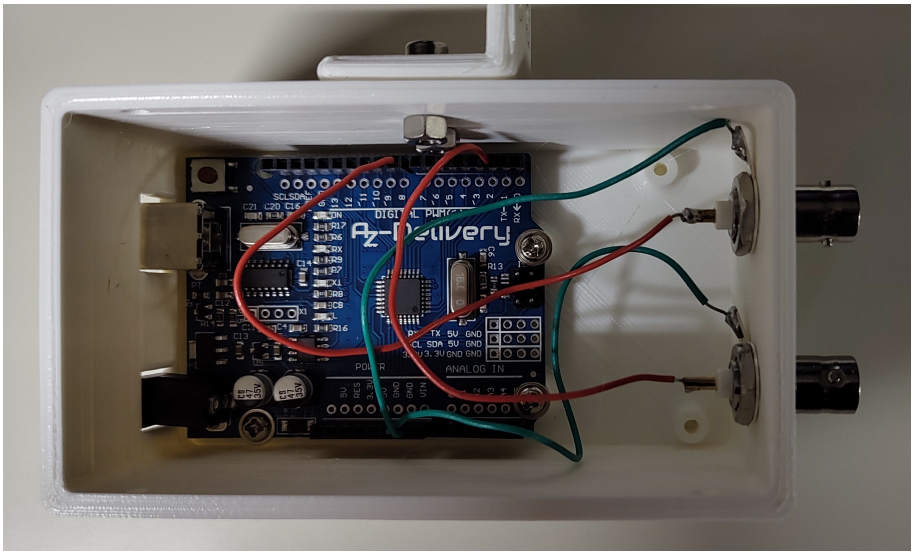

**Figure 6.23:** Trigger based on the Arduino Uno board. The case is 3d printed.

In our system the trigger is used to drive the laser diodes and the DAQ system. Once the diodes are triggered, the laser emission occurs about 205 µs later (Q-Switch delay) and we want start the signal acquisition before light is emitted. The specifications for the trigger signals are outlined in Table 6.8.

**Table 6.8:** Input trigger signals requirements

| Hardware | Amplitude | Min. Duration |
|---|---|---|
| Laser | 5-15 V | 100 µs |
| DAQ | 2.5-5 V | 150 ns |

The trigger hardware is based on the Arduino Uno board [104], as depicted in Figure 6.23. The original board uses a ceramic resonator which is sensitive to variations in temperature. Thus, I used a compatible board which mounts a crystal oscillator.

The output current, 40 mA, is high enough to trigger the laser diodes and the Licel transient recorders without requiring additional hardware. Specifically, the laser trigger is connected to pin 2 (PD2), while the Licel trigger is connected to pin 8 (PB0).
In order to obtain the required performance, the Arduino board is programmed handling the MCU registers.
The code is straightforward and is provided below:

```
int main() {

  DDRD = B00000100;
  DDRB = B00000001;
  PORTD = B00000000;
  PORTB = B00000000;

  while(true) {

    PORTD = B00000100;
    __builtin_avr_delay_cycles (1680);
    PORTD = B00000000;

    __builtin_avr_delay_cycles (960);

    PORTB = B00000001;
    __builtin_avr_delay_cycles (2);
    PORTB = B00000000;

    __builtin_avr_delay_cycles (157353);

  }
}
```

In the beginning, pins 2 and 8 are set as output and each pin of ports D and B is set as LOW. Then, in an endless loop, the laser trigger is set as HIGH and after 105 µs is set again as LOW. The pauses are done with the command:

```
__builtin_avr_delay_cycles (n);
```

where n is given by

$$n = \frac{delay}{62.5}$$

with *delay* the desired pause in ns and, since the board works at 16 MHz, each instruction takes 62.5 ns. Then, after 60 µs, the Licel DAQ is triggered. The last delay in the code sets the trigger frequency at 100 MHz. The signals are shown in Figure 6.24 with also the Pockels cell signal from the laser.
Using a photodiode (Thorlabs DET25K/M) we detected a light pulse 180 ns after the PC Sync (Figure 6.25).

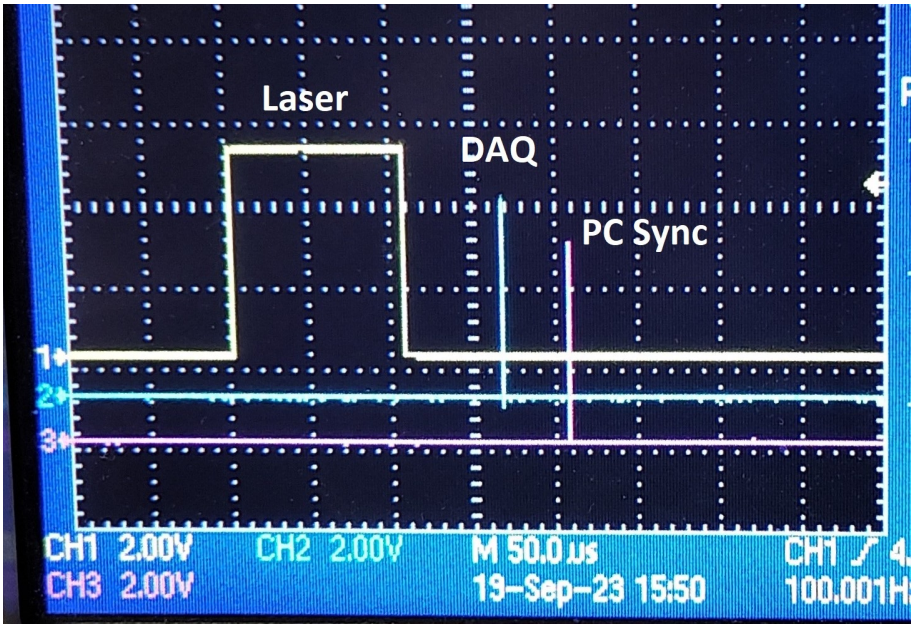


**Figure 6.24:** Trigger signals of laser diodes (yellow) and Licel DAQ (blue) with the PC Sync signal (pink).

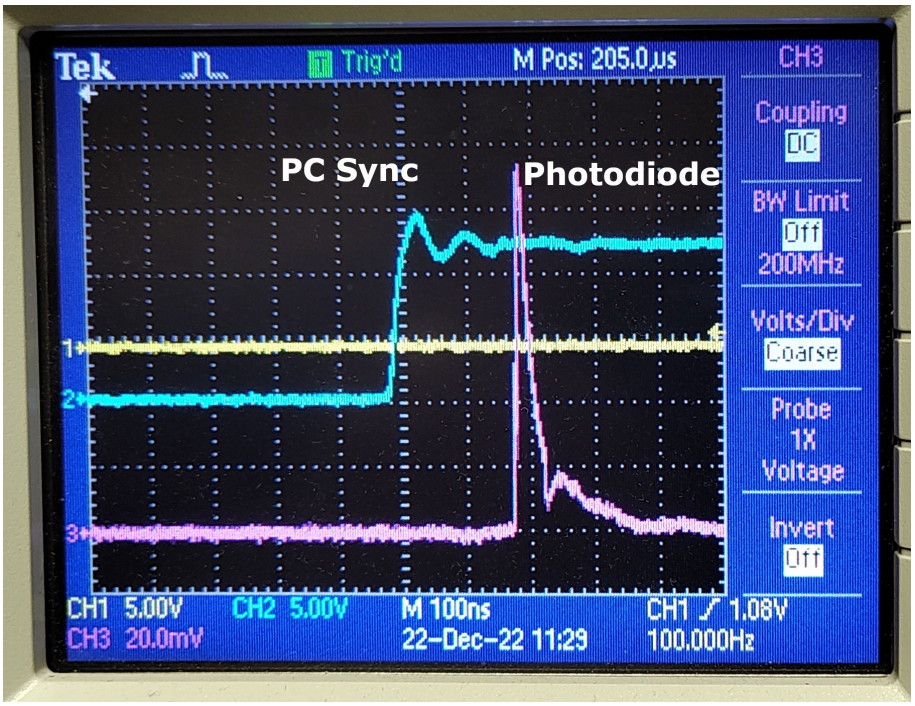


**Figure 6.25:** Delay between PC Sync (yellow) and photodiode signal (pink).

**Figure 6.26:** The rain sensor RG-9.

### Rain sensor

The rain sensor employed in the lidar system is the RG-9 model by Hydreon Corporation, as illustrated in Figure 6.26 [105]. Positioned adjacent to the dome, it serves to monitor rainfall conditions both before and during data acquisition. In the event of rain, the acquisition is automatically halted, and the dome is closed.

Supplementary meteorological data, including wind speed, relative humidity, atmospheric pressure, and temperature, is sourced from the Cetemps weather station [106], situated on the same building that accommodates the instrument.

## 6.3 Software

The control software has been developed with MATLAB [107]. As the laser software runs only under Windows we decided to control the whole system with a personal computer that uses this operating system.

The code is written using the object-oriented programming and it includes seven classes. The classes

- daqObj.m
- laserObj.m
- pmtObj.m
- powerObj.m
- rainObj.m
- weatherObj.m

contain the attributes and the methods which concern the Licel transient recorders, the laser, the PMTs high voltages, the relay board, the rain sensor, and the Cetemps weather station respectively. The classes **daqObj.m** and **pmtObj.m** talk directly with the Licel ethernet controllers without going through proprietary software (the acquisition is entirely managed within MATLAB). When instantiated, each class load the corresponding configuration file (an xml file). Once the software is initiated, it is possible to reload the configuration files if edited.
Furthermore there is the main class **lidarObj.m** that contains the methods for the data acquisition and data storage. These functions need the access to methods included in the other classes. In order to use the software will suffice to instanciate the main class, e.g. with **aq = lidarObj;**.

### 6.3.1 GUI

In order to simplify lidar operations, I realized a graphical user interface, a MATLAB app, called lidarAQ.mplapp (Figure 6.27). This interface allows the access to the main methods of the software modules. Launching the GUI from the MATLAB command window, i.e. with **app = lidarAQ;**, it is possible to access to the app workspace and launch the methods not implemented in the GUI. Each command must be preceeded by **app.**.

The GUI allows to control the power supplies, the dome aperture, the laser through the software SpitlightGUI, the PMTs' high voltages, and shows the current weather conditions. It also allows to start single signal acquisitions, while it is possible to start a set of multiple acquisitions with the command **app.aq.seq(n)**, where n is the length of the sequence.

### 6.3.2 Scripts and automatic observations

Given all the modules, it is possible to write MATLAB scripts for performing tests with several values of a given parameter or for performing automatic observations (the script is run at the desired hour with the Windows Task Scheduler).

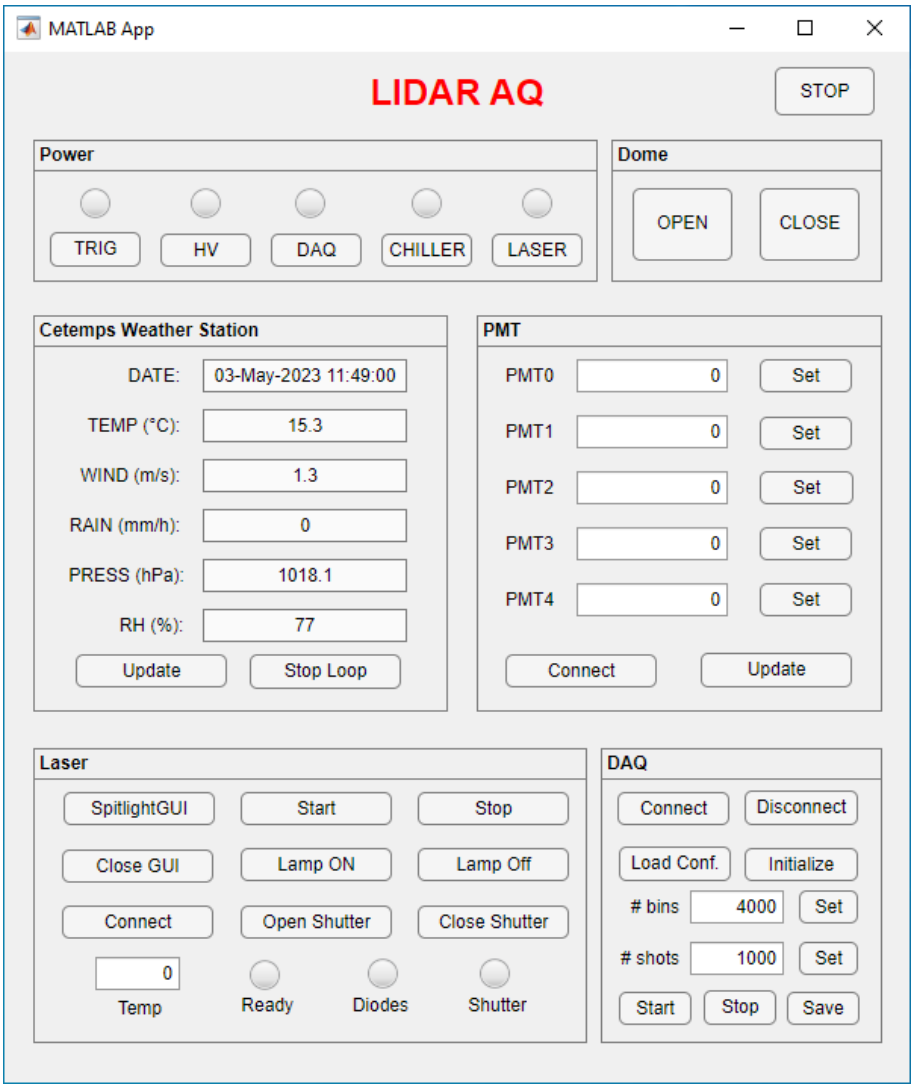


**Figure 6.27:** GUI.

A very usefull script is the one to perform the pulse height analysis of more than one photomultiplier tube at the same moment. This script provides substantial time savings in comparison to using the Licel software. Additional scripts are designed to conduct an observational sequence, adjusting a parameter, such as the discriminator level or the PMTs' high voltage, with each acquisition.

## 6.4 Quality Tests

In Europe, there is an international network of Lidar for aerosol study called EARLINET (European Aerosol Research Lidar Network) [108], integrated in 2011 within ACTRIS (Aerosols, Clouds, and Trace gases Research InfraStructure Network). The University of L'Aquila is a national facility of ACTRIS.
Within this network, there is currently no standard for hardware, and various groups use Lidar systems of diverse types. To ensure a minimum quality of measurements, a series of tests have been established to be conducted for each system (quality assurance, QA) [109].

### 6.4.1 Zero-Bin test

A trigger delay between the laser light emission and the zero range of the recorded signal can introduce large errors in the retrieved aerosol properties, especially in the lower range [109].
For our system the zero bin of each channel has been determined using a diffuse scattering target blocking the laser beam, a white paper, and a small aperture over the telescope. The measurements are reported in Figure 6.28, where the peaks show the range of the target.

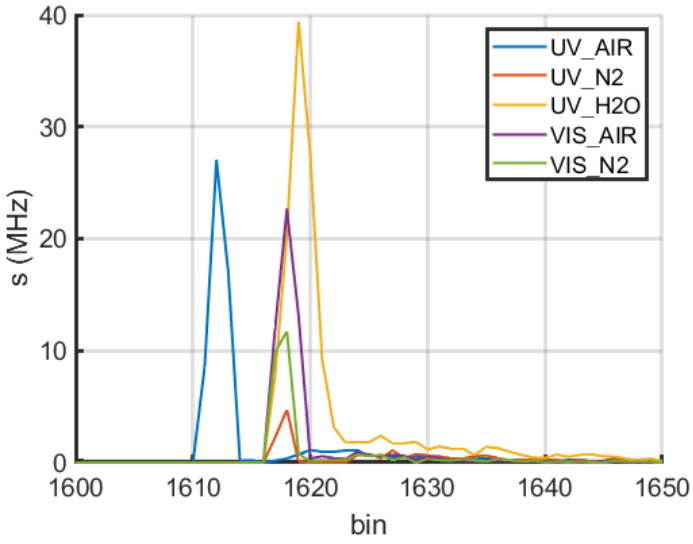


**Figure 6.28:** Results of the 0-bin test for the five channels. Peaks correspond to a range distance of 1 m.

### 6.4.2 Dark Measurements

The dark measurement is a lidar measurement with the telescope full covered so that no light from the atmosphere is collected. In the dark signals it is possible to observe distortions due to electromagnetic interference and therefore these latter can be subtracted from the actual lidar measurements. These disturbances mainly affect the analog signals.
As an example, in Figure 6.29 it is possible to observe the disturbances in the analog signal caused by the trigger signal of the DAQ and by the laser electronics.

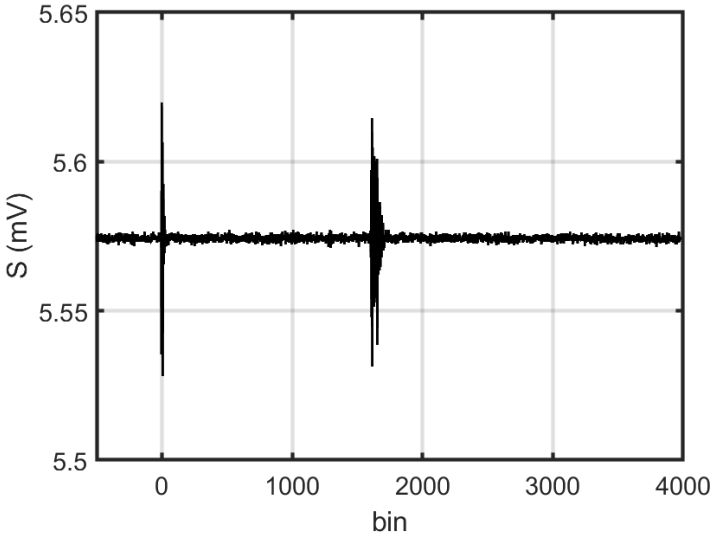


**Figure 6.29:** Electromagnetic disturbances due to DAQ trigger signal (bin 0) and to the laser Q-Switch (bin 1610).

### 6.4.3 Rayleigh Fit

The Rayleigh fit is a normalization of the range corrected signal to the attenuated molecular backscatter coefficient:

$$\beta_{\mathrm{m}}^{\mathrm{attn}}(R, R_0) = \beta_{\mathrm{m}}(R) exp\left\{ -2 \int_{R_0}^{R} \alpha_{\mathrm{m}}(R')dR' \right\}. \tag{6.5}$$

Normalization is performed in a range interval where no aerosols are supposed to be. $R_0$ is the reference range at the middle of a range interval $[R_{\mathrm{min}}, R_{\mathrm{max}}]$ where it is possible to assume the absence of aerosols, and $\beta_{\mathrm{m}}$ and $\alpha_{\mathrm{m}}$ should be obtained from a local radiosonde. The normalized range corrected signal is thus

$$R^2 P^{\mathrm{norm}}(R, R_0) = R^2 P(R) \frac{\sum_{R_{\mathrm{min}}}^{R_{\mathrm{max}}} \beta_{\mathrm{m}}^{\mathrm{attn}}(R, R_0)}{\sum_{R_{\mathrm{min}}}^{R_{\mathrm{max}}} R^2 P(R)}. \tag{6.6}$$

Deviations from the computed Rayleigh signals can reveal several problems, in particular, they can highlight distortions of lidar signals for large ranges, where the number of the detected backscattered photons is small and the presence of aerosols is negligible. Unfortunately, to perform this test, few hours of stable atmosphere could be necessary, and founding a suitable night for the Rayleigh fit test may require a long time.
The Rayleigh fits for the elastic channels UV-AIR (355 nm) and VIS-AIR (532 nm), are shown in Figure 6.30 and Figure 6.31 respectively. The data acquired on November 15, 2023 (Figure 6.43), are utilized, amounting to a total acquisition time of 134 minutes. Lidar signals are binned to 60 m and are normalized between 7 km and 8 km. Since radiosonde data were not available, the molecular component is computed from monthly averaged GDAS data. Deviations of the Rayleigh fits from the computed Rayleigh signals are below five percent for heights up to 12 km.

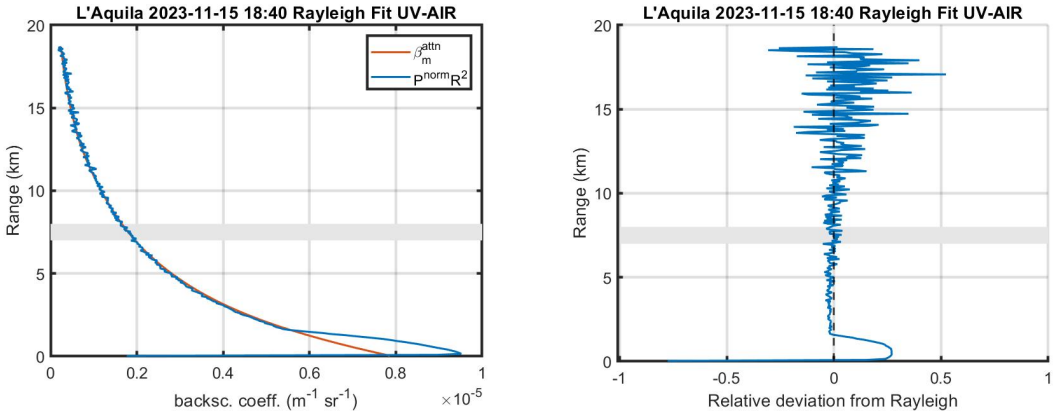


**Figure 6.30:** Rayleigh fit of the elastic channel UV-AIR (355 nm). In the left panel the Rayleigh fit $P^{\mathrm{norm}}R^2$ (blue) and the molecular attenuated backscatter coefficient $\beta_{\mathrm{m}}^{\mathrm{attn}}$ (red) are reported, while the residuals of the Rayleigh fit are shown in the right panel. The grey area indicates the region where the normalization has been performed [7 km - 8 km]. The lidar signal is binned into 16 bins with an overall width of 60 m.

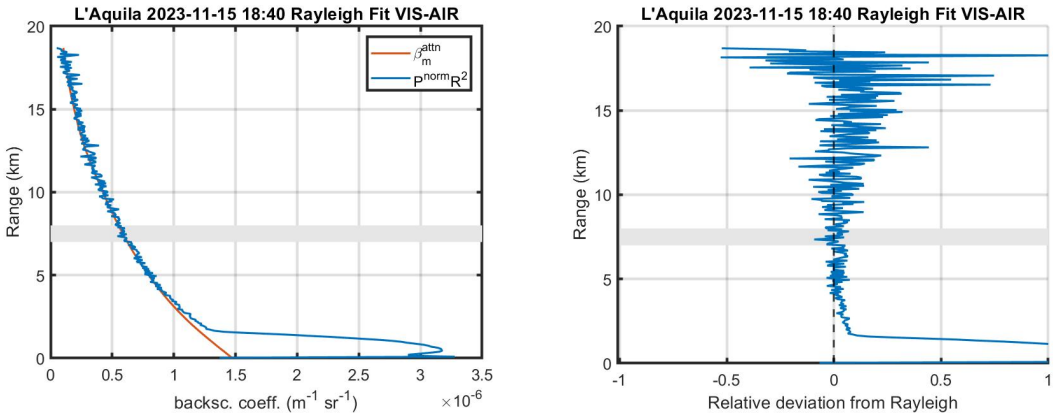


**Figure 6.31:** Rayleigh fit of the elastic channel VIS-AIR (532 nm). In the left panel the Rayleigh fit $P^{\mathrm{norm}}R^2$ (blue) and the molecular attenuated backscatter coefficient $\beta_{\mathrm{m}}^{\mathrm{attn}}$ (red) are reported, while the residuals of the Rayleigh fit are shown in the right panel. The grey area indicates the region where the normalization has been performed [7 km - 8 km]. The lidar signal is binned into 16 bins with an overall width of 60 m.

### 6.4.4 Telecover Test

The telecover test entails examining signal variations over short distances by obstructing different sections of the telescope aperture. In an ideal Lidar, differences in normalized signals are solely due to the overlap function. In a real Lidar, this test can highlight not only the minimum full overlap distance but also any optical misalignments. The test is based on the principle that photons collected from different sectors of the telescope mirror must produce a signal with the same range dependence. We therefore expect that in the region of full overlap, the signals from the telecover test, once normalized, will be similar.

There are three types of telecover tests: quadrant-test, in-out-test, and octant-test. The results of the quadrant-test are presented below. Four acquisitions were performed, each covering a different quadrant of the telescope, plus a fifth acquisition similar to the first to highlight any atmospheric variability.
In the following Figures 6.32, 6.33, 6.34, 6.35 and 6.36, normalized and smoothed range corrected signals are depicted on the left, and their relative deviations from the mean are shown on the right.
The relative differences are below 10% for ranges higher than 250 m for the channels UV-AIR, UV-N2, UV-H2O. The theoretical minimum distance of full overlap [110, 12] is instead of the order of 50 m, Figure 6.37 (the same result was obtained through simulations using Zemax, Figure 6.38). This difference could be attributed to the modulation introduced by the fiber bundle. For the channel VIS-AIR the telecover test shows a minimum range of full overlap of 400 m, 1000 m for the VIS-N2 channel. For all channels, observing the two Q1 curves (same quadrant of the telescope aperture left open but acquired 20 minutes apart), there is no significant atmospheric variability noticed. Therefore, the difference may be due to a misalignment issue of the laser beam with respect to the telescope's optical axis and to a modulation of the optical fiber.
Further observations, possibly of longer duration, are needed to understand the nature of this difference in the minimum distance of full overlap and to improve upon it. A better alignment of the laser beam and a defocusing of the fiber bundle could be necessary.

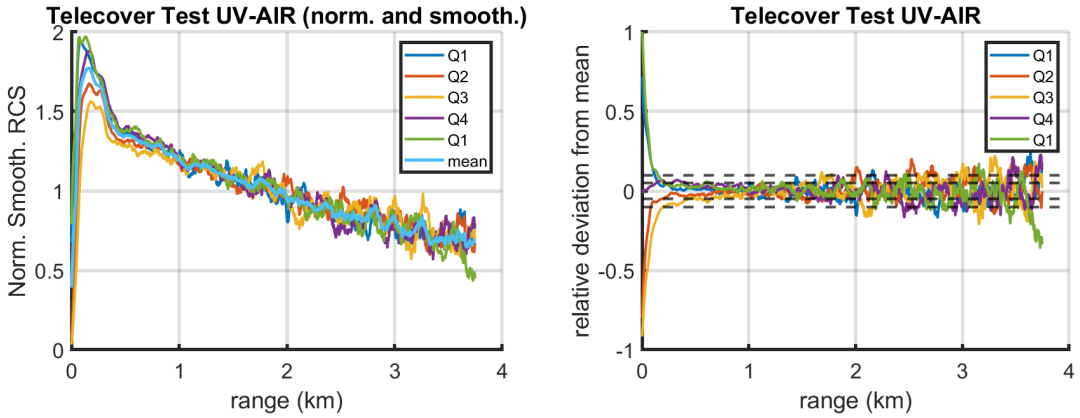


**Figure 6.32:** Quadrant telecover test of channel UV-AIR. The minimum range of full overlap is 250 m.

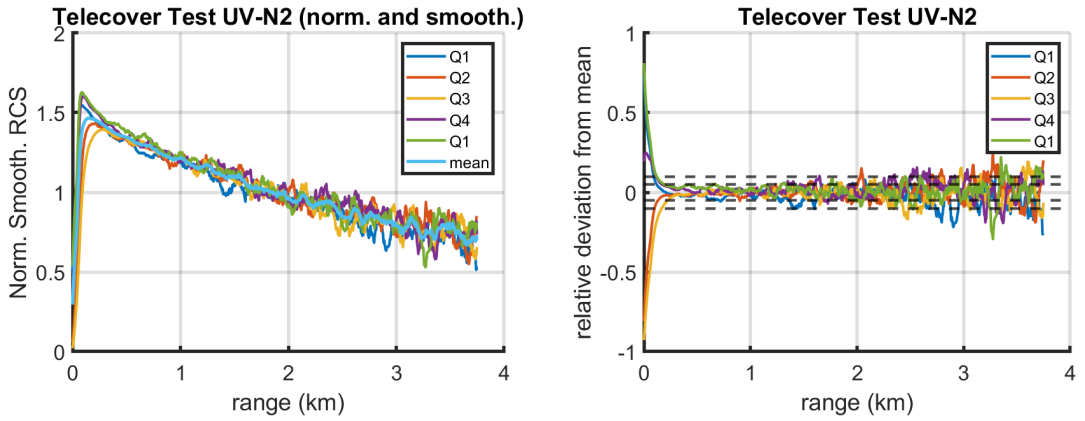


**Figure 6.33:** Quadrant telecover test of channel UV-N2. The minimum range of full overlap is 250 m.

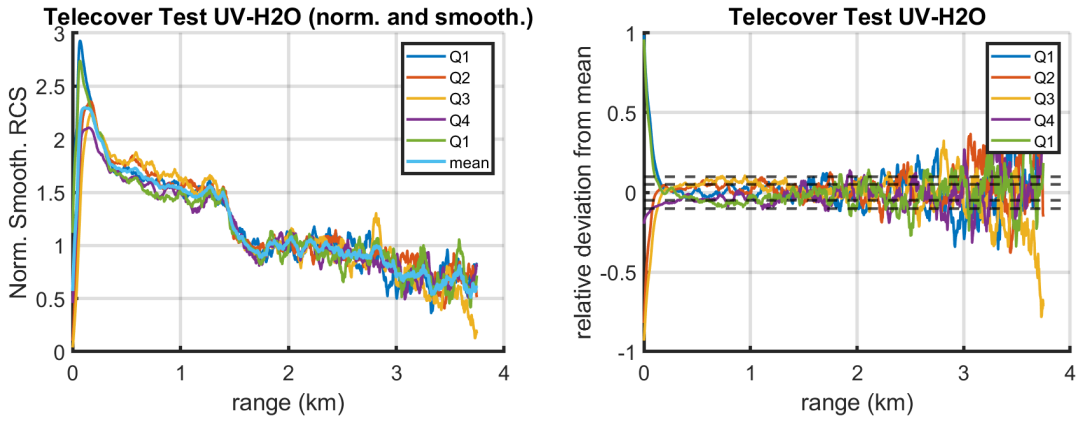


**Figure 6.34:** Quadrant telecover test of channel UV-H2O. The minimum range of full overlap is between 200 m and 300 m.

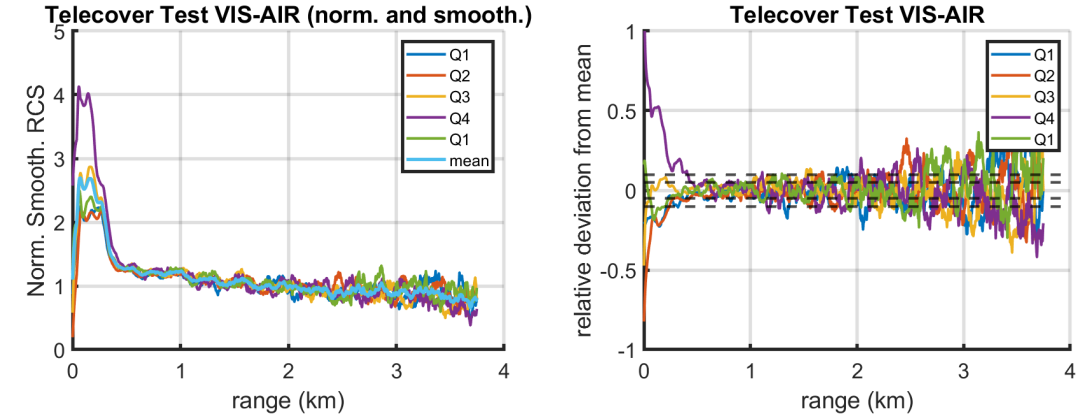


**Figure 6.35:** Quadrant telecover test of channel VIS-AIR. The minimum range of full overlap is 400 m.

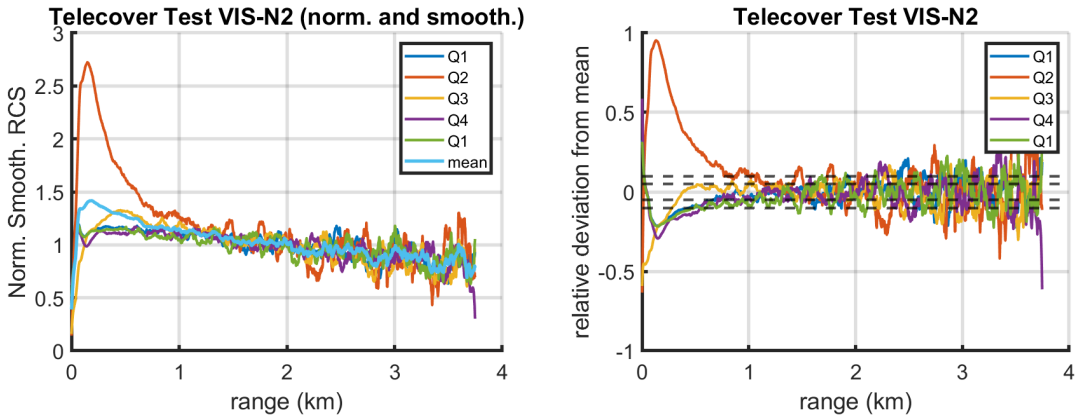


**Figure 6.36:** Quadrant telecover test of channel VIS-N2. The minimum range of full overlap is 1000 m.

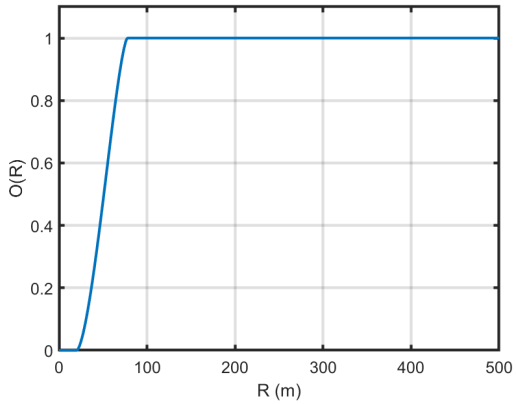


**Figure 6.37:** Analytical overlap function computed as in [110] with the laser beam axis parallel to the telescope axis.

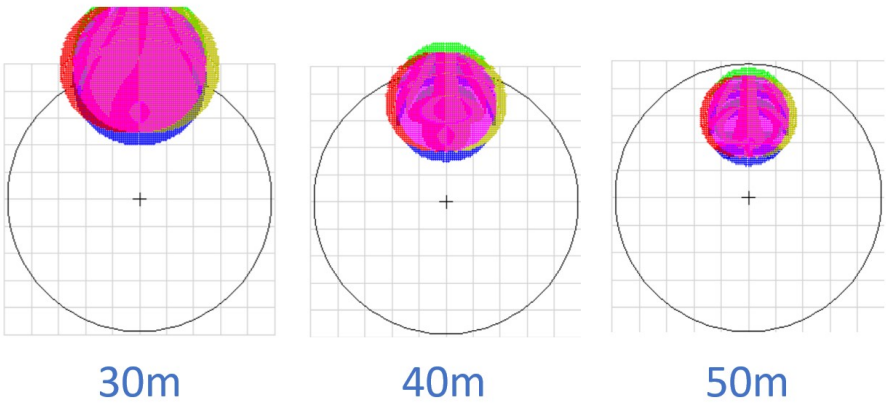


**Figure 6.38:** Fiber bundle input with the backscattered laser beam entering into the telescope field of view as a function of range. Simulation with Zemax.

## 6.5 Observations

In this section, some lidar observations conducted during the instrument testing are reported. A picture of the data acquisition phase is shown in Figure 6.39, where it is possible to observe the emission of the green laser beam from the lidar laboratory.

**Figure 6.39:** Lidar data acquisition. It is possible to observe the green laser beam.

### 6.5.1 Example of aerosol optical properties retrieval

In Figure 6.40, an observation from October 4, 2023 is presented. The signals labeled UV-AIR (panel 6.40a), UV-N2 (panel 6.40c), and UVH2O (panel 6.40e) result from the summation of four acquisitions of 5 minutes each, with 30,000 laser shots per acquisition. The original lidar signals, acquired with a vertical resolution of 3.75 m, are binned to an overall bin of 15 m length. The vertical resolution is further reduced through a low-pass filter applied concurrently with the first derivative during the calculation of the aerosol extinction coefficient. The same low-pass filter is then applied to the aerosol backscatter coefficient before the lidar ratio calculation (as illustrated in Section 4.7). A Savitzky–Golay filter [111] of the second order is used for computing the numerical first derivative and for signal smoothing.
On the right side of the figure, from top to bottom, the aerosol extinction coefficient (panel 6.40b), backscatter coefficient (panel 6.40d), and lidar ratio (panel 6.40f) at 355 nm are displayed. The red points represent data for which the relative uncertainties, obtained through standard error propagation, are less than 50%. The lidar ratio obtained in the lower atmosphere is consistent with the presence of urban aerosols.

### 6.5.2 Examples of atmospheric time evolution

Figure 6.41 shows the time sequence of the range corrected signals of the channels, from left to right, UV-AIR at 355 nm, VIS-AIR at 532 nm, and UV-H2O at 407 nm, acquired on October 5, 2023. It is the result of 30 acquisitions of one minute (6000 laser shots), and it shows the evolution of the planetary boundary layer and of high altitute clouds.
In Figure 6.42 the time sequence acquired on November 9, 2023 are reported (same channels of the previous figure, but in log scale). The sequence consists of 162 lidar acquisitions of twenty seconds (2000 laser shots). It is possible to observe the presence and the evolution of a cloud at an altitude of 4 km, followed by a low-level cloud (2 km above ground level).
In Figure 6.43, instead, a sequence of measurements from November 15, 2023 is shown. It consists of 67 acquisitions of two minutes each (1200 laser shots), totaling 2 hours and 14 minutes of observation. In this time interval no clouds or aerosol layers are present, and the evolution of the planetary boundary layer is observable, which lowers as the night progresses.

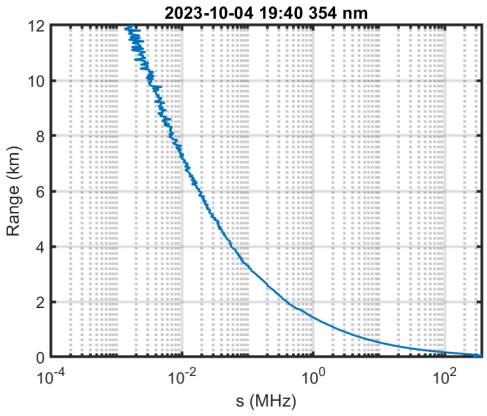


**(a)** UV-AIR signal @ 355 nm

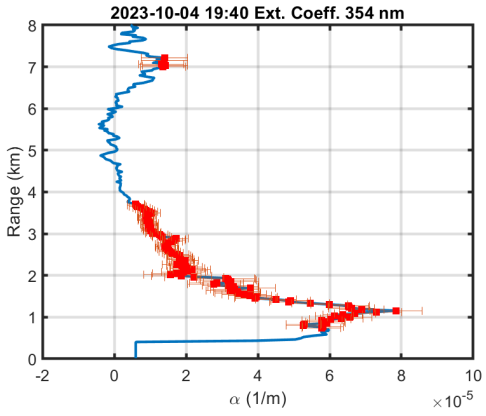


**(b)** Aerosol extinction coefficient at 355 nm

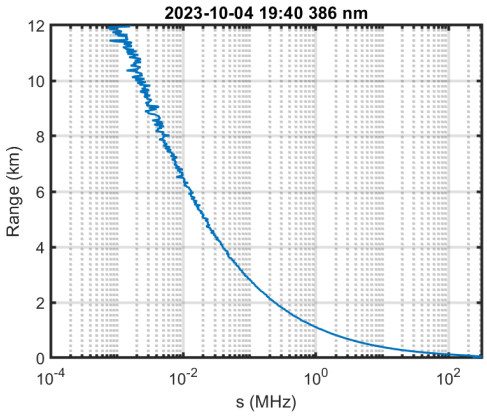


**(c)** UV-N2 signal @ 386 nm

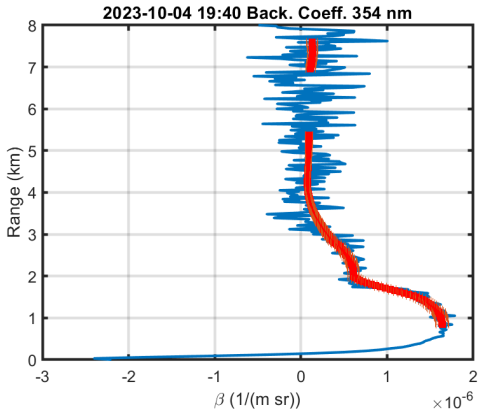


**(d)** Aerosol backsc. coefficient at 355 nm

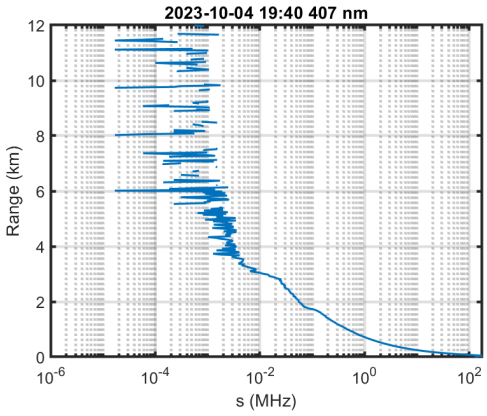


**(e)** UV-H2O signal @ 407 nm

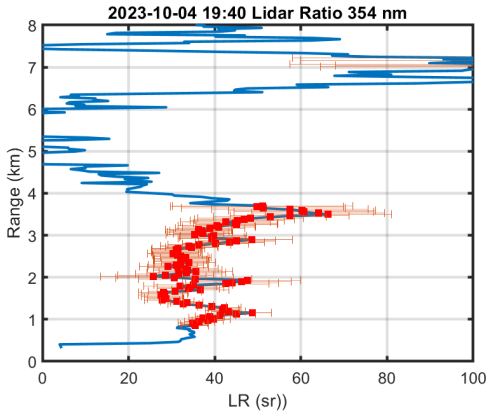


**(f)** Aerosol lidar ratio at 355 nm

**Figure 6.40:** Lidar observation from October 4, 2023. Total acquisition time 20 minutes for 120000 laser shots. Panels (a), (c), and (e) show the lidar signals UV-AIR at 355 nm, UV-N2 at 386 nm, and UV-H2O at 407 nm, respectively. Panels (b), (d), and (f) show the aerosol extinction coefficient, the aerosol backscatter coefficient, and the lidar ratio (all at 355 nm), respectively. The red points represent data for which the relative uncertainties are less than 50%.

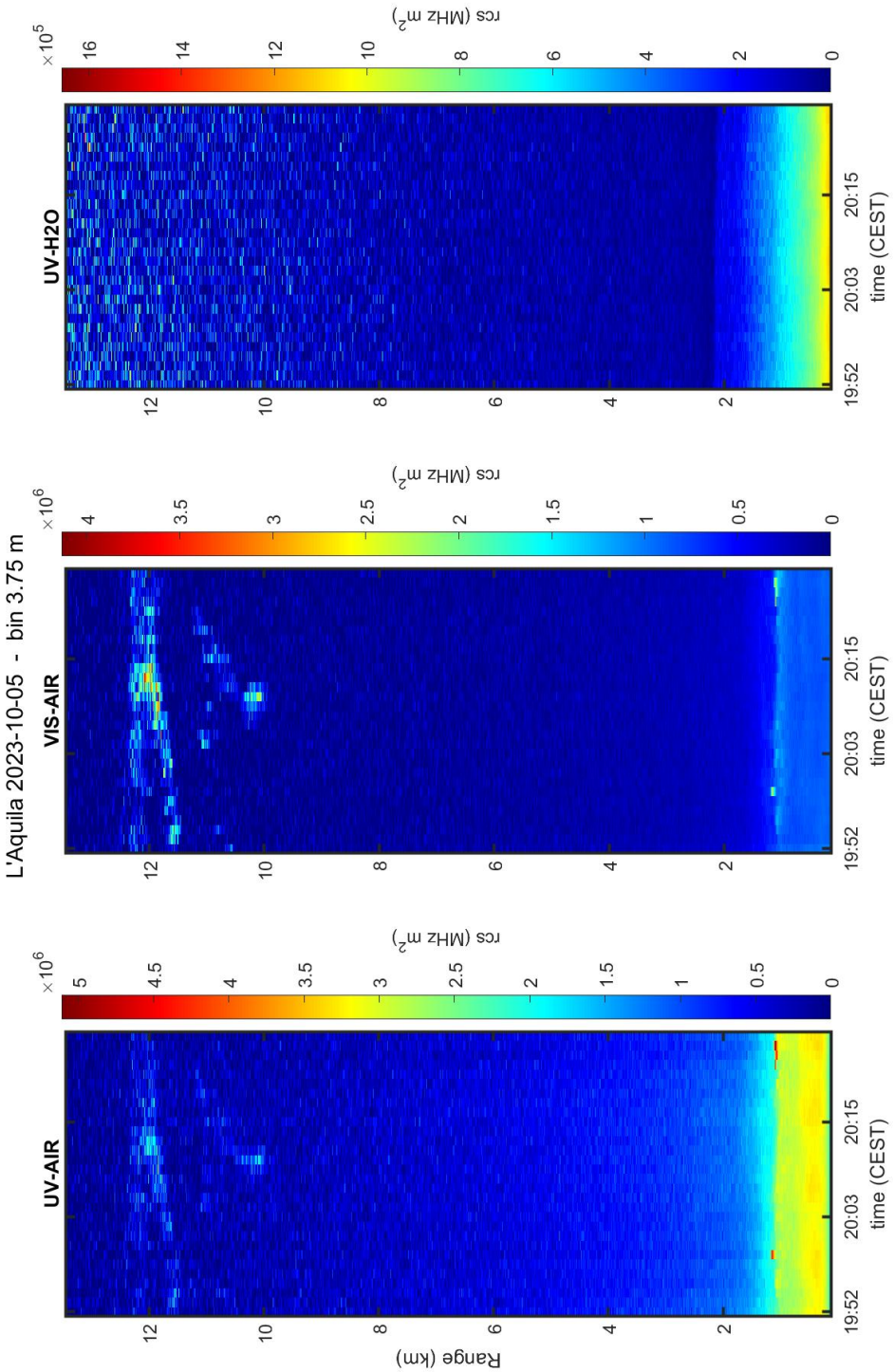


**Figure 6.41:** Observation on October 5, 2023. Sequence of 30 one-minute acquisitions (6000 laser shots). The left panel shows the range corrected elastic signal at 355 nm, the middle panel the range corrected signal at 532 nm, and the right panel the range corrected raman signal of the water vapor at 407 nm.

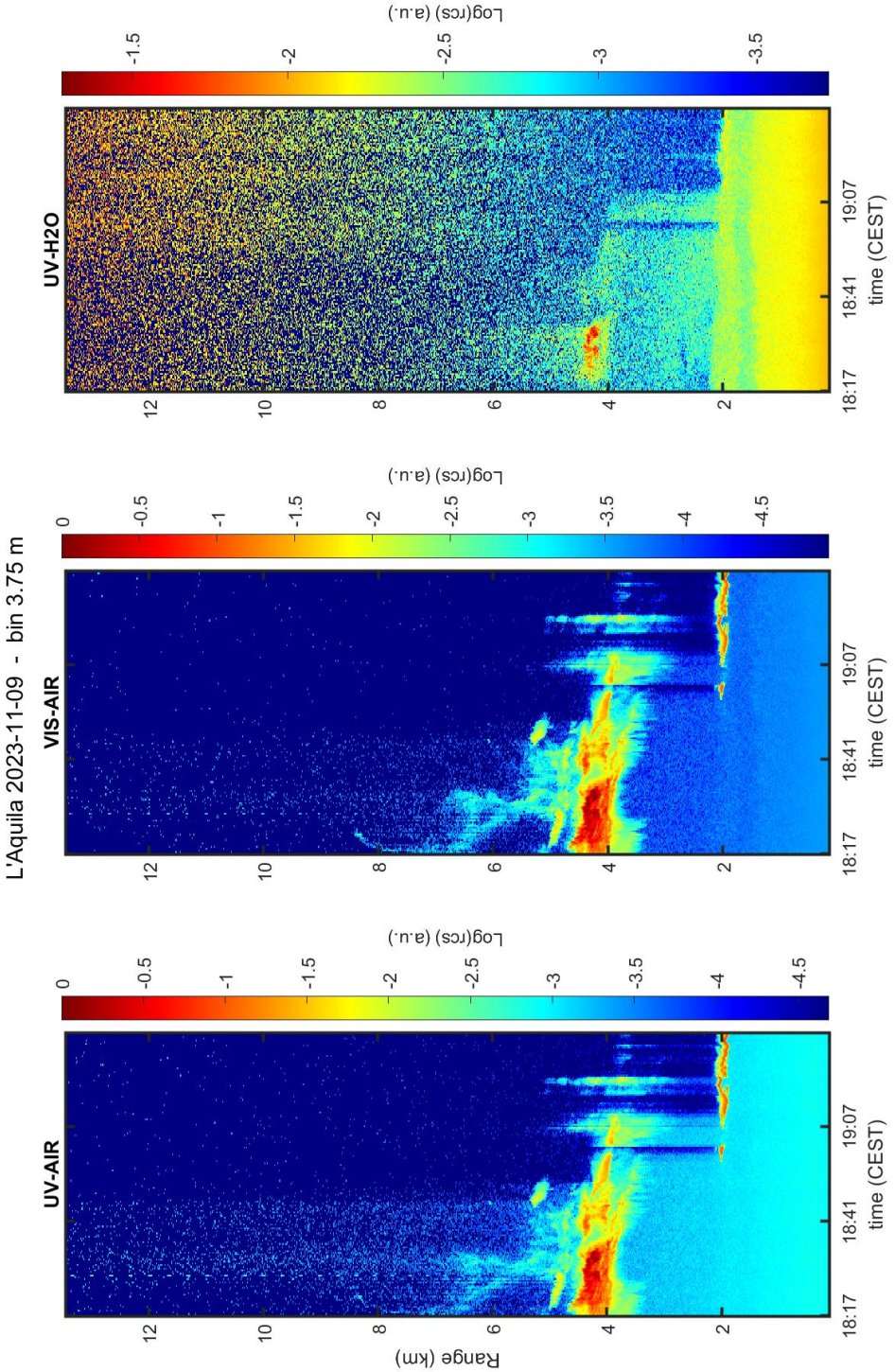


**Figure 6.42:** Observation on November 9, 2023. Sequence of 162 acquisitions of 20 seconds (2000 laser shots). The left panel shows the range corrected elastic signal at 355 nm, the middle panel the range corrected signal at 532 nm, and the right panel the range corrected raman signal of the water vapor at 407 nm. In this F the log scale for the range corrected signal is used.

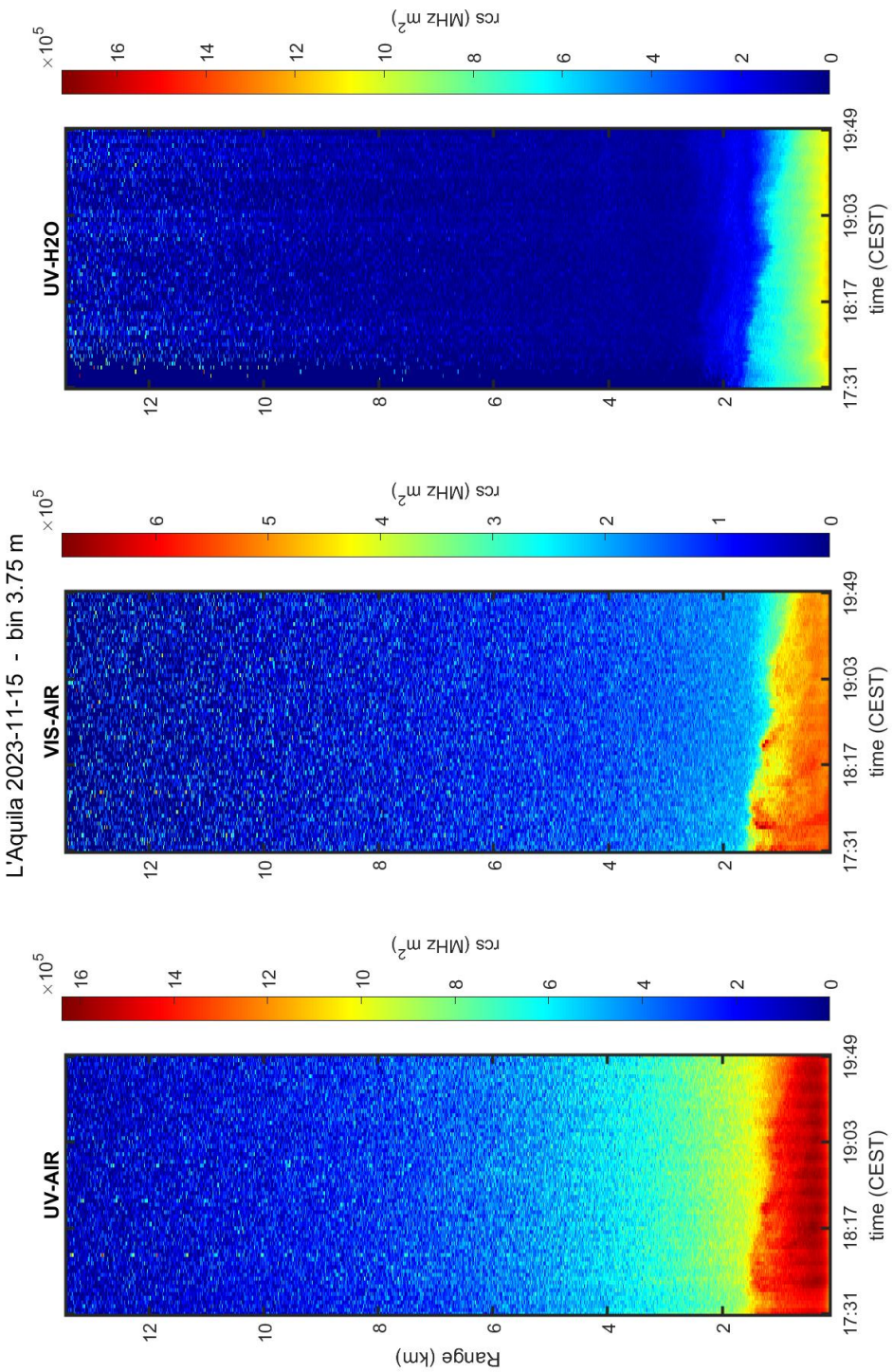


**Figure 6.43:** Observation on November 15, 2023. Sequence of 67 acquisitions of 120 seconds (12000 laser shots). The left panel shows the range corrected elastic signal at 355 nm, the middle panel the range corrected signal at 532 nm, and the right panel the range corrected raman signal of the water vapor at 407 nm.

# Chapter 7

# Conclusions

Although the discovery of cosmic rays occurred over a century ago, many questions regarding UHECRs remain unanswered. Specifically, efforts are underway to enhance our understanding of particle acceleration mechanisms at higher energies, to determine their composition, and to elucidate the observed features in their spectrum and arrival directions.
The study of cosmic rays with energies exceeding $10^{14}$ eV occurs through the observation of extensive air showers (EAS) that develop following interactions with molecules in the atmosphere. At the Pierre Auger Observatory, these EAS are detected using both the Surface Detector (SD) and the Fluorescence Detector (FD). To obtain accurate information about the nature and energy of the primary cosmic ray from fluorescence light measurements, it is crucial to understand the light extinction caused by aerosols.

My doctoral activity primarily focused on developing a lidar system for monitoring atmospheric aerosols. Specifically, I was involved in the hardware development of the system, as well as the instrument control software and signal analysis software. The unique aspect of the system is the use of a bundle of optical fibers that splits the light collected by the telescope into five channels (two elastic and three Raman), simplifying the receiver part. No alignment of beam splitters and interference filters is required anymore, and in many cases system updates are also facilitated. One of the aims of this work is to validate this solution. Various tests and initial observations demonstrate the system's potential, but also highlight some issues (such as in the telecover test) that we hope to resolve in the near future. This lidar will be used for aerosol monitoring at the L'Aquila site, and will also serve as a testbed for developing new systems tailored for cosmic ray observatories. To finalize the integration into ACTRIS, the system will undergo an update, including the addition of an infrared elastic channel and two additional channels for studying the aerosol depolarization ratio.

As a member of the Pierre Auger collaboration, I have been involved in signal analysis for the Raman lidar located at the Observatory's central laser facility. The system has been collecting data since September 2013, revealing atmospheric aerosols above the observatory site.
Since we are interested in the so-called clear nights, the lidar signals have been filtered for clouds, high aerosol content and bad measurements. Out of 5433 initial acquisitions, 675 have survived. The retrieved vertical profiles of the aerosol optical depth (VAOD) and backscatter coefficient show a seasonal dependence, with lower

values during the winter months. The average value of the VAOD at the reference height above ground of 4.5 km is $0.040 \pm 0.019$. The VAOD shape can be described with both a 2-parameter model or a 3-parameter model with the latter having better performance in describing the aerosol distribution above the observatory. The Raman lidar data can be used as a cross-check for the other techniques used within the observatory. In a recent work, these data were useful to upgrade the systematic uncertainty in shower energy and depth of the maximum size estimation attributable to aerosols.

For the Auger collaboration I also worked on the characterization of the new Quantel laser intended for the central laser facility and in participated in FD and SD measurement shifts.

# Appendix A

# Elastic-Backscatter Lidar

In the case where only the elastic signal is available, to be able to invert the lidar equation (Eq. 4.10) and obtain the aerosol extinction coefficient or the aerosol backscatter coefficient, it is necessary to make assumptions about their relationship (for example about the aerosol lidar ratio $L_{\text{aer}}$). Under typical tropospheric condition, it is preferable to retrieve the aerosol backscatter coefficient [112]. This method is often referred to as Klett's method [113, 114] or Klett-Fernald method [115].
Starting from the elastic lidar equation, Eq 4.10, the range corrected signal $S(R) = R^2P(R)$ can be written as

$$S(R) = P_0\eta\left[\beta_{\text{aer}}(R) + \beta_{\text{mol}}(R)\right] exp\left[-2\int_0^R [\alpha_{\text{aer}}(R') + \alpha_{\text{mol}}(R')]dR'\right]. \tag{A.1}$$

Introducing the term

$$Y(R) = L_{\text{aer}}\left[\beta_{\text{aer}}(R) + \beta_{\text{mol}}(R)\right], \tag{A.2}$$

and using

$$L_{\text{aer}}(R) = \frac{\alpha_{\text{aer}}(R)}{\beta_{\text{aer}}(R)} \quad \text{and} \quad L_{\text{mol}} = \frac{\alpha_{\text{mol}}(R)}{\beta_{\text{mol}}(R)},$$

we can write

$$\begin{aligned} S(R)L_{\text{aer}}(R)exp\left\{-2\int_0^R [L_{\text{aer}}(R') - L_{\text{mol}}]\beta_{\text{mol}}(R')dR'\right\} = \\ = P_0\eta Y(R)exp\left[-2\int_0^R Y(R')dR'\right]. \end{aligned} \tag{A.3}$$

Taking the logarithms and differentiating with respect to $R$, we obtain

$$\begin{aligned} \frac{d\ln\left(S(R)L_{\text{aer}}(R)exp\left\{-2\int_0^R [L_{\text{aer}}(R') - L_{\text{mol}}]\beta_{\text{mol}}(R')dR'\right\}\right)}{dR} = \\ = P_0\eta Y(R)exp\left[-2\int_0^R Y(R')dR'\right]. \end{aligned} \tag{A.4}$$

This equation can be integrated using the boundary condition

$$Y(R_0) = L_{\text{aer}}(R_0)\left[\beta_{\text{aer}}(R_0) + \beta_{\text{mol}}(R_0)\right] \tag{A.5}$$

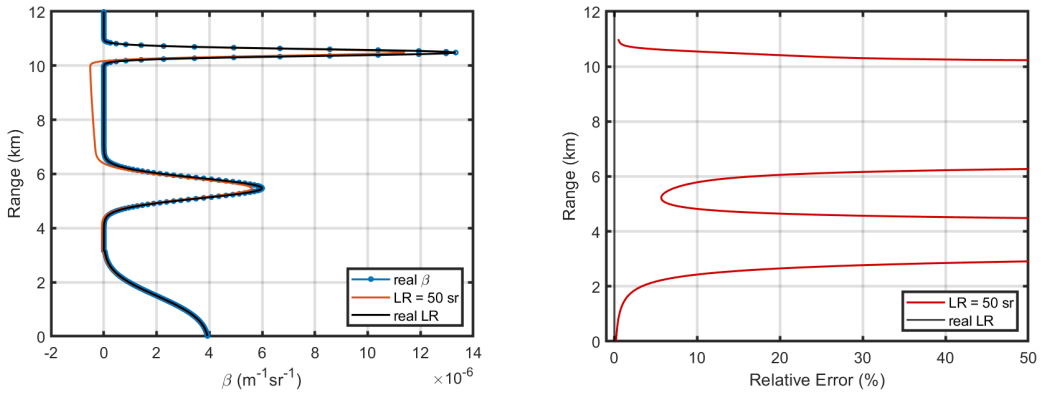


**Figure A.1:** Effects of the choice of the aerosol lidar ratio on the retrieval of the aerosol backscatter coefficient from the simulated lidar signals of Figure 4.2. The real $\beta_{\text{aer}}$ (dotted line) is compared with the retrieved ones using a constant lidar ratio of 50 sr (red line) and the real lidar ratio (black line).

and we obtain

$$\beta_{\text{aer}}(R) + \beta_{\text{mol}}(R) = \\ = \frac{S(R) exp\left\{-2\int_{R_0}^{R}[L_{\text{aer}}(R') - L_{\text{mol}}]\beta_{\text{mol}}(R')dR'\right\}}{\frac{S(R_0)}{\beta_{\text{aer}}(R_0)+\beta_{\text{mol}}(R_0)} - 2\int_{R_0}^{R} L_{\text{aer}}(R')S(R')T_\beta(R', R_0)dR'}, \tag{A.6}$$

with

$$T_\beta(R', R_0) = exp\left\{-2\int_{R_0}^{R'}\left[L_{\text{aer}}(R'') - L_{\text{mol}}\right]\beta_{\text{mol}}(R'')dR''\right\}. \tag{A.7}$$

The reference range $R_0$ is usually chosen in an aerosol free region. To assure numerical stability, the integrals in Eq. A.6 must be performed in the backward direction, i.e. starting form $R_0$ in the far end ($R < R_0$) [113]. The term $Y(R)$, Eq. A.2, can also be defined in terms of the extinction coefficients [116]. With this definition, an analog expression for the aerosol extinction coefficient can be obtained:

$$\alpha_{\text{aer}}(R) + \frac{L_{\text{aer}}(R)}{L_{\text{mol}}}\alpha_{\text{mol}}(R) = \\ = \frac{S(R)L_{\text{aer}}(R) exp\left\{-2\int_{0}^{R}\left[\frac{L_{\text{aer}}(R')}{L_{\text{mol}}} - 1\right]\alpha_{\text{mol}}(R')dR'\right\}}{\frac{S(R_0)L_{\text{aer}}(R_0)}{\alpha_{\text{aer}}(R_0)+\frac{L_{\text{aer}}(R')}{L_{\text{mol}}}\alpha_{\text{mol}}(R_0)} - 2\int_{R_0}^{R} L_{\text{aer}}(R')S(R')T_\alpha(R', R_0)dR'}, \tag{A.8}$$

with

$$T_\alpha(R', R_0) = exp\left\{-2\int_{R_0}^{R'}\left[\frac{L_{\text{aer}}(R'')}{L_{\text{mol}}} - 1\right]\alpha_{\text{mol}}(R'')dR''\right\}. \tag{A.9}$$

For highly turbid atmosphere, this equation is less sensitive to the value of the aerosol lidar ratio [115] and it is preferred to Eq. A.6.

The lidar ratio can be assumed constant with range or spatially variable. In this work the Klett's method is used for an estimation of the overlap function of Auger Raman lidar, and the real range dependent lidar ratio can be used. The effects of the aerosol lidar ratio on the backscatter coefficient retrieval is shown in Figure A.1. When aerosols are negligible, $\beta_{\text{aer}} \approx 0$, the relative deviation from the real value rises fast.

# Appendix B

# Temperature dependent lidar equations

Since the line strengths in Raman scattering are temperature dependent, depending on the passband of the filters used in the lidar system, the intensity of the recorded signal can result temperature sensitive.
In the case of the Rayleigh-Mie scattering the signal consists of an elastically scattered signal along with inelastic pure rotational lines which are due mainly to nitrogen and oxygen molecules. The filter passband may then include several of these rotational Raman lines and at atmospheric temperatures there is a significant probability that some rotational states of the molecules will be excited. The population of these states varies with temperature and this behaviour can be imparted to the backscattered signal.
On the other hand, regarding the case of vibrational Raman scattering, atmospheric molecules are essentially in their vibrational ground state. However, if the filter selects only a fraction of the roto-vibrational band, the transmitted signal will be temperature dependent as well.

In order to investigate the system performance we need to evaluate the temperature dependence of the Rayleigh-Mie and Raman lidar equations. A derivation of these temperature dependent equations was done in [117].
If $\Delta\lambda$ is the passband of the corresponding filter, the Rayleigh-Mie lidar equation can be written as

$$P(\lambda_{\mathrm{L}}, \Delta\lambda_{\mathrm{R}}, R) = P_0 \frac{c\tau}{2} A \frac{O(z)}{R^2} \Bigg\{ N_X(R) \int_{\Delta\lambda_{\mathrm{R}}} [d\sigma_X(\lambda', \pi, T[R])/d\Omega] \eta(\lambda') d\lambda' + \\ + \beta_{\mathrm{aer}}(\lambda_{\mathrm{L}}, R) \eta(\lambda_{\mathrm{L}}) \Bigg\} \times exp\left[ -2 \int_0^R \alpha(R', \lambda_{\mathrm{L}}) dR' \right], \tag{B.1}$$

It should be noted that the Mie signal due to aerosols is much narrower than the spectral width of signal due to molecules.
In the same way, the Raman lidar equation becomes

$$P(\lambda_{\mathrm{L}}, \Delta\lambda_X, R) = P_0 \frac{c\tau}{2} A \frac{O(R)}{R^2} N_X(R) \int_{\Delta\lambda_X} [d\sigma_X(\lambda', \pi, T[R])/d\Omega] \eta(\lambda') d\lambda' \\ \times exp\left[ - \int_0^R \alpha(R', \lambda_{\mathrm{L}}) dR' \right] \times exp\left[ - \int_0^R \alpha(R', \lambda_X) dR' \right] \tag{B.2}$$

We can then evaluate, for each lidar channel, the function

$$F_X(T) = \frac{\int_{\Delta\lambda_X} [d\sigma_X(\lambda', \pi, T)/d\Omega]\eta(\lambda')d\lambda'}{[d\sigma_X(\pi)/d\Omega]\eta(\lambda_X)} \tag{B.3}$$

which include the temperature dependence of the lidar equation and examine how it changes varying the temperature. The integral over the filter passband can be replaced with the summation over the Raman spectral lines which are transmitted. In the elastic lidar equation, the function $F_X(T)$ becomes important only in the case of very low aerosol load.

# Appendix C

# Channel cross talking

During our experiments we unfortunately found out that a non-negligible amount of light of the unwanted wavelength is recorded by the system. Firing the laser at only one wavelength, 355 nm or 532 nm, resulted in the recording of a lidar signal in those channels where the interference filters should have blocked the light (Figures C.1, C.2, and C.3). For example emitting only the beam at 355 nm we didn't expect a signal in the channel at 532 nm and 607 nm. The worst case is in the channel VIS-N2 at 607 nm where the intensity of the signal acquired shooting the laser at 355 nm (Figure C.3) is about one percent of the signal obtained shooting at 532 nm (Figure C.2). When all the laser outputs were sealed, no signals were observed at all.

In order to investigate more in details this phenomenon, we first removed the neutral density filters of the visible channels when blocking the laser green beam and the nd filters of the UV channels when blocking the laser UV beam (the Alluxa interference filters were left installed). Indeed, in doing so, the undesired signals were enhanced.
Then we observed how these signals change when adding additional interference filters, notch filters, and short pass filters. More in details the filters which were available are manufactured by Semrock and are:

- LL01-355
- LL01-531
- NF01-532
- NF03-532/1064
- SP01-532

These further observations suggested that there could be more than just one cause: the optical density of the interference filters may not be sufficient to block the elastically scattered laser light and a certain amount of unwanted light can reach the photocathode; there can be fluorescence effects; there are actually photons of the proper wavelength due to laser beam contamination (Figure C.7). This latter cause, although visible to the eye, was proved to be negligible in subsequent measurements. Therefore, as a first step, we decided to mount into the fiber launcher an additional interference filter. These additional filters have a FWHM of 10 nm and are manufactured by Thorlabs and are:

- FLH355-10
- FBH390-10
- FBH405-10
- FLH532-10
- FBH610-10

Observations with this new configuration show a slightly improvement of the picture: the undesired signals become negligible with the exception of the VIS-N2 channel where it affects the first 300 m (Figures C.4, C.5 and C.6).
These additional interference filters, which have a wider bandwidth compared to the Alluxa filters, do not alter significantly the performance of the fiber launcher.

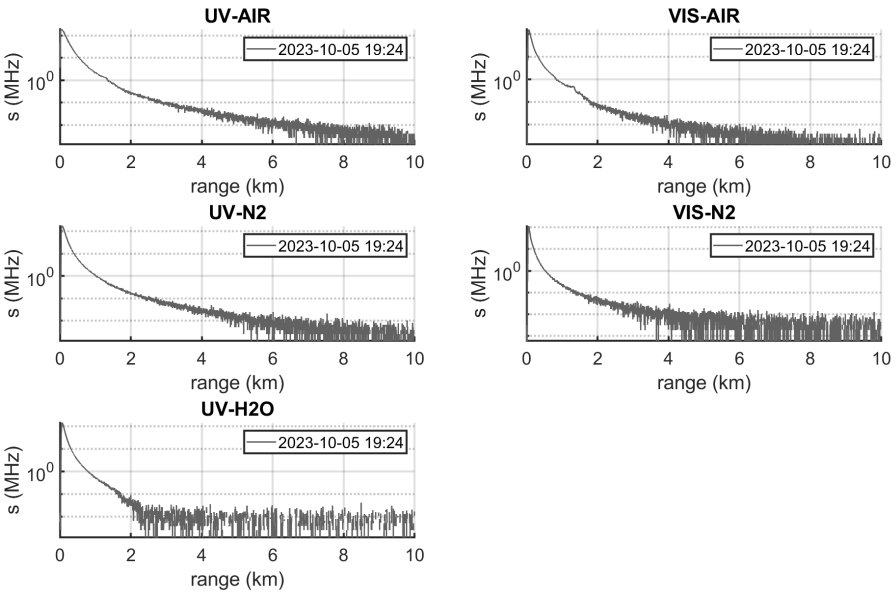


**Figure C.1:** Lidar signals with laser firing at 355 nm and 532 nm.

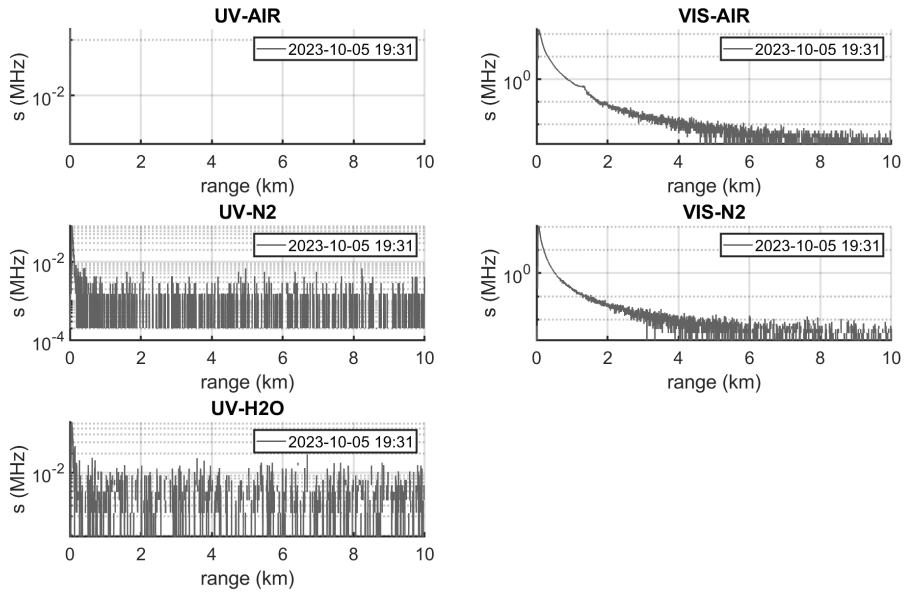


**Figure C.2:** Lidar signals with laser firing only at 532 nm.

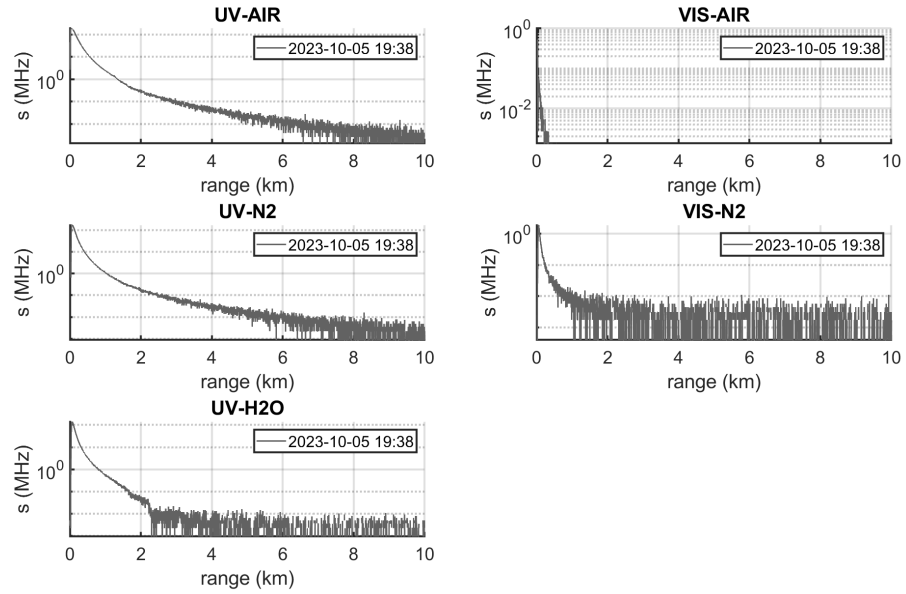


**Figure C.3:** Lidar signals with laser firing only at 355 nm.

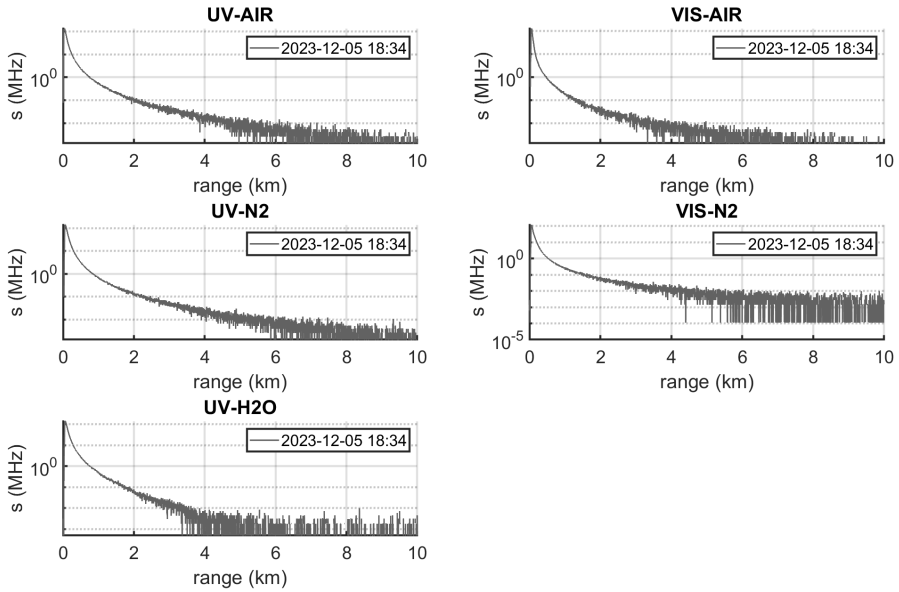


**Figure C.4:** Lidar signals with laser firing at 355 nm and 532 nm and the additional interference filters.

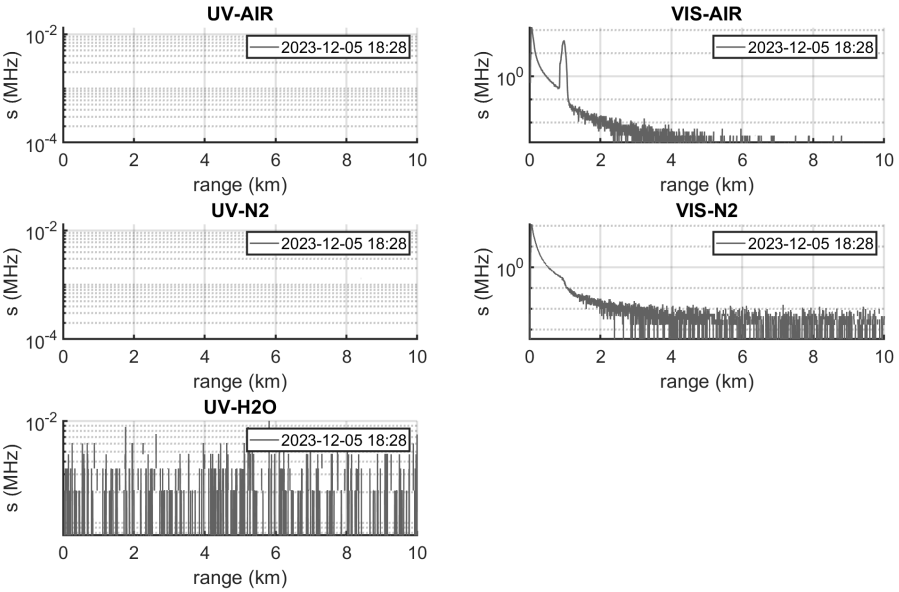


**Figure C.5:** Lidar signals with laser firing at 532 nm and the additional interference filters.

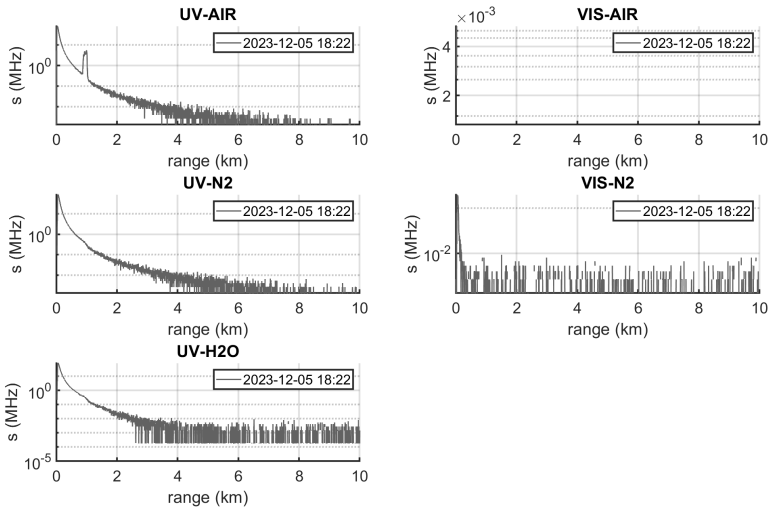


**Figure C.6:** Lidar signals with laser firing at 355 nm and the additional interference filters.

**Figure C.7:** Green contamination of the UV laser beam.

# Appendix D

# Auger Raman Lidar Technical Specifications

**Table D.1:** Technical data of the Auger Raman lidar

| | |
|---|---|
| **Laser** | |
| Type | Big Sky Laser Centurion Nd:YAG |
| Wavelength | 354.7 nm |
| Repetition Frequency | 100 Hz |
| Pulse duration | 7 ns |
| Divergence | 0.3 mrad |
| **Transmitter Optics** | |
| Flipper mirror | Newport 8892-K, CVI W2-PW1-1025-UV-248-355-0 (FM) |
| 1" Beam Splitter | CVI W2-PW1-1025-UV-248-355-0 (DBS) |
| Beam Expander | Thorlabs ELU-25-10X-351 (BEx10) |
| 2" Steering mirror | Newport 20QM20EN.35 (SMR) |
| **Receiver Optics** | |
| Geometry | Newtonian Reflector |
| Primary Mirror | 504 mm , $f/3$ |
| Coating | MgF2 and Al protection |
| **Optical Analyzer** | |
| Type | Beam Splitters + Interference filters |
| Liquid light guide | Newport 77629 (LLG) |
| Short wavelength pass filter | Newport 10-SWP-500 |
| Channels | air 355 nm, n2 386 nm, h2o 407 nm |
| Beam splitters | Barr BS-R345-361nm (BSair), Barr BS-R407-T320-395nm (BSn2) |
| Interference filters | Barr IF-CWL354.7-BW6nm (IFair), Barr IF-CWL3867-BW10A (IFn2), Barr IF-CWL4075-BW10A (IFh2o) |
| Notch filter | Barr LWP-T-378/415nm (NO) |

| | |
|---|---|
| Collimator lenses | Thorlabs LA1951 (L1),<br>Thorlabs LA1131 (L2),<br>Thorlabs LA1986 (L3) |
| **Data acquisition system** | |
| Detectors | PMT Electron Tubes 9829QB |
| Type | Photon Counting and Analog |
| Hardware | Embedded Devices APC-80250DSP |
| PC Max Count Rate | 250 MHz |
| A/D acquisition | up to 80 MHz |
| A/D bandwidth | 20 MHz |
| A/D resolution | 12 bit |

# Appendix E

# Lidar AQ Technical Specifications

**Table E.1:** Technical data of lidar AQ

| | |
|---|---|
| **Laser** | |
| Type | Innolas Spitlight Compact DPSS 100 |
| Wavelength | 355 nm, 532 nm, 1064 nm |
| Max Repetition Frequency | 100 Hz |
| Pulse duration | 8 ns |
| Divergence | $< 0.5$ mrad |
| **Transmitter Optics** | |
| 1" Beam Splitters | Thorlabs HBSY12, Thorlabs HBSY13 |
| 2" Beam Splitters | Thorlabs HBSY22, Thorlabs HBSY23 |
| Beam Expanders | Thorlabs BE05-355, Thorlabs BE05-532 |
| **Receiver Optics** | |
| Geometry | Newtonian Reflector |
| Primary Mirror | 200 mm , $f/3$ |
| Coating | MgF2 and Al protection |
| **Optical Analyzer** | |
| Type | Fiber Bundle + Interference filters |
| Channels | UV-AIR 355 nm, UV-N2 386 nm, UV-H2O 407 nm, VIS-AIR 532 nm, VIS-N2 607 nm |
| Alluxa IFs CWL(BW) | 354.7 nm(0.5 nm), 386.7 nm(0.5 nm), 407.6 nm(1.0 nm), 532.1 nm(0.5 nm), 607.6 nm(1.0 nm), |
| Thorlabs IFs CWL(BW) | FLH355-10 355 nm (10 nm), FBH390-10 390 nm(10 nm), FBH405-10 405 nm(10 nm), |

| | |
|---|---|
| | FLH532-10 532 nm(10 nm), |
| | FBH610-10 610 nm(10 nm), |
| ND filters | Thorlabs NUK01 |
| Collimator lenses | Thorlabs LA1951-A |
| Fiber Bundle | 925 optical fibers (CeramOptec) |
| | D. Core 200$\mu$m |
| | D. Cladding 220$\mu$m |
| | D. Buffer 245$\mu$m |
| | NA 0.22 |
| **Data acquisition system** | |
| Detectors | PMT Hamamatsu R9880U-113 |
| Type | Photon Counting |
| Hardware | Licel TR40 and PR40 |
| Max Count Rate | 800 MHz |

# Appendix F

# Lidar AQ Software - Manual

The program consists of six modules (classes). To use them, it is necessary to instantiate the main object lidarObj.m with, for example, **aq = lidarObj**. Then the commands of the individual modules must be preceded by aq. (for example, **aq.r.getTemp;**). However, the individual modules can still be instantiated with

```
r = rainObj;
w = weatherObj;
p = powerObj;
s = pmtObj;
d = daqObj;
l = laserObj;
```

However, before doing so, it is necessary to pay attention to their respective configuration files:

```
configurationRG9.xml
configurationWEATHER.xml
configurationPOWER.xml
configurationPMT.xml
configurationDAQ.xml
configurationLASER.xml
```

These files are automatically read when the objects are instantiated but can also be reloaded with the command **loadConf**.
Below, the various modules are seen in more detail.

## F.1 Modules

### F.1.1 lidarObj

This class includes methods that use functions and properties belonging to more than one submodule. In particular, it contains methods responsible for data acquisition and saving. The command **aq.OPEN** opens the dome and, unlike the command present in powerObj, checks the weather conditions during the opening (it takes 40 seconds). The command **aq.start** starts the data acquisition. First, it turns on the laser diodes and opens the shutter, then it starts the acquisition. Weather conditions and trigger are monitored during acquisition. In case of error or when

the acquisition is complete, the shutter is closed, and the diodes are turned off. The acquired data is saved with the command **aq.save** (preceded by **aq.d.download**). In the latest version, saving occurs automatically when the acquisition ends. To start an acquisition sequence, use the command **aq.seq(nacq)**, with nacq the number of acquisitions. With **aq.startnl**, a single acquisition without laser emission is initiated. There are also two methods to observe the effects of the discriminator and the HV of the photomultipliers: **aq.testDisc(nacq)**, **aq.testHV(hvmin, hvmax, dhv)**, where dhv is the HV step. Errors are checked with **aq.checkError**. This function returns **true** if at least one of the tracking errors variables of each individual modules is true. The command **aq.turnOFF** turns off the entire system.

### F.1.2 rainObj

This module manages the RG9 sensor for rain monitoring. First, it is necessary to establish a serial connection with **r.openRG9**. The function **r.getTemp** requests the temperature from the sensor and returns the numerical value. The function **r.getRain** checks if it is raining and returns the rain state: "1" indicates raining; "0" indicates not raining. If it is raining, the variable **r.err** is set to **true**. If the temperature is below zero, the sensor adds the word **COLD** to the response, indicating that reliability is not high in this case. Currently, there is no check on **COLD**. The sensitivity of the sensor can be set with the command **r.setSensitivity**.

### F.1.3 weatherObj

This module reads meteorological data from the CETEMPS weather station (web site). The function **w.read** reads the most recent weather data and compares the log date with the system date. In the private variable **w** of type struct, the date, temperature, wind speed, rainfall rate (the rain gauge sensitivity is not sufficient for our purposes), relative humidity, and atmospheric pressure are saved. The variable w can be requested with the command **w.getW**.

### F.1.4 powerObj

The powerObj module manages the Denkovi relay box. To operate, it requires Java and the Denkovi Relay Command Line Tool. With the commands **p.pmtON**, **p.pmtOFF**, and **p.pmtSTATUS**, it is possible to turn on, turn off, and check the status of the Ethernet Controller of the photomultipliers. The same applies to the Ethernet Controller of the transient recorder, the laser, the chiller, and the trigger. In the command, replace pmt respectively with daq, laser, chiller, and trigger.
The commands **p.OPEN** and **p.CLOSE** open and close the dome. The command is sent to the respective relay, waits for 40 seconds, and then the command is resent to rearm the dome. The dome's status is updated in the variable p.dome (public).
Finally, the command **p.getState** checks the status of the two Ethernet Controllers, the laser, the chiller, and the trigger, and updates the status in the variable state (private). This variable is then provided as output by the command.

### F.1.5 pmtObj

This module manages the Ethernet Controller of the detector power supplies.
The command **s.openPMT** opens the connection with the Ethernet Controller.
The command **s.getDET** outputs the status of all detectors. This is checked with the **s.checkAll** command.
The **s.init** command sets the detector power supplies as indicated in the configuration file.
To request the status of individual detectors, you can use the commands **s.getHV(#pmt)** and **s.getAPD(#apd)**, where #pmt and #apd identify the detector of interest.
Finally, to set individual detectors, use the commands **s.setHV(#pmt, hv)** for photomultipliers and **setApdHV(#apd, hv)** and **setApdTemp(#apd, 'ON—OFF')** for photodiodes. Here hv is the desired high voltage.

### F.1.6 daqObj

This module manages the Ethernet Controller of the Transient Recorder.
The command **d.openDAQ** opens the connection with the Ethernet Controller. You can interrupt the connection with the command **d.closeDAQ**. This allows connecting to the Ethernet Controller with another software such as TCPIP Acquis.
The command **d.init** initializes the transient recorder according to the configuration file. If you want to modify the configuration of the transient recorder, you can do so by editing the parameters in the variable **d.conf** and relaunching the **d.init** command. Alternatively, you can select the TRx with the **d.sel("x")** command and modify the settings with the commands (see Licel manual [118]):

- **d.setDiscriminator**
- **d.setThreshold**
- **d.setMaxBins**
- **d.setMaxShots**
- **d.limit**
- **d.setPreTrig**
- **d.setRange**
- **d.setFreqDiv**

It's possible to set the variables **d.nbin** (number of bins to download) and **d.nshots** (number of profiles to acquire) either by directly modifying them or using the methods **d.setNbin(nb)** and **d.setNshots(ns)**.
In case of changes to the configuration file, it needs to be reloaded with the command **d.loadConf** (followed by **d.init**). The methods for signal acquisition and profile saving are found in the lidarObj.m class. These methods invoke functions present in daqObj.m

### F.1.7 laserObj

To use the laser, you first need to turn it on with the command **p.laserON** and then to start Spitlight GUI with the command **l.openSpitlight** (Spitlight is set to automatically connect to the laser). Then, you need to establish a connection with Spitlight using the command **l.openLaser**. A callback is configured on the TCP connection. Whenever a byte is available, the function bigBrother is invoked to read the messages sent by Spitlight. When the laser diodes are turned on, the laser continuously sends the shot number, effectively blocking Matlab. For this reason, if the response **SHOT_COUNTER** is recognized, the while loop is temporarily exited with a break statement.

## F.2 GUI

One way to start the app is by using the command **app = lidarAQ;** in the MATLAB Command Window.
Upon starting the app, weather conditions are checked, and the Cetemps Weather Station panel is updated. The status of the relays is also checked.
Clicking on "start loop" initiates an infinite loop where weather conditions, relay status, and laser status are checked every minute. If entering this loop before establishing a connection with the SpitlightGUI laser program, the laser module will encounter an error as it won't receive any response. You can reset the error by typing **app.aq.l.err = false**. It is recommended to start the loop only after initializing the laser.
While inside the main loop, it is not possible to use other MATLAB functions. Clicking the "Stop Loop" button, the while loop is interrupted, and the Command Window becomes available again. You can then access the app's workspace (all attributes and methods defined as public within the classes) with **app.**, and use advanced commands not implemented in the GUI.

### F.2.1 Data Acquisition

First, you need to turn on the trigger (currently powered directly from the PC, so no need to click on TRIG), the laser, and the two Ethernet controllers (HV and DAQ). Wait a few seconds for the network switch to assign IP addresses to all components. From the Laser panel, open Spitlight GUI, which will automatically connect to the laser. Click on "connect" to establish a connection between our software and Spitlight GUI. Click on "start" and turn on the chiller from the Power panel. The laser will start warming up and should reach 25°C.
In the PMT panel, click on "Connect". The photomultiplier power supply voltages will update, and you'll be able to modify them.
In the DAQ panel, click on "Connect". Then, click on "Initialize" to initialize the acquisition boards according to the configuration file configurationDAQ.xml. If the configuration file is modified, you can reload it with "Load Conf." and clicking on "Initialize" again. Also, if the values of # bins and # shots are modified, you need to click on "Initialize" again.
Once the laser is at the right temperature, you can open the dome with "OPEN" in the Dome panel and start the acquisition with "Start" in the DAQ panel. After the

acquisition is complete, the profile will be saved in the data folder within the main program folder.

## F.3 Data file

The acquired profiles are saved in the file named YYYY-MM-DD-hh-mm-ss.m. Inside the file, a struct variable named lidardata is organized as follows:

```
lidardata:

    Station:
        Location
        Latitude
        Longitude
        Altitude
        StartTime
        StopTime

    Channel(i):
        Profile
        Type
        Mem
        Info
        Wavelength
        Polarization
        InputRange
        FreqDiv
        BinWidth
        Pretrigger
        Shots

    Weather:
        date
        temp
        wind
        rain
        humidity
        bar

    Detector:
        pmt
        apd
        tec
        Def
```

# Bibliography


[1] John M. Wallace and Peter V. Hobbs. *Atmospheric Science: An introductory Survey (Second Edition)*. Academic Press, 2006.

[2] William C. Hinds. *Aerosol Technology, Properties, Behaviour, and Measurement of Airborne Particles. Second Edition*. John Wiley & Sons Inc., New York, 1999.

[3] O. Boucher. *Atmospheric aerosols: properties and climate impacts*. Springer, 2015.

[4] S. Ramachandran. *Atmospheric aerosols: characteristics and radiative effects*. CRC Press, Taylor & Francis Group, 2018.

[5] V. Masson-Delmotte et al. "IPCC, 2021: Summary for Policymakers." In: *Climate Change 2021: The Physical Science Basis. Contribution of Working Group I to the Sixth Assessment Report of the Intergovernmental Panel on Climate Change* (2021), pp. 3–32.

[6] K. N. Grainger. *Some useful formulae for particle size distributions and optical properties*. `https://eodg.atm.ox.ac.uk/user/grainger/research/aerosols.pdf`.

[7] C. E. Junge. "Atmospheric chemistry". In: *Adv. Geophys.* 4 (1958), pp. 1–108.

[8] G. W. Petty and W. Huang. "The Modified Gamma Size Distribution Applied to Inhomogeneous and Nonspherical Particles: Key Relationships and Conversions". In: *JAS* 68.7 (2011), pp. 1460–1473.

[9] K. N. Liou. *An introduction to atmospheric radiation, Second Edition*. Academic Press, 2002.

[10] C. F. Bohren and D. R. Huffman. *Absorption and scattering of light by small particles*. John Wiley & Sons, 1983.

[11] J. Lenoble, L. Remer, and D. Tanré. *Aerosol remote sensing*. Springer, 2013.

[12] R. Measures. *Laser Remote Sensing*. Krieger Publishing Company, 1992.

[13] J.W. Strutt. "On the light from the sky, its polarization and colour". In: *Phil. Mag.* 41 (1871), pp. 107–120, 274–279.

[14] G. Mie. "Beiträge zur Optik trüber Medien, speziell kolloidaler Mettallösunger". In: *Ann. Phisik* 25 (1908), pp. 377–445.

[15] P. Carlson and A. De Angelis. "Nationalism and internationalism in science: the case of the discovery of cosmic rays". In: *EPJ H* 35 (2011).

[16] B. Rossi. "Misure della distribuzione angolare di intensità della radiazione penetrante all'Asmara". In: *Ric. Sci. Suppl.* 1 (1934), pp. 579–589.

[17] P. Auger et al. "Extensive Cosmic-Ray Showers". In: *Rev. Mod. Phys.* 11 (1939), pp. 288–291.

[18] A. M. Hillas. "The Origin of Ultra-High-Energy Cosmic Rays". In: *Ann. Rev. Astron. Astrophys.* 22 (1984), pp. 425–444.

[19] A. Di Matteo. *Ultra-high-energy cosmic ray phenomenology: Monte Carlo simulations and experimental data*. PhD Thesis, Università degli studi dell'Aquila, 2015.

[20] F. G. Schroder. "News from Cosmic Ray Air Shower". In: *Proceedings of Science (ICRC2019)* 030 (2019).

[21] V. Berezinsky, A. Z. Gazizov, and S. I. Grigorieva. "On astrophysical solution to ultrahigh-energy cosmic rays". In: *Phys. Rev. D* 74 (2006), p. 043005. DOI: 10.1103/PhysRevD.74.043005. arXiv: hep-ph/0204357.

[22] T. K. Gaisser and T. Stanev. "High-energy cosmic rays". In: *Nucl. Phys. A* 777 (2005), pp. 98–110.

[23] T. K. Gaisser. *Cosmic Rays and Particle Physics*. Cambridge University Press, 1990.

[24] T. K. Gaisser and A. M. Hillas. "Reliability of the method of constant intensity cuts for reconstructing the average development of vertical showers". In: *Proc. 15th ICRC* 8 (1977), pp. 353–357.

[25] P. Trávníček. *Detection of high-energy muons in cosmic ray showers*. PhD Thesis, Charles University, Prague, 2004.

[26] W. Heitler. *The Quantum Theory of Radiation*. Third edition, Oxford University Press, London, 1954.

[27] J. Matthews. "A Heitler model of extensive air showers". In: *Astropart. Phys.* 22.5 (2005), pp. 387–397. DOI: https://doi.org/10.1016/j.astropartphys.2004.09.003.

[28] The Pierre Auger Collaboration. "Muons in air showers at the Pierre Auger Observatory: Measurement of atmospheric production depth". In: *Phys. Rev. D* 90 (2014).

[29] F. Arqueros, J. R. Hörandel, and B. Keilhauer. "Air fluorescence relevant for cosmic-ray detection—Summary of the 5th fluorescence workshop, El Escorial 2007". In: *Nucl. Instrum. Methods Phys. Res., Sect. A* 597 (2008), pp. 1–22.

[30] The Pierre Auger Collaboration. "A study of the effect of molecular and aerosol conditions in the atmosphere on air fluorescence measurements at the Pierre Auger Observatory". In: *Astroparticle Physics* 33.2 (2010), pp. 108–129.

[31] F. Salamida. "Highlights from the Pierre Auger Observatory". In: *PoS* ICRC2023 (2023), p. 016. DOI: 10.22323/1.444.0016.

[32] V. Novotny. "Energy spectrum of cosmic rays measured using the Pierre Auger Observatory". In: *PoS* ICRC2021 (2021), p. 324. DOI: 10.22323/1.395.0324.

[33] O. Tkachenko. "Studies of the mass composition of cosmic rays and proton-proton interaction cross-sections at ultra-high energies with the Pierre Auger Observatory". In: *PoS* ICRC2023 (2023), p. 438. DOI: 10.22323/1.444.0438.

[34] R. M. de Almeida. "Large-scale and multipolar anisotropies of cosmic rays detected at the Pierre Auger Observatory with energies above 4 EeV". In: *PoS* ICRC2021 (2021), p. 335. DOI: 10.22323/1.395.0335.

[35] The Pierre Auger Collaboration. "The Pierre Auger Cosmic Ray Observatory". In: *Nucl. Instrum. Methods Phys. Res., Sect. A* 798 (2015), pp. 172–213.

[36] M. Malacari. *Systematic Effects in the Measurement of Vertical Aerosol Profiles at the Pierre Auger Observatory*. PhD Thesis, The University of Adelaide, 2016.

[37] R. Mussa and G. Ciaccio. "Observations of ELVES at the Pierre Auger Observatory". In: *Eur. Phys. J. Plus* 127 (2012).

[38] E. Varela for the Pierre Auger Collaboration. "The low-energy extensions of the Pierre Auger Observatory". In: *J. Phys.: Conf. Ser.* 468 (2013), p. 012013. DOI: 10.1088/1742-6596/468/1/012013.

[39] G. Silli. "Performance of the 433 m surface array of the Pierre Auger Observatory". In: *PoS* ICRC2021 (2021), p. 224. DOI: 10.22323/1.395.0224.

[40] I. Allekotte et al. "The surface detector system of the Pierre Auger Observatory". In: *Nucl. Instrum. Methods Phys. Res., Sect. A* 586 (2008), pp. 409–420.

[41] The Pierre Auger Collaboration. "The fluorescence detector of the Pierre Auger Observatory". In: *Nucl. Instrum. Methods Phys. Res., Sect. A* 620 (2010), pp. 227–251.

[42] A. Castellina. "AugerPrime: the Pierre Auger Observatory Upgrade". In: *EPJ Web Conf.* 210 (2019).

[43] B. Keilhauer. "Atmospheric Monitoring for Astroparticle Physics Observatories". In: *PoS ICRC 2023* 023 (2023).

[44] The Pierre Auger Collaboration. "Atmospheric effects on extensive air showers observed with the surface detector of the Pierre Auger observatory". In: *Astroparticle Physics* 32 (2009), pp. 89–99.

[45] L. Valore. "Atmospheric aerosol attenuation effect on FD data analysis at the Pierre Auger Observatory". In: *EPJ Web Conf.* 210 (2019).

[46] The Pierre Auger Collaboration. "Description of atmospheric conditions at the Pierre Auger Observatory using the Global Data Assimilation System (GDAS)". In: *APh* 35 (2012), pp. 591–607.

[47] The Pierre Auger Collaboration. "Techniques for measuring aerosol attenuation using the Central Laser Facility at the Pierre Auger Observatory". In: *J. Instrum.* (2013).

[48] B. Fick et al. "The Central Laser Facility at the Pierre Auger Observatory". In: *JINST* 1 (2006).

[49] S. Y. BenZvi et al. “Measurement of the aerosol phase function at The Pierre Auger Observatory”. In: *Astropart. Phys.* 28 (2007), pp. 312–320.

[50] L. Henyey and J. Greenstein. “Diffuse radiation in the Galaxy”. In: *Astrophysical Journal* 93 (1941), pp. 70–83.

[51] The Pierre Auger Collaboration et al. “The FRAM robotic telescope for atmospheric monitoring at the Pierre Auger Observatory”. In: *JINST* 16 (2021), pp. 70–83.

[52] D. Müller et al. “Aerosol-type-dependent lidar ratios observed with Raman lidar”. In: *J. Geophys. Res.* 112 (2007).

[53] D. Müller, U. Wandinger, and A. Ansmann. “Microphysical particle parameters from extinction and backscatter lidar data by inversion with regularization: theory”. In: *Appl. Opt.* 38.12 (1999), pp. 2346–2357.

[54] P. Di Girolamo et al. “Aerosol observations by lidar in the nocturnal boundary layer”. In: *Appl. Opt.* 38.21 (1999), pp. 4585–4595.

[55] U. Wandinger. “Introduction to Lidar”. In: *Lidar, Range-Resolved Optical Remote Sensing of the Atmosphere* (2005). Ed. by Springer.

[56] V. A. Kovalev and W. E. Eichinger. *Elastic Lidar. Theory, Practice, and Analysis Methods*. John Wiley & Sons, Inc., 2004.

[57] E.H. Synge. “XCI. A method of investigating the higher atmosphere”. In: *London Phil. Mag.* 9 (1930), pp. 1014–1020.

[58] M.A. Tuve, E. A. Johnson, and O.R. Wulf. “A new experimental method for study of the upper atmosphere”. In: *Terr. Mag. and Atmos. Elec.* 40 (1935), pp. 452–454.

[59] E. O. Hulburt. “Observations of a Searchlight Beam to an Altitude of 28 Kilometers”. In: *J. Optical Soc. Amer.* 27 (1937), pp. 377–382.

[60] E. A. Johnson et al. “The Measurement of Light Scattering by the Upper Atmosphere from a Search-Light Beam”. In: *J. Optical Soc. Amer.* 29 (1938), pp. 512–517.

[61] L. Elterman. “A series of stratospheric temperature profiles obtained with the searchlight technique”. In: *J. Geophys. Res.* 58 (1953), pp. 519–530.

[62] E. L. Pruitt. “The Office of Naval Research and Geography”. In: (1979).

[63] T. H. Maiman. “Stimulated Optical Radiation in Ruby”. In: *Nature* 187 (1960), pp. 493–494.

[64] F. J. McClung and R. W. Hellwarth. “Giant Optical Pulsations from Ruby”. In: *Appl. Opt.* 33 (1962), pp. 828–829.

[65] L. D. Smullin and G. Fiocco. “Optical Echoes from the Moon”. In: *Nature* 194 (1962), p. 1267.

[66] G. Fiocco and L. D. Smullin. “Detection of Scattering Layer in the Upper Atmosphere (60-140 km) by Optical Radar”. In: *Nature* 199 (1963), p. 1275.

[67] G. Fiocco and G. Grams. “Observations of the Aerosol Layer at 20 km by Optical Radar”. In: *J. Atmos. Sci.* 21 (1964), pp. 323–324.

[68] D. D. Turner, J. E. M. Goldsmith, and R. A. Ferrare. "Development and Applications of the ARM Raman Lidar". In: *The Atmospheric Radiation Measurement (ARM) Program: The First 20 Years, Meteor. Monogr.* 57 (2016).

[69] D. A. Leonard. "Observation of Raman Scattering from the Atmosphere using a Pulsed Nitrogen Ultraviolet Laser". In: *Nature* 216 (1967), pp. 142–143.

[70] J. A. Cooney. "Measurements on the Raman component of laser atmospheric backscatter". In: *Appl. Phys. Lett.* 12.2 (1968), pp. 40–42.

[71] J. A. Cooney. "Measurements Separating the Gaseous and Aerosol Components of Laser Atmospheric Backscatter". In: *Nature* 224 (1969), pp. 1098–1099.

[72] S. H. Melfi, J. D. Lawrence, and M. P. McCormick. "Observations of Raman scattering by water vapor in the atmosphere". In: *Appl. Phys. Lett.* 15.9 (1969), pp. 295–297.

[73] A. Ansmann, M. Riebesell, and C. Weitkamp. "Measurement of atmospheric aerosol extinction profiles with a Raman lidar". In: *Opt. Lett.* 15.13 (1990), pp. 746–748.

[74] A. Ansmann et al. "Independent measurement of extinction and backscatter profiles in cirrus clouds by using a combined raman elastic-backscatter lidar". In: *Appl. Opt.* 31.33 (1992), pp. 7113–7131.

[75] W. L. Eberhard. "Correct equations and common approximations for calculating Rayleigh scatter in pure gases and mixtures and evaluation of differences". In: *Appl. Opt.* 49.7 (2010), pp. 1116–1130.

[76] A. Bucholtz. "Rayleigh-scattering calculations for the terrestrial atmosphere". In: *Appl. Opt.* 34.15 (2005), pp. 2765–2773.

[77] M. Adam. "Notes on Rayleigh scattering in lidar signals". In: *Appl. Opt.* 51.12 (2012), pp. 2135–2149.

[78] D. N. Whiteman, S.H. Melfi, and R.A. Ferrare. "Raman lidar system for the measurement of water vapor and aerosols in the Earth's atmosphere". In: *Appl. Opt.* 31 (1992), pp. 3068–3082.

[79] U. Wandinger. "Raman Lidar". In: *Lidar, Range-Resolved Optical Remote Sensing of the Atmosphere* (2005). Ed. by Springer.

[80] A. Foth et al. "Water vapour profiles from Raman lidar automatically calibrated by microwave radiometer data during Hope". In: *Atmos. Chem. Phys.* 15 (2015), pp. 7753–7763.

[81] T. Leblanc, I. S. McDermid, and T. D. Walsh. "Ground-based water vapor raman lidar measurements up to the upper troposphere and lower stratosphere for long-term monitoring". In: *Atmos. Meas. Tech.* 5 (2012), pp. 17–36.

[82] T. Leblanc and I. S. McDermid. "Accuracy of Raman lidar water wapor calibration and its applicability to long-term measurements". In: *Appl. Opt.* 47.30 (2008), pp. 5592–5603.

[83] G. Dai et al. "Calibration of Raman lidar water vapor profiles by means of AERONET photometer observations and GDAS meteorological data". In: *Atmos. Meas. Tech* 11 (2018), pp. 2735–2748.

[84] M. Iarlori et al. “Effective resolution concepts for lidar observations”. In: *Atmos. Meas. Tech* 8 (2015), pp. 5157–5176.

[85] Glenn F. Knoll. *Radiation Detection and Measurement*. Wiley.

[86] G. D’Amico et al. “Earlinet single calculus chain - technical - part 1: Preprocessing of raw lidar data”. In: *Atmos. Meas. Tech* 9 (2016), pp. 491–507.

[87] L. R. Bissonette. “Lidar and Multiple Scattering”. In: *Lidar, Range-Resolved Optical Remote Sensing of the Atmosphere* (2005). Ed. by Springer.

[88] H. Baars et al. “An overview of the first decade Polly$^{NET}$: an emerging network of automated Raman-polarization lidars for continuous aerosol profiling”. In: *Atmos. Chem. Phys.* 16 (2016), pp. 5111–5137.

[89] A. Amodeo. “Statistical error evaluation in aerosol optical properties retrieval”. In: *Fiffth EARLINET-ASOS workshop* (2008).

[90] I. Mattis et al. “Earlinet single calculus chain - technical - part 2: Calculation of optical products”. In: *Atmos. Meas. Tech* 9 (2016), pp. 3009–3029.

[91] V. M. Harvey. “Real-time Measurements with Atmospheric Instruments at the Pierre Auger Observatory”. In: *PoS ICRC 2019* 283 (2019).

[92] L. Wiencke et al. “Joint elastic side-scattering LIDAR and Raman LIDAR measurements of aerosol optical properties in south east Colorado”. In: *JINST* 12 (2017).

[93] V. Rizi. “The Auger Raman Lidar: 2013-2022 continuous observations”. In: *AtmoHEAD 2022 workshop* (2022).

[94] V. Rizi et al. “Atmospheric monitoring with LIDARs at the Pierre Auger Observatory”. In: *Eur. Phys. J. Plus* 127 (2012).

[95] V. M. Harvey. “A new cross-check and review of aerosol attenuation measurements at the Pierre Auger Observatory”. In: *PoS ICRC 2023* 300 (2023).

[96] U. Wandinger and A. Ansmann. “Experimental determination of the lidar overlap profile with Raman lidar”. In: *Appl. Opt.* 41.3 (2002), pp. 511–514.

[97] N. Rogelj et al. “Experimental determination of UV- and VIS- lidar overlap function”. In: *Opt. Pura Apl.* 47.3 (2014), pp. 169–175.

[98] *Angle of incidence AOI and polarization - Alluxa*. URL: `https://alluxa.com/optical-filter-specs/angle-of-incidence-aoi-and-polarization/`.

[99] F. J. Bailén et al. “On Fabry-Pérot Etalon-based Instruments. I. The Isotropic Case”. In: *ApJS* 241 (2019).

[100] *Zemax*. URL: `https://www.zemax.com/`.

[101] G. Avila et al. “Ro-vibrational Raman Cross Sections of Water Vapor in the OH Stretching Region”. In: *J. Mol. Spectrosc.* 196 (1999), pp. 77–92.

[102] *Denkovi Assembly Electronics LTD*. URL: `http://denkovi.com/`.

[103] *Licel GmbH*. URL: `https://www.licel.com/`.

[104] *Arduino web site*. URL: `www.arduino.cc`.

[105] *Rain gauge RG-9*. URL: `https://rainsensors.com/products/rg-9/`.

[106] *Cetemps weather station*. URL: `http://meteorema.aquila.infn.it/tempaq/main.html`.

[107] *MATLAB web site*. URL: `https://www.mathworks.com/products/matlab.html`.

[108] G. Pappalardo et al. "EARLINET: towards an advanced sustainable European aerosol lidar network". In: *Atmos. Meas. Tech.* 7 (2014), pp. 2389–2409.

[109] V. Freudenthaler et al. "EARLINET lidar quality assurance tools". In: *Atmos. Meas. Tech.* (2018).

[110] K. Stelmaszczyk, M. Dell'Aglio, and S. Chudzynski. "Analytical function for lidar geometrical compression form-factor calculations". In: *Appl. Opt.* 44 (2005), pp. 1323–1331.

[111] A. Savitzky and M. J. E. Golay. "Smoothing and differentiation of data by simplified least squares procedures". In: *Anal. Chem.* 36.8 (1964), pp. 1627–1639.

[112] A. Ansmann and D Müller. "Lidar and Atmospheric Aerosol Particles". In: *Lidar, Range-Resolved Optical Remote Sensing of the Atmosphere* (2005). Ed. by Springer.

[113] J. D. Klett. "Stable analytical inversion solution for processing lidar returns". In: *Appl. Opt.* 20.2 (1981), pp. 211–220.

[114] J. D. Klett. "Lidar inversion with variable backscatter/extinction ratios". In: *Appl. Opt.* 24.11 (1985), pp. 1638–1643.

[115] F. G. Fernald. "Analysis of atmospheric lidar observations: some comments". In: *Appl. Opt.* 23.5 (1984), pp. 652–653.

[116] Y. Sasano et al. "Error caused by using a constant extinction/backscattering ratio in the lidar solution". In: *Appl. Opt.* 24.22 (1985), pp. 3929–3932.

[117] D. N. Whiteman. "Examination of the traditional Raman lidar technique. I. Evaluating the temperature-dependent lidar equations". In: *Appl. Opt.* 42 (2003), pp. 2571–2592.

[118] Licel GmbH. *Licel Ethernet Controller – Installation and Reference Manual*. `https://licel.com/manuals/ethernet_pmt_tr.pdf`.